NORTHWESTERN UNIVERSITY

Understanding Stabilization of Noncentrosymmetric Inorganic Phases by Analysis of

Static Structures and Dynamic Processes

A DISSERTATION

SUBMITTED TO THE GRADUATE SCHOOL
IN PARTIAL FULFILLMENT OF THE REQUIREMENTS

for the degree

DOCTOR OF PHILOSOPHY

Field of Chemistry

By

Michael John Edward Holland

EVANSTON, ILLINOIS

December 2016

Abstract

Understanding Stabilization of Noncentrosymmetric Inorganic Phases by Analysis of

Static Structures and Dynamic Processes

Michael John Edward Holland

The properties of crystalline materials are controlled by their composition and by their structure, however, the structure of a crystal is only partly controlled by its composition. Development of specifically directed inorganic syntheses will require an understanding of the dynamics of crystal phase forming processes, especially those processes involved in generating specific symmetry features. One successful strategy, intended to exert synthetic control over the symmetry of crystal structures involves incorporating polar, anionic species, called basic building units (BBUs). Polar BBUs tend to adopt ordered configurations, increasing the probability that discovered structures will have polar symmetry. Discovery of eight new compounds with general formula $K_{10}(M_2O_nF_{11-n})X$ (M = V^V, Nb^V, n = 2, M = Mo^{VI}, n = 4; X^- = $(F_2Cl)_{1/3}$, Cl, $([Br][Br_3])_{1/2}$, and $([I][I_3])_{1/2}$) is reported. Post-synthetic structure analysis these compounds which crystallize in the space groups $P3m1$, $Pmn2_1$, and $C2/m$, is used to analyze and expand on the Λ-shaped anionic unit strategy.

The atom scale processes involved in the phase transition are examined through computational Molecular Dynamics (MD) simulations. Atomistic MD simulations present the technical challenge of developing models for calculating interatomic interactions that can reliably reproduce experimental results. A strategy for improving the accuracy of empirical interatomic interaction models is outlined. Cryogenic temperature (~15K) and variable-pressure

(1-10 GPa) diamond anvil cell single crystal diffraction experiments on the *Pna*2$_1$ phase of KNaNbOF$_5$ are used to develop a set of empirical pairwise interatomic interaction functions of the complex five element system. The atom scale dynamics of a temperature driven reconstructive phase transition in KNaNbOF$_5$ are examined, leading to the discovery of a dynamically disordered high temperature crystal structure, and the origin of the NCS phase stabilization upon cooling. The reconstructive transition going from the *P*4/*nmm* phase to the high temperature *Cmcm* phase is believed to result from a loss of O/F site ordering caused by rigid rotations of octahedral [NbOF$_5$]$^{2-}$ BBUs. The high temperature phase is found to be a dynamically disordered state involving two locally stable phases in the potential energy landscape with *Pbcm* and *Pnma* space group symmetries.

Acknowledgements

I am grateful to all the people who helped me in the course of this research, throughout my graduate career, and throughout my life. I cannot do justice to all of the people who have contributed to making me the person I have become, and what follows is only a brief selection.

My advisor, Kenneth R. Poeppelmeier gave me an excellent working environment. His advice and scientific experience helped me to shape my research, and at the same time he gave me the freedom to develop my own scientific ideas. I could not have asked for a better advisor.

I want to thank my wife, Ruby, who continuously inspires me to be a better person, both at work, and in life.

I would like to thank my mother, Jean Holland, who always encouraged me and my brothers to be curious and to find answers. I am thankful to my brothers Peter, Philip, Stephen, and Thomas, for more than I can put into words. I am also very grateful to my father, Frederick Holland, who did not live to see this day.

Nenian Charles has been a fantastic collaborator, and helped me shape large portions of my research. Over the course of our many discussions I gained a much better understanding of the theoretical perspective of solid-state chemistry.

The other members of the oxide-fluoride subgroup of the lab of Ken Poeppelmeier were instrumental in shaping my graduate research. In particular, Dr Martin Donakowski taught me the skills and attitudes necessary for the solid-state field, and is one of the best scientists I have had the pleasure of working with. Dr Romain Gautier provided a great deal of experienced

advice and insight in the early part of my graduate studies. Dr Kelvin Chang, Dr Hongcheng Lu, Stacy Vinokur, Jackie Cantwell, and Dr Shichao Wang all contributed to the cordial and supportive environment that enabled this work. Members of other subgroups of the lab also frequently contributed insights, new perspectives, and assistance in the course of my research. Alisson Wustrow, Dr Jared Incorvati, Dr Robert Kennedy, Dr Karl Rickert, Dr Daniel Fowler, Dr Linhua Hu, James Mcarthy, Dr Yuyuan Lin, Dr Justin Hancock, Steven Flynn, and Ryan Paull, have all been wonderful colleagues and friends.

Contents

List of Figures

Chapter 4

Chapter 5

Chapter 8

List of Tables

Chapter 1 Introduction

1.1 Structures and Properties of Crystals

The properties of crystal materials are controlled by their composition and by their structure. The structure of a crystal is only partly controlled by its composition. Phase transitions happen when compounds experience changing temperature and pressure conditions. Variations to the crystallization conditions can also influence structure. It is possible to obtain multiple different structures with the same composition but different properties. By improving our understanding of the relationships between composition, formation conditions, and crystal structure, we will eventually be able to selectively synthesize new crystal materials in a process of targeted discovery.

One important aspect of crystal structure is symmetry, and many properties are only observed in crystals with, or lacking, specific kinds of symmetry. The absence of inversion symmetry is a condition required for a material to exhibit properties including piezoelectricity, ferroelectricity, second harmonic generation (SHG), optical activity, and several other phenomena. The ability to target specific symmetry qualities is crucial for directed inorganic crystals synthesis on the basis of desired properties.

1.2 Design Strategies

In the past few decades strategies that enable a measure of synthetic control over the symmetry of newly discovered solid-state materials have been developed. The most extensively applied strategy involves the inclusion in synthetic investigations of polar, anionic, transition metal coordination complexes, referred to as basic building units (BBUs). Polar BBUs tend to

pack in ordered configurations, increasing the probability that a newly discovered phase will have polar symmetry. In a large number of these investigations the anionic BBUs involved have been octahedral coordination complexes of early transition metals. Anionic BBUs with a combination of oxide and fluoride ligands are often polar and their use increases the rate of discovery of polar NCS compounds. Recent extensions to this strategy suggest that the incorporation of larger anionic units with bent shapes can further improve the chances of discovering new polar phases.

Applying these strategies in the course of my research resulted in the discovery of several new compounds of formulae $K_{10}(M_2O_nF_{11-n})X$ ($M = V^V$, Nb^V, $n = 2$, $M = Mo^{VI}$, $n = 4$; $X =$ halide). Part of this thesis details the post synthetic analysis of this group of materials, and identifies specific local interactions that control the symmetry of the individual compounds.

Directed inorganic crystal syntheses will ultimately require a thorough understanding of the dynamics of crystallization processes, especially those processes that result in the adoption or breaking of symmetry features. Atomistic behavior can be studied through computational simulations using molecular dynamics techniques. Such simulations present a technical challenge, both in execution and in the development of accurate computational models composed of interatomic potential functions. Some of the challenges to development of accurate models are discussed, and some strategies are presented.

Part of this thesis discusses possible nonlinear relationships between temperature and experimental bond-lengths in crystal structures reported in the literature. These relationships are not associated with changes in symmetry or phase, and a comparison is drawn to a previously

documented nonlinear relationship between pressure and experimental bond-length. A physical

origin of this a relationship is proposed and the consequences and the possible benefits of the

effect are discussed.

The last part of this thesis describes an investigation of solid-solid phase transitions on

the basis of the atomic scale dynamics involved. A sequence of temperature-induced phase

transitions in the compound $KNaNbOF_5$ provide an opportunity to investigate the dynamics of a

crystal system as it changes from a structure with inversion symmetry, to a high temperature

transition structure, and then to a structure without inversion symmetry. The previously

unidentified structure of the high temperature phase of $KNaNbOF_5$ is determined using a

molecular dynamics simulation and matched to experimental data, and both the transition

kinetics and the effect that stabilizes the polar phase are identified and explained.

1.3 Noncentrosymmetry

The symmetry of a system is defined as the set of operations under which the system is

invariant. In other words if you can do something to a system and afterwards it looks the same as

it did before, the system is said to be symmetrical with respect to whatever it was you did to it.

The formal mathematical description of all the symmetry classifications of 3-dimensional crystal

systems were first formally reported by Fedorov.[1] Crystalline compounds have physical

properties that can require the presence or absence of specific symmetry operations. The absence

of inversion symmetry centers is one condition that allows crystals to exhibit several interesting

and useful properties.[2] A crystal has inversion symmetry if there is any point within the unit cell

where, if you set that point as the origin with coordinates (0,0,0), then for every atom *n* with

coordinates (x_n,y_n,z_n) an equivalent atom can be found at $(-x_n,-y_n,-z_n)$. Points satisfying this

condition are called inversion centers. A crystal structure with no inversion centers is said to be Noncentrosymmetric (NCS), while those crystals with inversion centers are termed Centrosymmetric (CS) Figure 1.
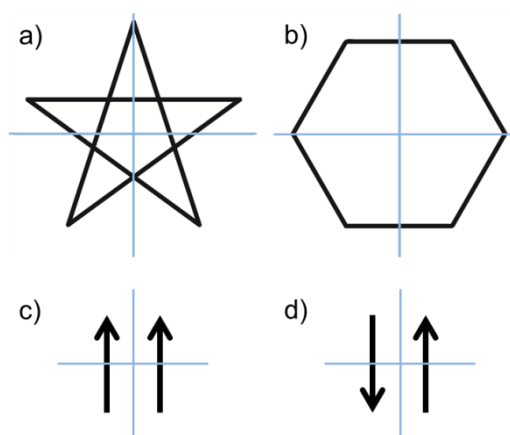
Figure 1: Two-dimensional examples of noncentrosymmetry (a, c) and centrosymmetry (b, d); Inverting the figures through the points indicated by the crossed blue lines produces no change in (b) or (d) while (a) or (c) would be reproduced upside down.

Experimentally, NCS crystals are much less common than CS crystals, despite the fact that most of the possible crystal systems are NCS.[3] Of the 32 crystal classes, 21 are NCS while 11 are CS, and of the 230 space groups, 138 are NCS while 92 are CS. NCS materials can exhibit nonlinear properties such as piezoelectricity, pyroelectricity, second harmonic generation (SHG), ferroelectricity, and optical activity.[4-9] Consequently, NCS materials are technologically important, and have many commercial and research applications including laser optics, energy generation, sensors, precision actuators, and data storage.[10-13]

Noncentrosymmetry occurs in crystals of organic and inorganic substances. NCS inorganic crystals have certain advantages over organic alternatives for practical applications.[14,15]

25

While the covalent bonds between the atoms of individual molecules are stronger than ionic

bonds, the intermolecular forces that bind the molecules to each other (e.g. hydrogen bonds,

dipole-dipole interactions, Van der Waals forces) in organic crystals are much weaker than the

ionic bonds present in inorganic crystals. One of the ways that this difference manifests itself is

in the much lower melting points of organic vs inorganic crystals. For SHG materials the optical

damage threshold and thermal stability values of inorganic materials are generally higher than

those for organic crystals. There are exceptions to this trend, such as L-arginine, which has a

higher optical damage threshold than potassium dihydrogen phosphate, though it also has lower

thermal stability.[16] NCS materials that are commercially useful are more likely to be inorganic

than organic in composition.
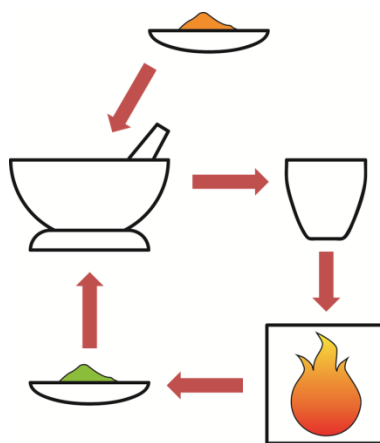
Figure 2: In a standard solid state synthesis reaction starting reagents are ground together using

a mortar and pestle to ensure a homogeneous mixture; the reagents are then transferred into a

crucible made of a material selected for thermal stability and inertness (often alumina or

platinum metal); the crucible, with the reagents inside, is then put into a furnace that is

programmed to go through a series of temperature changes called a "heating profile"; after

cooling, the product is extracted from the crucible; in many cases, the product will then be reground and the process will be repeated several times to improve yield.

1.4 Synthetic Methods

There are two primary synthetic methods used in the search for new inorganic NCS compounds: these are solid-state synthesis, and hydrothermal synthesis. Solid state synthesis involves grinding together powdered reagents and heating them to promote formation of a product phase Figure 2. Grinding and heating is often repeated several times for a single solid state reaction to improve yield. This technique produces samples that are frequently unsuitable for analysis by single crystal diffraction techniques, but are readily analyzed using powder diffraction techniques. The molar ratios of reagents used in solid state syntheses are selected so that the stoichiometry of the reaction sample (after heating) is the stoichiometry of the desired compound. Some reagents used in solid state syntheses release gases during the heating step (e.g. CO_2), and these experiments are often designed to take advantage of this effect.[17-19]

Hydrothermal synthesis involves combining reagents in water at temperatures in excess of 100 °C and pressures above 1 bar. Hydrothermal crystal growth is performed in an autoclave capable of withstanding the temperature and pressure of the reaction and with an interior liner that is inert to the reagents being used Figure 3. Similar conditions are produced by geological processes, and hydrothermal methods were first used to research the growth of geological crystals.[20,21] In response to an insufficient natural supply of quartz crystals for electronics components following World War II, A. C. Walker and E. Buehler at Bell Laboratories developed a commercial scale hydrothermal process for generating quartz crystals.[22] Hydrothermal crystal growth is now a common technique for synthesizing inorganic materials

for research purposes. When a solvent other than water is used the method is referred to as solvothermal synthesis. Conceptually solvothermal synthesis is identical to hydrothermal synthesis, but for safety reasons it is very important to take into account the chemical and thermodynamic properties of the solvent being used when setting up a reaction.

Hydrothermal conditions can be used to synthesize a broad variety of compounds, with widely varying temperature and pressure requirements. For the hydrothermal experiments discussed in this work, a stainless steel autoclave with a polytetrafluoroethylene (PTFE) liner, and reaction temperatures between 150 °C and 200 °C were used. These hydrothermal experiments also employ a slight modification to the standard method. Originally developed by Stucky and coworkers, the variation involves running multiple reactions at once in the same autoclave in individual heat-sealed PTFE pouches.[23,24] A 125 ml PTFE-lined autoclave can be used to simultaneously run up to 7 different reactions under temperature and pressure conditions that the researcher can be certain are identical to each other. Additionally, this method allows researchers to perform reactions using much smaller quantities of reagents than would be reasonable when employing the full autoclave chamber. Much of the synthetic research discussed here involves hydrofluoric acid, an extremely toxic and dangerous reagent, and decreasing the scale of the reactions helped to minimize the risk of toxic exposure without sacrificing scientific investigation.

The compounds investigated in my research are inorganic phases containing early transition metal oxide-fluorides (ETMOFs).[25,26] Transition metal oxides are the primary reagent sources of transition metals in hydrothermal synthesis reactions for ETMOFs. Some transition metal oxides are resistant to dissolution in almost all strong acids. Hydrofluoric acid a common

exception to this and can be used to mineralize most transition metal oxides.[27-29] Using

hydrofluoric acid to mineralize the transition metal oxide reagents has the added benefit that it

provides a source of fluoride anions for generating ETMOFs.
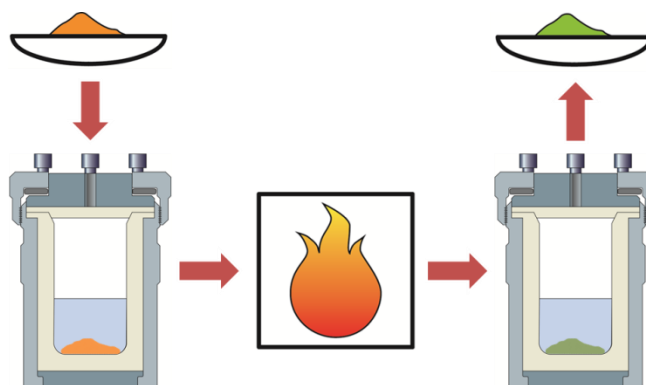
Figure 3: In a typical hydrothermal synthesis reaction the reagents are placed into a lidded PTFE

container slightly less than half filled with water, which is then put into a stainless steel

autoclave (shown schematically) that when closed, applies pressure to the PTFE container and

lid creating a sealed reaction space; the autoclave is then subjected to a heating profile, creating

temperature and pressure conditions inside of the autoclave that facilitate the formation of the

products; after cooling the products are usually separated from the reaction solution by vacuum

filtration.

1.5 New Materials Discovery

Despite the significant progress that continues to be made in the development of

theoretical and computational inorganic chemistry, synthetic investigation remains the dominant

driver in the search for, and discovery of, new NCS crystal compounds. While theoretical

methods have been used to predict potential new compounds, and the relative stability of

selected possible crystal phases for them, there are still challenges that must be overcome before such methods can be reliably used to discover new materials.[30-35] One challenge is that theoretical methods cannot reasonably be used to predict the relative stability of every one of the effectively infinite possible atomic arrangements for a given elemental composition.[36] Some set of criteria must always be used to select phases for evaluation, necessarily omitting other structures.[37]

The most significant barrier to application of theoretical methods for driving the discovery of new materials is that while theoretical models can be used to predict whether a compound will be stable with a certain structure, they cannot yet offer useful insights into what experimental conditions would lead to the formation of the predicted phase, or even whether any such conditions exist for that specific phase.[38,39] Experimentally synthesizing a theoretically predicted compound with a desired elemental composition and structure requires that the conditions needed for formation of the specific phase are identified. The stability of predicted phases should ideally be evaluated against the stability of possible combinations of phases that could form under the synthetic reaction conditions. This is a much more complicated question than individual phase stability, and while synthetic phase diagrams of many systems have been generated through experimental observations, and theoretical methods have recently been applied to generate some, the vast majority of synthetic composition and phase space is unmapped.[40,41] Until theoretical and computational approaches can address these details, discovery of new compounds will remain an experimentally dominated endeavor. There is a computation-based project working to accelerate synthetic discovery of new crystal materials by applying machine learning analysis to a database of unsuccessful, or "dark" reactions, and

predicting sets of new reaction conditions that are likely to generate some crystalline product.[39]

This is an important and useful development but, as the authors note, this is not the same as

predicting the conditions for formation of a specific compound or phase.

1.6 Anionic Group Theory

Synthetic investigations for the discovery of new materials benefit from the application of

concepts developed by analyzing existing materials. The development of predictive concepts

occurs through the process of abstraction and generalization, one of the cornerstones of any

scientific endeavor.

In the search for new NCS inorganic phases, and more specifically phases with polar

symmetry, a predictive concept that has been applied very successfully is based on Chen's

Anionic Group Theory (CAGT).[42-44] A crystal has polar space group symmetry when its

corresponding point group symmetry is polar (a point group is polar when every symmetry

operation leaves more than one point unchanged); there are 68 polar space groups, slightly more

than half of the 132 NCS space groups. Chen and colleagues showed that in polar crystal lattices

the presence of anionic subunits, individually possessing an intrinsic dipole, and having those

dipoles collectively oriented in the same direction often corresponded to the crystal exhibiting

high SHG efficiency. They found that the SGH efficiency could be expressed as a geometric sum

of second-order polarizability tensors for the anionic units themselves.[45] Collective alignment of

anionic unit dipoles within the lattice gives the bulk crystal a net dipole moment Figure 4. The

observations of CAGT can be applied as a guide to synthetic discovery. Intentionally

incorporating anionic units that possess an intrinsic dipole moment, when attempting to

synthesize new materials, is a successful strategy for discovering polar, NCS compounds.[45-51]

This approach has been particularly successful in its application to the discovery of new SHG-active borate compounds.[51-55]

New materials discovered by incorporating polar anions do not always have polar symmetry, but they do have an improved probability, when compared to materials that incorporate nonpolar anions, of having polar symmetry.[56-58] Compounds have been discovered with two kinds of polar anionic units that crystalize within the same structure, such as the compound $(Ag_3MoO_3F_3)(Ag_3MoO_4)Cl$ reported by Maggard in 2003.[59] The presence of two kinds of polar units greatly increases the likelihood that a crystal will form in a polar space group. There is an important distinction between the effects of polar and chiral units in crystals structures. Crystals that include only one enantiomer of a chiral molecule in their structures must always possess chiral symmetry, and therefore are NCS. Polar molecules or units that are not chiral do not have distinct enantiomers, and CS arrangements of polar molecules or units are common.[60] CS compounds that incorporate polar anions frequently have a dipole ordering that is anti-ferroelectric.[57] An example structure of this kind may have one-dimensional chains of aligned dipoles with neighboring chains exhibiting alignment in opposite directions so that their dipoles cancel as in Figure 4c.
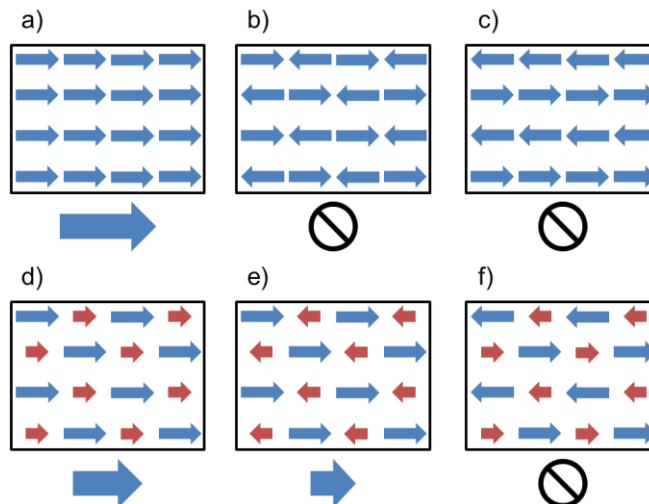
Figure 4: Dipolar anionic units (represented as arrows) in a crystal lattice contribute to the bulk dipole moment of the crystal. When the dipole vectors of the individual units align together (a), the bulk crystal has a polar moment and is therefore NCS. The dipole moments of the individual units can also order themselves with alignments that cancel each other (b and c), when this happens, the bulk crystal exhibits no net polar moment and is CS. In crystal systems with two kinds of polar unit (d, e, and f) the number of arrangements that result in a nonzero bulk dipole increases; (e) shows an anti-aligned arrangement that results in partial canceling of the dipole moments.

1.7 Polar d0 BBUs

Transition metals with distorted octahedral coordination are examples of the kinds of polar anions identified by CAGT.[61] Two effects can cause $[MO_6]$ anions (with M being an early transition metal) to exhibit distorted octahedral coordination, the Second Order Jahn-Teller (SOJT) and the Pseudo Jahn-Teller (PJT) effect.[62,63] The SOJT effect and PJT effect apply to d^0 and d^1 transition metals, respectively. In both cases the highest occupied and lowest unoccupied

orbitals (HOMO and LUMO) of the coordination complex are close enough in energy to interact, causing the metal atom to distort away from the center of its coordination polyhedron, toward a corner, edge, or face, breaking the coordination symmetry and removing degeneracy. All Jahn-Teller-type effects break symmetry to cause degenerate energy levels to split. The out-of-center distortion imparts a dipole moment to the anionic polyhedron. When this distortion breaks the crystal symmetry the direction of the distortion, and therefore the direction of the bulk dipole, can be changed by applying a sufficiently strong electric field. Polar perovskites (ABO_3), and related phases exhibit this kind of distortion and have been extensively studied for their ferroelectric properties.[64-69]

$$[M^nO_3F_3]^{(n-9)}$$
Face

$$[M^nO_2F_4]^{(n-8)}$$
Edge

$$[M^nOF_5]^{(n-7)}$$
Corner
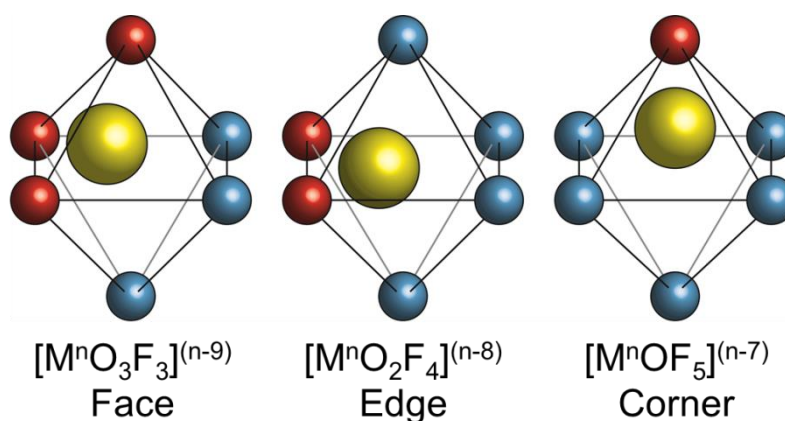
Figure 5: Octahedral anionic coordination complexes of early transition metals by oxide fluoride ligands exhibit out-of-center distortions in which the metal atom (yellow) distorts toward the oxide ligand(s) (red) and away from the fluoride ligands (blue). The number of oxygen atoms determines whether the distortion will be toward an octahedral face, edge, or corner, as indicated. This distortion gives these anionic units a dipole moment and makes them excellent building units for synthetic discovery of NCS phases following the guidelines suggested by CAGT.

Polar anionic units in ETMOF phases are comprised of transition metals having oxide and fluoride ligands, most frequently in octahedral coordination with the general formula $[MO_xF_{6-x}]^{n-}$.[56,70-74] In $[M^nO_xF_{6-x}]^{(n-(6-x))}$ octahedra the metal center distorts toward a corner (x=1), edge (x=2), or face(x=3) with the distortion directed toward the oxide ligands Figure 5.[28] These anions also exhibit polar distortion of their octahedral coordination environment, but unlike $[MO_6]$ octahedra, the out-of-center distortions of the metal in $[M^nO_xF_{6-x}]^{(n-(6-x))}$ anions are only rarely SOJT or PJT effects. In order for the out-of-center distortion to be a Jahn-Teller-type effect, the distortion must break the symmetry that would exist without the distortion. In most ETMOF compounds that symmetry is already broken. $[M^nO_xF_{6-x}]^{(n-(6-x))}$ ions can only have non-polar symmetry if a: x=2 and the two oxide ligands are trans to each other, or b: x=4 and the two fluoride ions are trans to each other. Some ETMOF crystals have one-dimensional chains of corner sharing $[MO_2F_4]$ octahedra where the oxide ligands occupy the shared corners (with the entire chain having the formula $[MOF_4]$).[75] In these cases a distortion along the chain axis is a SOJT effect.

1.8 Lambda Shapes

An expansion on the strategy of using polar anionic units to promote formation of NCS phases is the inclusion of what are called Λ-shaped polar anions.[26,76] The concept was first developed within the field of organic crystal growth, by Yamamoto et al.[77] "Λ-shape" is the term used to indicate that the physical structure of the unit is bent. The work reported that molecules exhibiting such shapes were more likely to pack together in NCS configurations because the most-dense packing motifs involved fitting each Λ-shaped unit into the next with their angles aligned. Martin Donakowski, in his work on the compound $CuVOF_4(H_2O)_6 \cdot H_2O$, reported an

extension of the Λ-shape effect into the field of inorganic crystal synthesis.[26] The effect is a result of steric influences from the building units and is independent of the dipole interactions that are often relied on to stabilize the ordering of polar anionic units. Examples of NCS oxide-fluoride materials that incorporate Λ-shapes include the compound $CuVOF_4(H_2O)_6 \cdot H_2O$ and the $K_{10}(M_2O_nF_{11-n})_3X$ compounds (X = F, Cl, Br, I; M= Nb, Mo).[76]

In order to apply this effect to the discovery of new NCS crystals, either the anion must have an intrinsic Λ shape, or the Λ-distortion must be caused by interactions between the anionic unit and its coordination environment. A Λ-distortion is intrinsic to an anionic unit when it results from interactions between the atoms that compose the unit, and is independent of external influences. Any such unit could likely be incorporated into many new structures through wide ranging synthetic investigation and the bent shape would be conserved in all of them. If an anionic unit has a Λ-shape that is caused primarily from interactions with its environment, synthetic incorporation of the unit into a new compound can occur with the anion in a linear conformation. Theoretical contributions to the work on the $K_{10}(M_2O_nF_{11-n})_3X$ compounds by the Seideman group found that the $[M_2O_nF_{11-n}]^{3-}$ anionic units would adopt linear configurations without the influence of their coordination environment.[76] While organic molecules with intrinsic Λ-type structures are common, the lack of covalent behavior (to give atomic interactions angle dependent character) in inorganic systems makes generating or discovering these kinds of anionic units a much greater challenge. In the inorganic Λ-shape containing compounds reported so far, the distortion in the anionic unit results from interactions with the coordinating environment. The distortion in the $K_{10}(M_2O_nF_{11-n})_3X$ compounds arises from interactions between the shared fluoride ligand in the $[M_2O_nF_{11-n}]^{3-}$ and coordinating potassium cations, and

in $CuVOF_4(H_2O)_6 \cdot H_2O$ the bent shape is caused by hydrogen bonding interactions. The scarcity of inorganic anionic units with intrinsic Λ-shapes limits the current applicability of this concept for discovering new NCS compounds.

1.9 Dimensionality

The octahedral ETMOFs and Λ-shaped polar, anionic units discussed above are both examples of 0-dimensional basic building units (BBUs), anionic building units that exist as isolated conserved species, smaller than the crystallographic unit cell. One-dimensional ETMOF anionic units consist of metal oxide-fluoride polyhedra in chains, linked together by shared ligands that extend indefinitely through the crystal in one direction. These chains still possess a charge formally described as the charge per repeating unit of the chain. Similarly there are materials with two-dimensional anionic units that consist of sheets extending through the crystal forming layered structures, and there are three-dimensional anionic frameworks such as the network of corner-shared MO_6 octahedra in perovskite lattices.

Oxide and fluoride anions, when part of a transition metal coordination polyhedron, interact with surrounding cations with very similar energetic relationships.[28,78] If an ETMOF anion is present in a crystal, the net change in energy associated with switching the orientation of the anionic unit is often relatively small, especially in compounds with zero-dimensional BBUs. In some of the oxide-fluoride compounds this leads to crystallographic disordering of oxide and fluoride sites. This is understood as disorder in the relative orientations of the polar axes of neighboring BBUs. Individual anionic units retain a fixed ratio of oxide and fluoride ligands, because the energetic cost of exchanging an oxide ligand for a fluoride ligand on one of the tightly bound zero-dimensional BBUs is high. ETMOF anionic units with disordered polar

orientations lose their collective polar moment, preventing them from giving the bulk crystal a net dipole. It is useful to find strategies for stabilizing orientational order of the anionic units when attempting to synthesize new NCS ETMOF phases.[79] If a crystal compound has ETMOF octahedra with 2 oxide and 4 fluoride ligands per metal center, every metal center is expected to coordinate with 2 oxide ligands and 4 fluoride ligands even in disordered phases. The disorder reflects the uncertainty in identifying which 2 of the 6 ligand sites around a metal center are occupied by oxygen atoms. For zero-dimensional ETMOF octahedral anions, oxide ligands are frequently oriented trans to a fluoride ligand, making the anions polar.[28] The different possible orientations of such octahedra that maintain the approximate positions of the ligands determines the number of orientational microstates (for $[MOF_5]$ there are 6, for $[MO_2F_4]$ there are 12, and for $[MO_3F_3]$ there are 8). Experimental investigations of the order-disorder transition behavior of ETMOF compounds have demonstrated a loss of polar symmetry in response to increasing temperature.[80]

Differentiating oxide and fluoride sites when solving a crystal structure is challenging, even when they are well ordered, and high quality single crystal diffraction data is necessary.[78,79] Assignment of oxide and fluoride sites is achieved by a combination of structure refinement and bond valence sum analysis using the refined bond lengths.[70]

Cations that coordinate to the ETMOF anionic units play an important role in promoting O/F site order.[58] One method that our group has used for promoting O/F site ordering takes advantage of an effect analogous to hard-soft acid base theory.[70,81] By coordinating two monatomic cation species with an anionic unit, preferential interactions of one cation with the oxide ligands and the other with the fluoride ligands can lead to ordering. An example of this

effect is the ordered bilayer of the rutile-type structure seen in $AgNa(VO_2F_2)_2$, in which silver cations coordinate with oxide ligands and sodium cations coordinate with fluoride ligands.[81] The out of center distortions of the anionic units change the "hardness" of the ligand ions. Oxide ions become harder and fluoride ions become softer influencing their coordinating interactions with the cation lattice.[28] Another example of this kind of effect is the local ordering reported in nickel and manganese doped samples of $LiCoO_2$, where Ni^{2+} and Mn^{4+} ions were found to occupy sites close to each other.[82]

Chapter 2

2.1 Inorganic Crystal Structure Analysis

Experimental methods of analyzing crystalline materials are understandably important to the characterization of sample compositions, structures, and properties. Spectroscopic methods, magnetic behavior characterizations, elemental analyses, conductivity measurements, calorimetric experiments, and elastic response measurements all provide useful and important information. Diffraction techniques are the dominant experimental methods in the field of solid state inorganic materials research. Powder x-ray diffraction is used primarily for known-phase identification and analysis of sample purity. Determination of the atomic structure of crystals is (ideally) achieved by matching single crystal diffraction data, however, powder diffraction methods are sometimes used for this purpose when single crystals of a sample are unobtainable.

Structure and elemental composition determine the properties of a sample, and understanding structure-property relationships is a major goal of solid state chemistry. Another focus of solid state chemistry is developing an understanding of those rules that govern the manner in which elemental composition and synthetic conditions determine the atomic structures of materials. Methods for evaluating atomic interactions within known structures, such as the bond valence sum method, crystal field theory, and the Kapustinski equation, are useful tools for these endeavors.

2.2 Bond Valence Sums

In order to develop a detailed understanding of solid state crystal structures, methods of conceptual analysis that extend beyond crystallographic structure solutions are required. A

familiarity with the relationships between compositions, structures, and properties is built by developing and applying both quantitative and qualitative conceptual models to known systems. Identification of crystal structures is necessary, but not sufficient, for developing the level of intuitive understanding about atomic crystal systems that enables an experienced researcher to make useful predictions about the properties of possible new or unexamined compounds. Developing and using conceptual frameworks to generate explanations for the observed behaviors of materials, researchers make advances to scientific understanding in this field and are able to identify and exploit trends in the relationships between elemental compositions, crystal structures, and material properties.

One very powerful conceptual analysis method for understanding crystal structures is the bond valence method. Developed in its modern form by I.D. Brown, this method evaluates bonding interactions between neighboring atoms using a simple function of bond length and enables semi-quantitative evaluation of individual bonds to determine the relative stability of atoms in their respective sites.[83,84] The bond valence method is empirical, and employs parameters that have been derived using available experimental data. The first extensive set of parameter values was published by Brown and Aldermatt in 1985, and many additional parameters were developed and reported in 1991 by Brese and O'keefe.[85,86] The concepts involved are an extension of Pauling's electrostatic valence rule and the experimentally observed relationships between bond length and bond strength.[87] The bond valence method defines the "valence" of a bonding interaction between atoms i and j to have a numerical value given by eqn. 1.

$$v_{ij}(r) = e^{\left(\frac{R_{ij}-r}{b_{ij}}\right)}$$

eqn. 1

In eqn. 1 r is the interatomic distance, and R_{ij} and b_{ij} are empirical parameters specific to the i-j bond type, the R_{ij} parameter represents the characteristic bond length at which the valence of the bond has a value of exactly 1, and b_{ij} is a term that describes the bond "hardness" and is most often assigned a value of 0.37. A large collection of published R_{ij} and b_{ij} parameters for various bond types developed using various methods has been compiled by Brown and is made available by the IUCr on their website.[88]

The valence value of a bond is related to its strength and is closely connected to the concept of bond order.[89] The valence of a bond contributes its value to the valence sum of both participating atoms. Using bond valence method to analyze an individual ion site is done by calculating valence values for all of the atom's bonding interactions and summing them. The Bond Valence Sum (BVS) thus obtained can be used to evaluate both the formal oxidation state of an atom site and its relative stability in its present coordination environment.[84] The BVS of an ion rounded to the nearest integer is expected to be the nominal valence state of that ion, which is equal to the absolute value of the formal oxidation state for that ion (as long as the correct set of parameters is being used).

Bond valence parameters are frequently oxidation state specific, making it possible to evaluate the oxidation state assigned to an atom by comparing BVS values calculated using several sets of parameters. The absolute value of the difference between the BVS and the nominal valence is inversely related to the stability of that atom in its coordination environment.

For a complete crystal structure, a Global Instability Index (GII) can be calculated from the BVS values for all of the individual ions.[90] The GII can be used to assign a numerical value to the stability of crystal structures (according to the bond valence method) and to evaluate the relative stabilities of different phases of polymorphic compounds.

Calculations necessary for analysis of structures by the bond valence method are very straightforward and the complete bond valence description of a relatively complicated crystal structure can be generated from a list of bond lengths in as little as a few minutes using a computer. Nevertheless, the method has several limitations of which a user should be aware. The bond valence method does not account for anion-anion or cation-cation interactions and therefore is very difficult to effectively apply to generalized structure optimizations. On first learning to apply the bond valence method it appears that structure optimization should be a natural extension that would allow a broader range of applications. The method possesses insufficient complexity of interactions to generate realistic forces, and new interaction terms need to be developed, parameterized, and added to the bond valence method framework in order to apply its concepts to structure optimization problems.[91] The program SPUDS does use bond valence calculations for a specific kind of structure optimization, but it necessarily imposes many additional constraints on the symmetry of the structure, limiting the use of the program to very specific systems.[92] Additionally, the valence values are only indirectly related to bond and site energies. This greatly complicates adapting the bond valence method to predict elastic properties of crystals.

The bond valence method has its primary application in explaining crystal structure behavior from a qualitative standpoint.[70,76,93,94] Variations in bond lengths and atomic positions

between related structures or between different sites in the same structure can often be described

from the point of view of satisfying the BVS requirements of every atom in the structure

simultaneously. For example, the polarizing out of center distortions of the metal cations in

ETMOF octahedral anions can be understood as arising from the increased BVS requirement of

the oxide anions (2) over the fluoride anions (1).[28] Additional and interesting new applications of

the method have been developed in recent years. One of these is a technique, developed by S.

Adams, for identifying ion transport pathways through intercalation compounds such as the

lithium ion battery cathode material $LiFePO_4$ by finding the path of least valence change for the

ion.[95,96]

2.3 Size-Site Mismatch

Observing and analyzing the details of many crystal structures enables the identification

of trends. One such trend is that symmetry breaking distortions in crystal lattices have a tendency

to center around an atom that behaves as if it is "too small" for its coordination environment, so

that there is a size-site mismatch.[97] In bond valence terms such an atom is "under-bonded". This

concept can describe the out-of-center distortions observed in the octahedral anionic units of

early transition metal oxides and oxide-fluorides, which impart a dipole moment to the

octahedral unit. Glazer-type tilting effects observed in perovskites also fit this trend.[98] In

perovskites (with general formula ABX_3), using the rigid octahedra model when the A-site cation

is too small for its 12-fold coordination environment, tilting of the BX_6 octahedra shrink the

coordination environment around the A-site without significantly changing the B-site

coordination or bond lengths. This concept can also explain the distortion in the perovskite

related $KCuF_3$, with a structure that can be described as having tilted 12 coordinate A-sites

instead of tilted 6 coordinate B-sites. The size-site mismatch trend suggests that intentionally synthesizing compounds where ions are made to occupy sites for which they are too small could reliably lower the symmetry of the resulting crystal, and could be applied to improve the chances of forming new noncentrosymmetric phases.

2.4 Predictive Modeling

The complexity of three dimensional interatomic interactions makes computational methods invaluable for interpreting and predicting atom-scale behavior in detail. Crystal phase formation is an example of an emergent behavior. There are an enormous number of possible packing arrangements of atoms in crystal lattices.[99] The packing arrangements adopted by specific systems can often be predicted intuitively when enough is known about closely related systems. Many new compounds and structures are discovered using intuition and experience with similar compounds. Experience based predictions are harder to make for complex systems and for those systems that have not been well investigated. In general, predicting which possible structure a given composition might adopt is the most stable requires computational approaches. Dynamic behavior is also an emergent property and is even more difficult to predict. Investigating emergent behaviors is really only made possible with the aid of computers. Computational methods for this purpose use mathematical models composed of functions that are intended to mimic the interactions between individual atoms, as well as the influences from applied external conditions. Models are either developed on the basis of ab initio theoretical calculations, or else they are constructed by parameterizing functions empirically to fit experimental results.

2.5 Ab Initio Models

Many computational investigations employ some variety of *ab initio* quantum chemistry methods to calculate lattice energies, elastic-properties, and electro-optical properties of crystals. Quantum computational methods, such as density functional theory (DFT), are primarily focused on electron behavior. In order to simplify the quantum mechanical calculations, these methods parameterize the behaviors of atoms' inner shell electrons and apply crystal symmetry rules to limit the number of variables and the computational costs. Ab initio methods can be applied to fixed experimental crystal structures to calculate lattice energies and predict electronic orbital density of states. These methods are often moderately successful at predicting electronic band energies in crystalline semiconductors.[100] Optical and electrical properties obtained by ab initio calculations frequently show good agreement with experimental values.[101] When used for predicting the equilibrium atom positions and elastic properties for solid state crystal structures, ab initio methods are not yet accurate at reproducing experimental values.[102,103]

When symmetry constraints on a modeled crystal are removed or a system of interest is stoichiometrically complex, ab initio predictions of equilibrium structures rapidly become more computationally expensive to obtain and less reliable. Equilibrium unit cell volumes of even high symmetry inorganic compounds predicted using *ab initio* methods nearly always differ from the available experimental values by at least 5%, and often significantly more.[40,41] This level of accuracy is frequently reported in publications as being "in good agreement with experiment." Bulk modulus predictions are far less accurate, often disagreeing with experiment values by as much as 50%.[104] The limits of predictive accuracy of ab initio methods for crystal dimensions and elastic properties does not prevent them from predicting the relative stabilities of selected

crystal phases with reasonable accuracy, but it does negatively impact the reliability of dynamic simulations. The large computational cost for applying such methods to systems in low symmetry conditions also makes ab initio simulations less attractive for simulating unconstrained transitions or phase forming reactions in the solid state.[105]

2.6 Empirical Models

In contrast to the fully theoretical nature of ab initio computational methods, there exist a slew of empirical quantitative computational approaches to modeling and analyzing atomic systems.[106-109] These approaches use parameterized functions to construct a model that reproduces selected experimental properties of the system being investigated. The functions used in an empirical model are often selected so that the parameters can be interpreted as established statistical or experimental quantities, such as ionic radius, electronegativity, or free-ion polarizability.[110] While this is common, it is not strictly necessary, and empirical models with parameters that are entirely arbitrary are also allowed.

Any model intended to reproduce the atomistic behavior of a system requires some form of interatomic interaction functions. For empirical models, these are the functions that must be parameterized. A variety of interatomic potential forms exist and they are discussed in more detail in chapter 6.

Empirical modeling of systems is often used for Monte Carlo and Molecular Dynamics (MD) simulations, both of which are methods that can be applied to explore the energy landscape of the configuration space of solid-state systems.[111-114] The computational power required for

these methods is high, as few crystallographic symmetry constraints are applied to the simulated systems and every atom is treated as an independent particle.

Empirical models of inorganic crystals tend to reproduce experimental behavior very well, but only when the simulation conditions (e.g. temperature and pressure) are very close to the experimental conditions of the fit experimental data.[105,115-118] As the simulated conditions diverge from the fit data conditions, empirical models tend to simulate behavior that deviates from experimentally observed behavior, giving an empirical model a "window" of conditions that it can reliably simulate. Consequently, empirical models usually lack transferability (compared to ab initio models), meaning that the components of a model that successfully predicts the behavior of one compound cannot be reliably applied to model another compound. This is in contrast to the accuracies of ab initio predictions, which are less intimately related to the system conditions and have better transferability.

Chapter 3

3.1 $K_{10}(M_2O_nF_{11-n})_3X$

One variety of anionic building unit found capable of adopting a Λ-shape is the bimetallic

$[M_2O_nF_{11-n}]^{3-}$, consisting of two transition metal oxide-fluoride octahedra with a shared corner.

Previous work by Udovenko and Laptash, among others, produced a variety of compounds

containing these bimetallic units with examples of both linear and lambda-shaped

conformations.[119-122] The previously reported crystal compounds are summarized in Table 1.

These compounds are structurally very similar to each other but belong to several different space

groups, some of them being polar. An earlier chapter discussed the role of the coordination

environment in inducing lambda distortions in otherwise linear anionic units. In this chapter I

will discuss how the coordination environment and the bonding within the anionic unit can

interact to cause a lambda distortion.

Table 1: Previously reported compounds with $[M_2O_nF_{11-n}]^{3-}$ units.

Compound	Space Group	Citation
$(NH_4)_5Nb_3O_3F_{14}\cdot H_2O$*	$P6_3mc$	119
$K_5Nb_3O_3F_{14}\cdot H_2O$*	$P6_3mc$	119
$Rb_5Nb_3O_3F_{14}\cdot H_2O$*	$P6_3mc$	119
$Cs_5Nb_3O_3F_{14}\cdot H_2O$*	$P6_3mc$	119
$(NH_4)_3(Mo_2O_2F_9)$	$P\bar{3}m1$	120
$Rb_{10}Nb_6O_7F_{26}\bullet H_2O$	P3	121
$K_{10}(Nb_2O_2F_9)_3F$	$Pmn2_1$	122
$(NH_4)_{10}(Nb_2O_2F_9)_3F$	$P\bar{3}m1$	122
$Rb_{10}(Nb_2O_2F_9)(F_2Cl)_{1/3}$	$P\bar{3}m1$	122
$Rb_{10}(Mo_2O_4F_7)_3F$	$P\bar{3}m1$	122
$Rb_{10}(W_2O_4F_7)_3F$	$P\bar{3}m1$	122

This research shows that a lambda-type distortion of the $[M_2O_nF_{11-n}]^{3-}$ building units in compounds with the general formula $K_{10}(M_2O_nF_{11-n})_3X$ where (M = V^V, Nb^V, n = 2; M = Mo^{VI}, n = 4; $X^- = (F_2Cl)_{1/3}$, Cl, $([Br][Br_3])_{1/2}$, and $([I][I_3])_{1/2}$) occurs in cases where the bridging ligand in the building unit is under-bonded. Concepts from the bond valence method are used to explain the origin of the Λ-distortion in the anionic units of these compounds. This family of compounds also acts as an example of drastic changes in crystal symmetry that can arise from very small changes in relative atomic positions.

From this research we discovered and reported 8 new compounds listed in Table 2 and Table 3. Collectively with those listed in Table 1 these comprise a fairly robust family of compounds with similar crystal structures. There are 3 primary space groups represented in this family of compounds, one of which has polar symmetry, and an additional 2 space groups that are only observed in one case each. Despite this diversity of crystal symmetries, as Figure 6 illustrates, the various structures have nearly identical connectivity and can be considered pseudosymmetrical. Λ-distortions are observed in some of the compounds, but not in all of them. Also, though Λ-distortions of bimetallic units are present in all of the polar compounds, some of the non-polar compounds have Λ-distorted units as well as linear ones. Figure 7, Figure 8, and Figure 9 are visual depictions of example unit cells for the three space groups adopted by the newly reported compounds (*P*3*m*1, *Pmn*2$_1$, and *C*2/*m*).

Table 2: Crystallographic parameters for compounds 1 – 4.

Compound	1	2	3	4
Formula	$K_{10}(V_2O_2F_9)_3(F_2Cl)_{1/3}$	$K_{10}(V_2O_2F_9)_3([Br][Br_3])_{1/2}$	$K_{10}(Mo_2O_4F_7)_3Cl$	$K_{10}(Nb_2O_2F_9)_3Br$
Empirical formula	Cl F83 K30 O18 V18	Br2 F27 K10 O6 V6	Cl F21 K10 Mo6 O12	Br F27 K10 Nb6 O6
Formula weight (g/mol)	3990.37	1465.44	1593.28	1637.52
Temperature	100.07 K	100.02 K	100.02 K	100.0 K
Wavelength	0.71073 Å	0.71073 Å	0.71073 Å	0.71073 Å
Crystal system	Trigonal	Monoclinic	Orthorhombic	Orthorhombic
Space group	$P\bar{3}m1$	$C\,2/m$	$Pnn2_1$	$Pnn2_1$
Unit cell dimensions	a = 19.2623(6) Å, α = 90.00° b = 19.2623(6) Å, β = 90.00° c = 7.7318(2) Å, γ = 120.00°	a = 11.2978(3) Å, α = 90.00° b = 19.1761(5) Å, β = 93.2470(10)° c = 7.7624(2) Å, γ = 90.00°	a = 19.907(2) Å, α = 90.00° b = 7.7643(10) Å, β = 90.00° c = 11.2139(14) Å, γ = 90.00°	a = 20.1125(11) Å, α = 90.00° b = 7.7382(4) Å, β = 90.00° c = 11.4797(6) Å, γ = 90.00°
Volume	2484.43(13) Å³	1679.01(8) Å³	1733.3(4) Å³	1786.64(16) Å³
Z	1	2	2	2
Density (calculated)	2.667 g/cm³	2.899 g/cm³	3.053 g/cm³	3.044 g/cm³
Absorption coefficient	3.085 mm⁻¹	5.394 mm⁻¹	3.537 mm⁻¹	4.308 mm⁻¹
F(000)	1892	1378	1488.2	1524.1
Crystal size	0.457 x 0.12 x 0.12 mm³	0.26 x 0.17 x 0.14 mm³	0.55 x 0.153 x 0.06 mm³	0.26 x 0.22 x 0.19 mm³
θ range for data collection	1.22 to 30.12°	2.09 to 26.37°	2.05 to 33.14°	2.03 to 30.03°
Index ranges	-26<=h<=27, -25<=k<=27, -10<=l<=10	-14<=h<=14, 0<=k<=23, 0<=l<=9	-30<=h<=30, -11<=k<=10, -17<=l<=17	-28<=h<=21, -8<=k<=10, -16<=l<=15
Reflections collected	24701	2357	94133	24101
Independent reflections	2642 [R$_{int}$ = 0.0760]	2689 [R$_{int}$ = 0.0000]	6671 [R$_{int}$ = 0.0718]	5269 [R$_{int}$ = 0.0223]
Completeness	99.8%	99.8%	99.9%	99.8%
Data / restraints / parameters	2642 / 0 / 139	2689 / 0 / 132	6671 / 1 / 273	5269 / 1 / 242
Goodness-of-fit	1.132	1.157	1.033	1.170
Flack Parameter	-	-	0.01(6)	0.09(1)
Final R indices [>2σ(I)]	R$_{obs}$ = 0.0613, wR$_{obs}$ = 0.1754	R$_{obs}$ = 0.0332, wR$_{obs}$ = 0.0911	R$_{obs}$ = 0.0425, wR$_{obs}$ = 0.1109	R$_{obs}$ = 0.0290, wR$_{obs}$ = 0.0843
R indices [all data]	R$_{all}$ = 0.0623, wR$_{all}$ = 0.1774	R$_{all}$ = 0.0362, wR$_{all}$ = 0.0977	R$_{all}$ = 0.0452, wR$_{all}$ = 0.1130	R$_{all}$ = 0.0292, wR$_{all}$ = 0.0844
Extinction coefficient	None.	None.	0.0012(2)	None.
Largest diff. peak and hole	2.669 and -1.301 e·Å⁻³	2.148 and -3.128 e·Å⁻³	2.949 and -1.217 e·Å⁻³	2.560 and -1.287 e·Å⁻³

Table 3: Crystallographic parameters for compounds 5 – 8.

Compound	5	6*	7	8
Formula	$K_{10}(Nb_2O_2F_9)_3([Br][Br_3])_{1/2}$	$K_{10}(Mo_2O_4F_7)_3([Br][Br_3])_{1/2}$	$K_{10}(Nb_2O_2F_9)_3([I][I_3])_{1/2}$	$K_{10}(Mo_2O_4F_7)_3([I][I_3])_{1/2}$
Empirical formula	Br2 F27 K10 Nb6 O6	Br2 F21 K10 Mo6 O12	F27 I2 K10 Nb6 O6	F21 I2 K10 Mo6 O12
Formula weight (g/mol)	1717.34	1717.46	1811.26	1811.31
Temperature	99.99 K	99.99 K	299 K	99.97 K
Wavelength	0.71073 Å	0.71073 Å	0.71073 Å	0.71073 Å
Crystal system	Orthorhombic	Orthorhombic	Orthorhombic	Orthorhombic
Space group	$Pmn2_1$	$Pmn2_1$	$Pmn2_1$	$Pmn2_1$
Unit cell dimensions	a = 20.0790(6) Å, α = 90.00° b = 7.7588(2) Å, β = 90.00° c = 11.4828(4) Å, γ = 90.00°	a = 20.0790(6) Å, α = 90.00° b = 7.7580(2) Å, β = 90.00° c = 11.4836(3) Å, γ = 90.00°	a = 20.3471(6) Å, α = 90.00° b = 7.8376(3) Å, β = 90.00° c = 11.6367(3) Å, γ = 90.00°	a = 20.0720(8) Å, α = 90.00° b = 7.7549(3) Å, β = 90.00° c = 11.4644(4) Å, γ = 90.00°
Volume	1788.80(9) Å³	1788.83(8) Å³	1855.73(10) Å³	1784.51(12) Å³
Z	2	2	2	2
Density (calculated)	3.188 g/cm³	3.189 g/cm³	3.241 g/cm³	3.371 g/cm³
Absorption coefficient	5.419 mm⁻¹	5.587 mm⁻¹	4.734 mm⁻¹	5.092 mm⁻¹
F(000)	1594.1	1594	1666	1665.9
Crystal size	0.14 x 0.07 x 0.06 mm³	0.147 x 0.069 x 0.044 mm³	0.163 x 0.103 x 0.037 mm³	0.26 x 0.07 x 0.03 mm³
θ range for data collection	2.03 to 31.00°	2.03 to 38.66°	2.00 to 29.18°	2.03 to 30.03°
Index ranges	-29<=h<=29, -11<=k<=11, -16<=l<=16	0<=h<=35, 0<=k<=12, 0<=l<=20	-27<=h<=27, -10<=k<=10, -15<=l<=15	-28<=h<=28, -10<=k<=10, -16<=l<=16
Reflections collected	8796	5391	48327	72517
Independent reflections	8796	5391	5149	5358
Completeness	96.5%	99.6%	100%	100%
Data / restraints / parameters	8798 / 2 / 251	6426 / 1 / 250	5149 / 1 / 250	5358 / 2 / 255
Goodness-of-fit	1.174	1.231	0.949	1.067
Flack Parameter	-0.04(7)	0.03(3)	-0.10(4)	0.00(8)
Final R indices [>2σ(I)]	R_{obs} = 0.0305, wR_{obs} = 0.0835	R_{obs} = 0.0434, wR_{obs} = 0.1385	R_{obs} = 0.0434, wR_{obs} = 0.1028	R_{obs} = 0.0427, wR_{obs} = 0.1152
R indices [all data]	R_{all} = 0.0326, wR_{all} = 0.0850	R_{all} = 0.0467, wR_{all} = 0.1421	R_{all} = 0.0593, wR_{all} = 0.1088	R_{all} = 0.0470, wR_{all} = 0.1186
Extinction coefficient	None.	None.	None.	None.
Largest diff. peak and hole	1.385 and -1.282 e·Å⁻³	3.989 and -4.609 e·Å⁻³	2.432 and -2.330 e·Å⁻³	5.545 and -2.117 e·Å⁻³

* subcell approximation of commensurate structure.
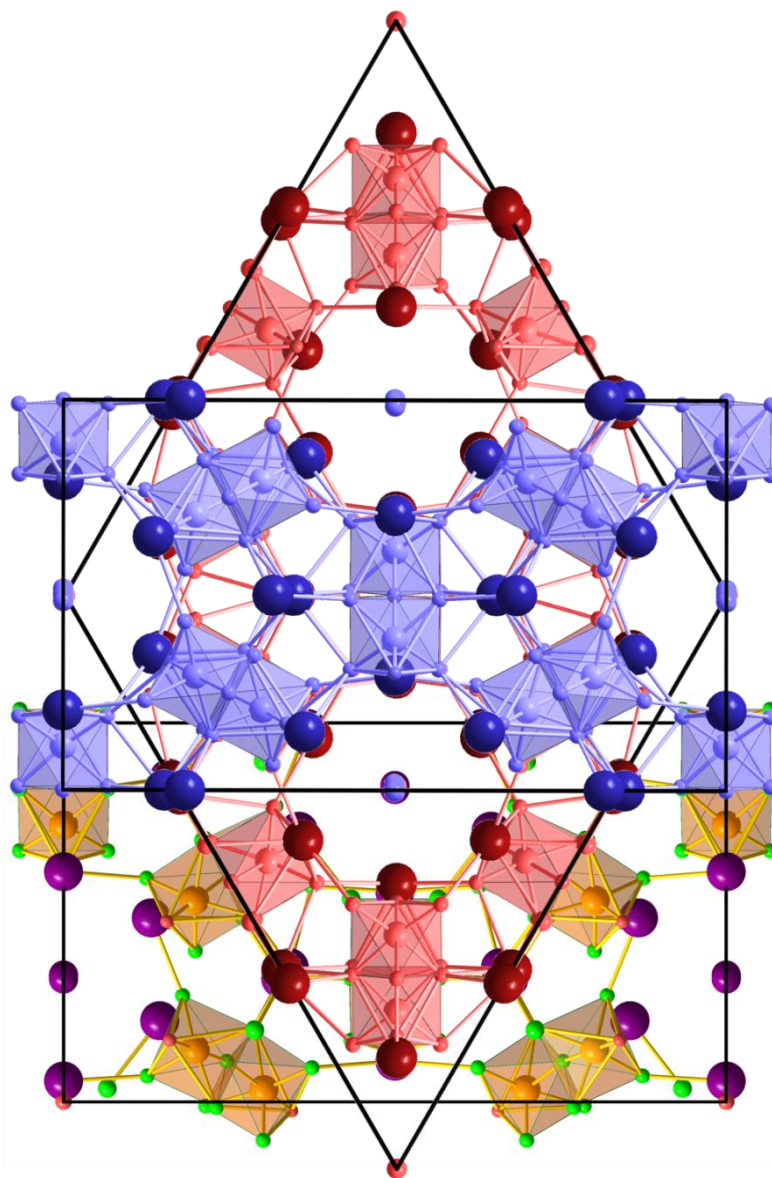
Figure 6: An overlap comparison of the three structure types of the 8 compounds reported. Their pseudo-symmetric relationship can be clearly observed. The trigonal $P3m1$ phase is shown in red, the monoclinic $C2/m$ phase is colored blue and the orthorhombic $Pmn2_1$ phase is shown with the colors used in **Figure 8**. The "real" differences in packing between the trigonal, monoclinic, and orthorhombic phases are subtle, but result in drastically different symmetry properties.
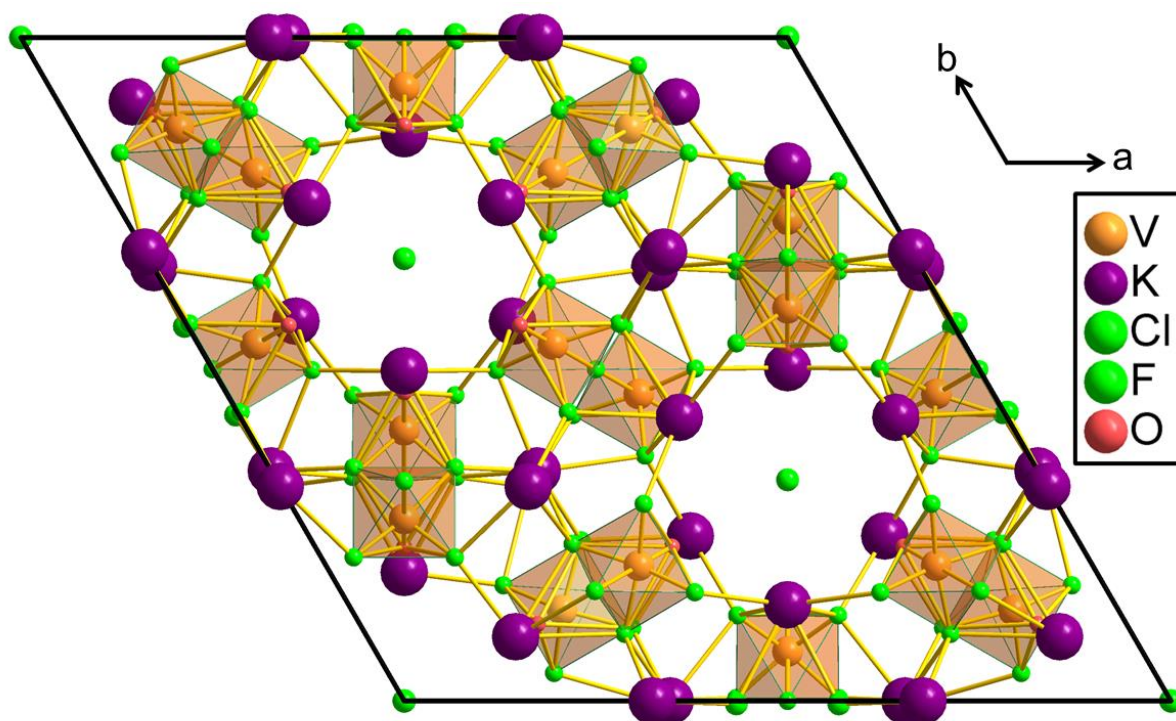
Figure 7: The trigonal structure of Compound 1: $K_{10}(V_2O_2F_9)_3(F_2Cl)_{1/3}$ which crystallizes in the $P\overline{3}m1$ space group. There are three halide channels (oriented along the c axis) in the unit cell, one at the cell corners and two within the body. The two channels within the body of the unit cell are disordered fluoride-containing channels while the channel at the corners is a well-ordered chloride ion channel.
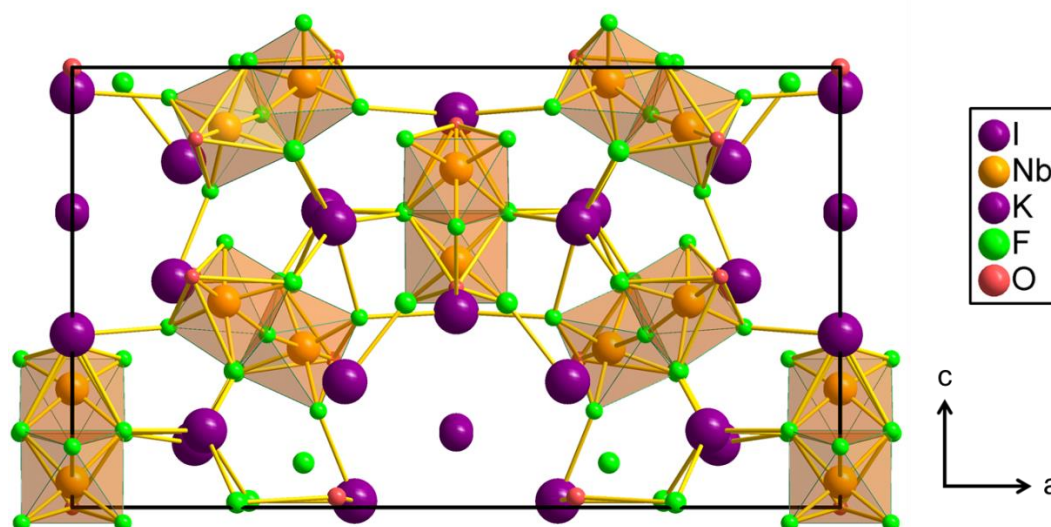
Figure 8: The orthorhombic *Pmn*2$_1$ structure of compounds 3 – 8, using compound 7 as the specific example. The halide ion channels in these phases are disordered down the *b* axis. There is additional disorder in compounds 3, 6, and 8 that results from the additional oxide ligands in the building unit. That disorder is not depicted in this figure.
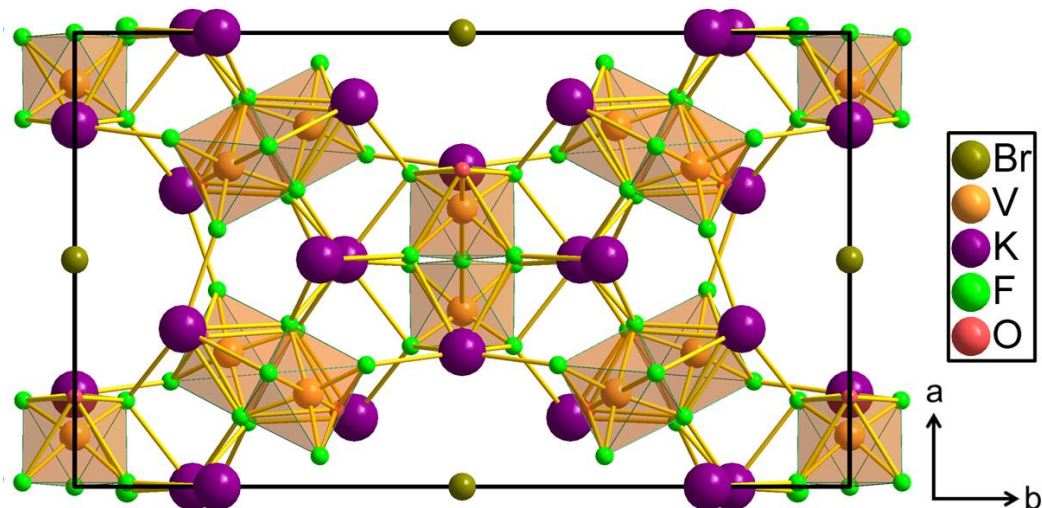
Figure 9: The monoclinic structure of compound 2: $K_{10}(V_2O_2F_9)_3([Br][Br_3])_{1/2}$ which adopts the $C2/c$ space group symmetry. The halide channels are oriented along the c axis and contain a disordered mixture of bromide and tribromide anions.

To explain the Λ-distortion from a bond valence method perspective we employ the distortion theorem.[123] The distortion theorem describes a consequence of the exponential relationship between bond length and bond valence and can be stated: *For multiple bonds of the same type to a central atom, any deviation of the lengths of bonds from the average increases the total valence contribution assuming that the average bond length stays constant.* Or: *For a set of bonds with a fixed average bond length, the minimum bond valence contribution occurs when all bonds are exactly equal to the average.* The valence contribution from a bond changes faster when the bond is shortened than when the bond is lengthened. The Λ-distortions in these materials increase the valence contributions from coordinating K^+ cations on bridging fluoride ligands in the bimetallic anion units (Figure 10).

In an earlier chapter I discussed the concept of the how a size-site mismatch can lead a too-small atom to undergo an out-of-center distortion. The distortion theorem is an alternative method for describing the same effect within the framework of the bond valence method. An under-bonding coordination environment is equivalent to a too-large site. Just as the too-small atom in the too-large site will shift away from the central position, an under-bonded atom in a symmetrical coordination environment will, by shifting away from the central position increase the net valence contribution it receives.

It is possible to use the distortion theorem to explain the octahedral tilting effect observed in some ABX_3 perovskite systems. In these systems the observed tilting of BX_6 octahedra increase the net valence on the under-bonded A-site cation by bringing some of the X anions closer to the A-site while moving others further away. This allows the A-site cation to fulfill its valence without changing the valence of the B-site cation. This effect is reversed in the case of the perovskite $KCuF_3$.[124] The structure of this compound can be interpreted as a tilting of the $[KF_{12}]$ coordination polyhedron, which maintains a regular coordination geometry and valence sum, while the Cu B-site cation increases its valence by shortening 4 bonds and lengthening 2. The distortion of the $[CuF_6]$ octahedral unit is more fundamentally understood as resulting from the strong Jahn-Teller distortion effect associated with Cu^{2+}.[125] Although the Jahn Teller effect is a consequence of degenerate electronic orbital interactions, which are not considered by the bond valence method at all, the bond valence method offers an explanation in its own terms for the associated distortion.
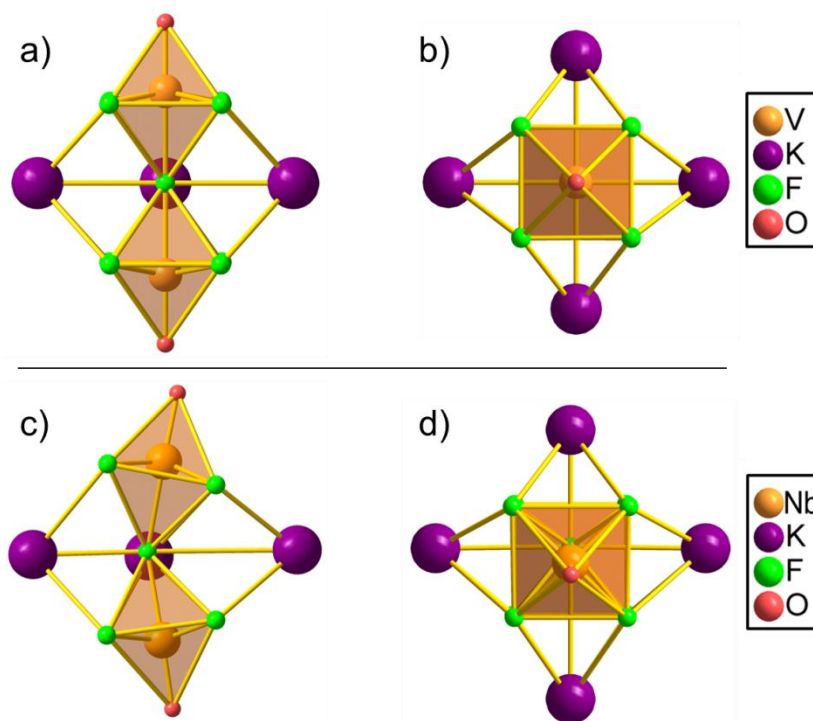
Figure 10: a) A linear, vanadium-containing, anionic building unit. The bond angle of V-F-V is 180º (under symmetry constraints). b) The same anionic unit viewed down the V-F-V axis; the coordinating potassium cations are arranged symmetrically around the linear anionic unit. c) View of a Λ-shaped, niobium-containing, anionic building unit. The bridging fluoride anion distorts to coordinate more closely with one of the potassium cations, giving rise to the Λ-angle. d) The same unit viewed down the Nb-F-Nb axis; the coordinating potassium cations are less symmetrically arranged about the bent unit as a result of the distortion.

In the compounds discussed in this research, the bridging fluoride ligand of the bimetallic $[M_2O_nF_{11-n}]^{3-}$ anions must satisfy part of its valence requirement by bonding to four K^+ cations that coordinate about the middle of the anion. When the transition metal in the unit is vanadium, the coordinating K^+ cations are able to sit close enough to the bridging fluoride anion that its valence requirement is sufficiently filled without distorting. When the transition metal in the

anionic unit is Nb or Mo the increase in the length of the bonds between the metal and the non-bridging fluoride ligands causes a larger average distance between the bridging fluoride and the K^+ cations. This increase in the average distance to the four coordinating K^+ cations lowers their valence contribution, and the bridging fluoride ligand distorts away from its central position to increase the net valence contribution as described by the distortion theorem.[123]

An interesting feature of these materials is the presence of highly disordered halide ion channels that, in some of the compounds, are occupied by a combination of linear polyhalide anions and monatomic halide anions, while in the other compounds they only contain monatomic halide anions. The highly disordered nature of these anion channels suggests that this set of compounds may have practical applications as solid state anion conductors.

Early difficulty in solving the crystal structure of the compound $K_{10}(Nb_2O_2F_9)_3([I][I_3])_{1/2}$ was exacerbated by the disorder of the halide ion sites in the channels. We initially attempted to solve the structure using the formula $K_{10}(Nb_2O_2F_9)_3I$. When we attempted to refine partial occupancies of iodine sites, results would indicate that the net iodine occupancy in the channels was twice our expected value. The refinement indicated each channel would have two iodine atoms per unit cell. The channels are oriented along the b axis, giving a linear concentration of ~3.919 Å per iodine. If the indicated concentration of iodine atoms were present as monatomic anions in the channels, the chemical formula would not charge-balance and ions would necessarily be forced closer to each other than would be considered reasonable based on the established ionic radius for I^- (2.06 Å).

Table 4: Elemental analysis summary of compounds 1 – 8 done using EDS. The ratios of halide ions to the transition metal ions were consistent with the proposed formulae.

Compound	X	M	Atomic % (found)					Ratio X /M (found)	Ratio X /M (expected)
			K	M	O	F	X		
1	$Cl_{1/3}$	V	0.216	0.108	0.080	0.599	0.0060	**0.056**	**0.056**
2	$Br_{4/2}$	V	0.177	0.089	0.116	0.593	0.0252	**0.283**	**0.333**
3	Cl	Mo	0.192	0.120	0.232	0.435	0.0206	**0.172**	**0.167**
4	Br	Nb	0.174	0.123	0.099	0.585	0.0185	**0.150**	**0.167**
5	$Br_{4/2}$	Nb	0.166	0.100	0.105	0.600	0.0295	**0.296**	**0.333**
6	$Br_{4/2}$	Mo	0.178	0.123	0.194	0.465	0.0408	**0.332**	**0.333**
7	$I_{4/2}$	Nb	0.148	0.096	0.094	0.634	0.0284	**0.296**	**0.333**
8	$I_{4/2}$	Mo	0.164	0.106	0.168	0.529	0.0322	**0.303**	**0.333**

The stoichiometric composition of these materials was checked by energy-dispersive X-ray spectroscopy (EDS) performed on single crystals. EDS was used because phase-pure materials could not be reliably obtained from synthesis, making more precise elemental analysis using inductively coupled plasma atomic emission spectroscopy (ICP-AES) unfeasible. EDS can be reliably used to check stoichiometric ratios of elements but is not precise enough to accurately analyze subtle variations in composition. The EDS analyses, shown in Table 4 and Figure 11, indicated that compounds 2, 5, 6, 7, and 8 contained ~2 halogen atoms per formula unit instead of 1.
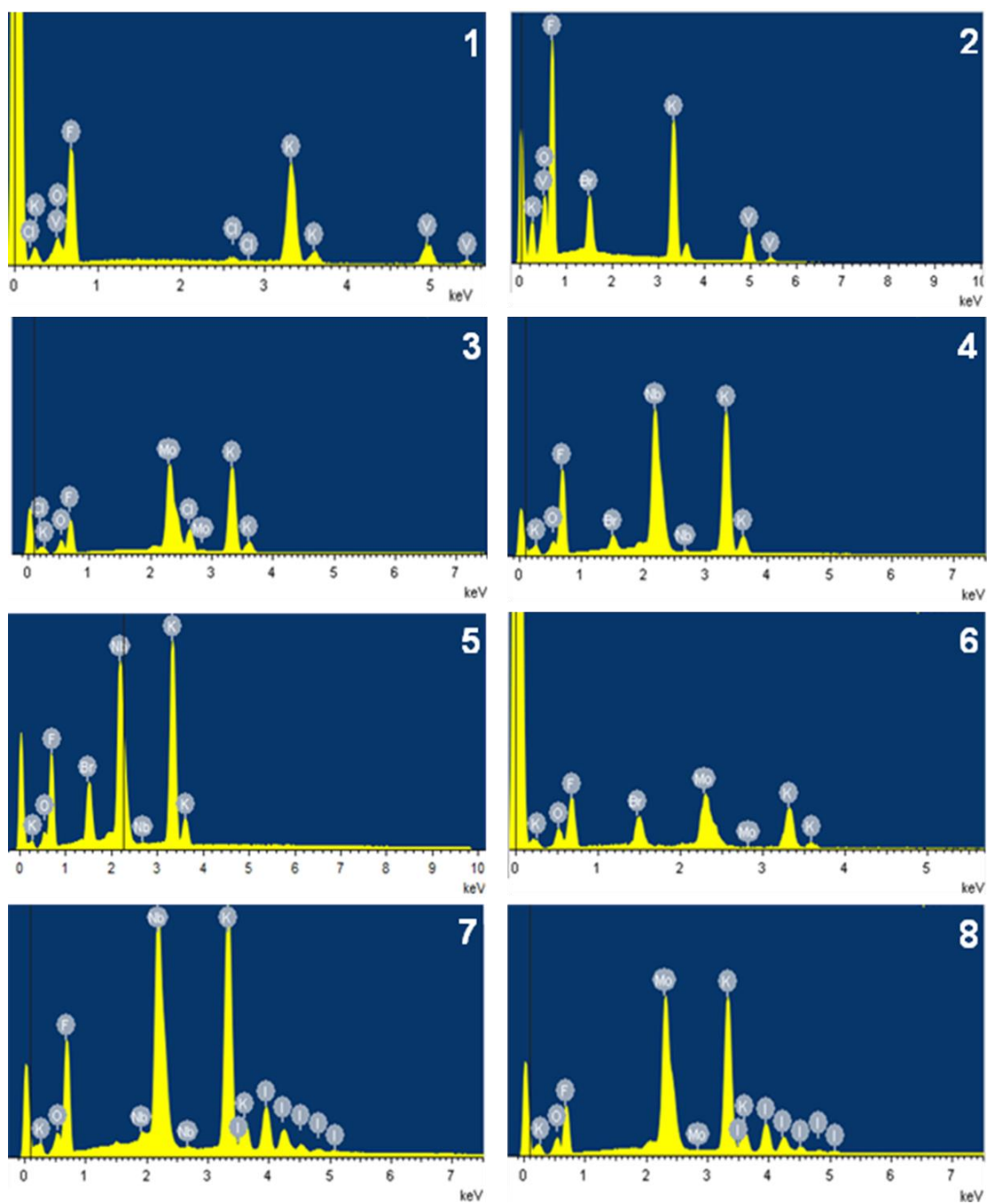
Figure 11: EDS spectra of single crystals of compounds 1 – 8.

To check the hypothesis that the compounds with extra halogen atoms had polyhalide ions in the channels, we performed resonance Raman spectroscopy to look for characteristic frequencies. Fundamental stretching band frequencies were observed that agreed with previous reports of trihalide detection. In addition, characteristic overtone progressions corresponding to triiodide and tribromide ions can be observed at integer multiples of their respective fundamental frequencies. An interesting feature appears at a lower frequency ($\sim$162 cm^{-1}) than the $[Br_3]^-$ fundamental in each of the tribromide containing compounds. We attributed this to an asymmetric stretching mode of the $[Br_3]^-$ that becomes Raman active through the distorting influence of forces within the crystal. The compounds that contain polyhalide ions are colored. Triiodide ions turn the crystals a grayish brown color while tribromide makes them red-orange. Crystals of these compounds form with a needle-like morphology. Some of the trihalide containing crystals were found to exhibit fading color intensity along the length of the crystals, and all of the trihalide crystals were found to slowly lose some of their color over several months when stored in air likely indicating changes in concentration of polyhalide ions.

Triiodide containing phases were observed to be dichroic, able to act as a linear polarizer of visible light. The alignment of the triiodide ions along the channels is analogous to the alignment of triiodide ions in crystals of the mineral herapathite.[126] In the original form of the commercial polarizing filter material Polaroid, needle like microcrystals of herapathite were aligned within a matrix of transparent nitrocellulose polymer film.[21] The large polarizability of the aligned trihalide ions decreases the transmittance for light polarized parallel to the alignment of trihalide ions in herapathite (as well as in the modern version of polaroid).[127] It is very likely

that the alignment of trihalide ions within our crystals gives them their observed dichroic property in the same manner.

3.2 Experimental

Aqueous hydrofluoric acid (49% by weight), potassium fluoride (>99.0%), and molybdenum (VI) oxide (99.5%) were used as received from Sigma-Aldrich. Niobium (V) oxide (99.9985%), vanadium (V) oxide (99.6%), and potassium bromide (99+%) were acquired from Alfa-Aesar. Potassium chloride (99.48%) was obtained from Malinckrodt. Deionized water was used in reagent quantities and as backfill in the pressure vessels. Pouches made of FEP were made in the manner described previously.[23,24,128]

3.2.1 Synthesis and Isolation of Single Crystals of $K_{10}(M_2O_nF_{11-n})_3X$

Caution! Hydrofluoric acid is toxic and corrosive! It must be handled with extreme caution and the appropriate protective gear and training.[129,130]

The dissolution of compounds in aqueous hydrofluoric acid can be exothermic and cause volatilization of hydrofluoric acid. Use of Teflon® at elevated temperatures allows $HF_{(aq)}$ to permeate the film; caution should be used in handling the backfill of these reactions.

Compounds of the $K_{10}(M_2O_nF_{11-n})_3X$ kind were synthesized by combining 10 mmol KX ($X^- = $ F,Cl,Br,I), 1 mmol $M_2^{5+}O_5$ ($M^V = $ V, Nb) or 2 mmol MoO_3, 24 mmol HF (0.87 mL of 48 wt.% $HF_{(aq)}$) and 0.63 mL of deionized water within a FEP pouch.

Pouches were placed, alone, within Teflon®-lined Parr acid digestion vessels which were then sealed and heated to 150ºC, held at this temperature for 24 hours, and then cooled to 25ºC at 0.1ºC/minute. The pouches were removed then opened and the crystals were separated from the pouch solution by filtering in air. The trihalide containing products are a 50:50 mixture of monohalide and trihalide ($[X]_{1/2}^-$ and $[X_3]_{1/2}^-$) and their content is noted as $([X][X_3])_{1/2}$.

Compounds with tribromide components ($[Br_3]^-$) were synthesized by the addition of 5 mmol KBr to the relevant syntheses for the compounds containing only the monobromide anions ($[Br]^-$). Synthesis of a vanadium compound containing triiodide ($[I_3]^-$) components was attempted, but resulted in the reduced vanadium compound K_3VF_6. The starting materials did not contain the trihalide species, which were generated in-situ via as-yet unidentified redox processes present under hydrothermal conditions. Mineral acids (such as HCl) are noted redox-active species. During the hydrothermal synthesis, redox reactions must take place in order to generate the $[X_3]^-$ from $3[X]^-$. Further investigation to uncover the responsible redox active species could potentially lead to useful applications for obtaining novel new compounds.

It is interesting to note that Compound 1 ($K_{10}(V_2O_2F_9)_3(F_2Cl)_{1/3}$) was initially synthesized without the use of any explicit source of chloride; KF, V_2O_5, $HF_{(aq)}$, and deionized water were used in the synthesis. The source of the chloride ions was found using EDS not to be the KF or V_2O_5 reagents, and may have been impurities in the aqueous hydrofluoric acid reagent. Compound 1 was subsequently synthesized with 10/3 mmol KCl and 20/3 mmol KF in place of 10 mmol KF.

3.2.2 Crystallographic Determinations

Single crystal XRD data was obtained at 100K with the use of a Bruker Kappa Apex 2 CCD diffractometer with monochromated Mo Kα radiation ($\lambda = 0.71073$ Å). The crystal-to-detector distance was 60 mm. The data were integrated with the program SAINT-V7.23A.[131] Absorption corrections (face-indexed) were applied. The structures were solved with XS by identification of the metal ions with direct methods of Fourier syntheses, and then refined with ShelXL to determine the anion sites, within the Olex2 suite.[132,133] Structures were checked with PLATON and no additional symmetry elements were found.[134] Crystallographic parameters are provided in Table 2 and Table 3. All structures were refined on a full-matrix least squares on F^2. Compound 6 exhibited commensurate super-symmetry (q vector = (0,1/3,0)); solution of the larger 1 x 3 x 1 cell was initially difficult with the use of ShelXL or SIR97 algorithms. The structure was solved with the ShelXT algorithm (unpublished).[135]

3.2.3 Elemental Analysis

Phase-pure materials could not be reliably obtained by synthesis. Impurities did not interfere with single crystal analysis, however they did prove to make elemental analysis via ICP-AES infeasible.
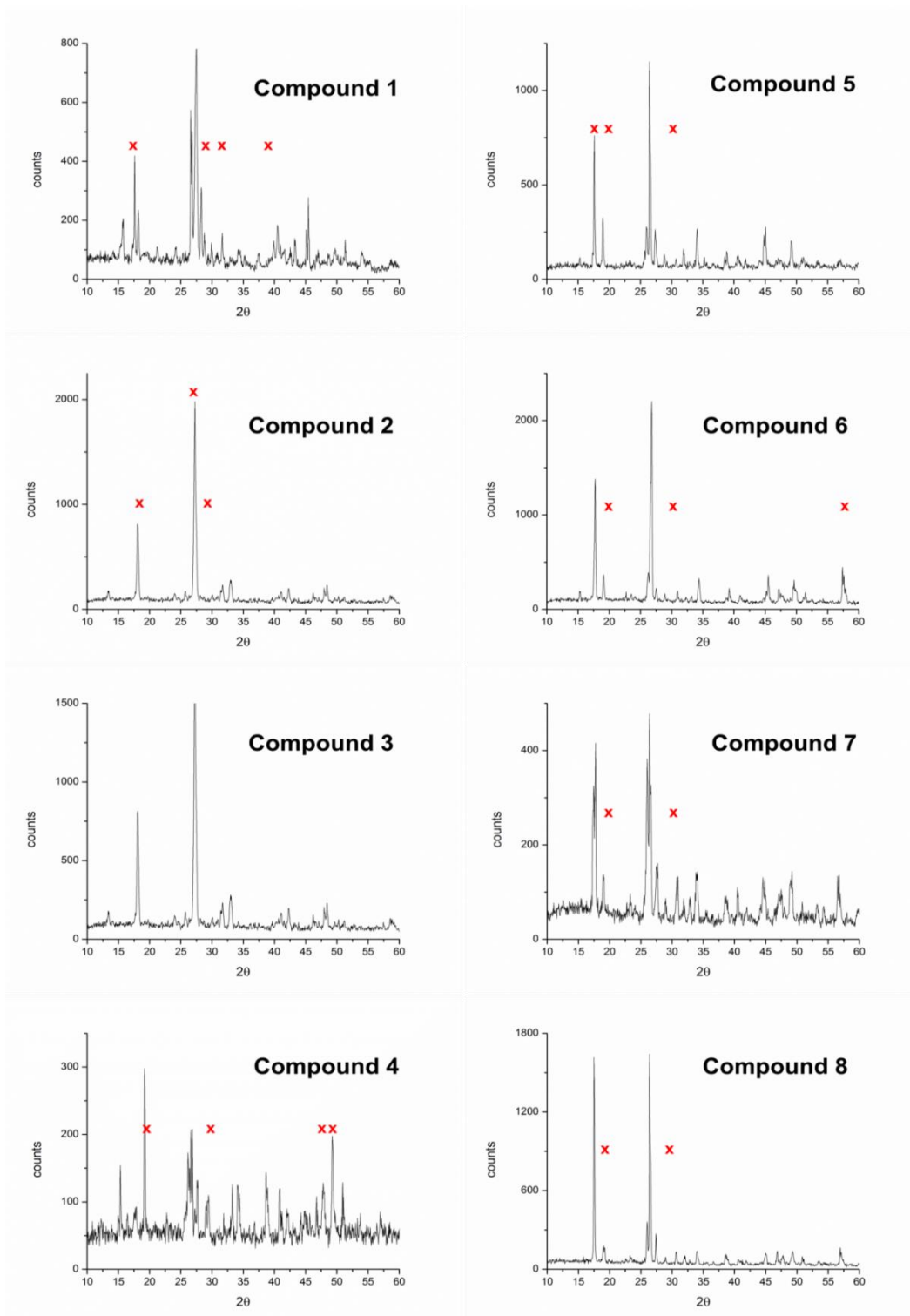
Figure 12: Powder X-ray diffraction patterns for compounds $1 - 8$. Red x's indicate peaks from secondary phases.

3.2.4 Powder X-ray Diffraction

The as-synthesized compounds were not phase-pure and qualitative analyses of the reaction products by PXRD were performed to determine the identities of secondary phases. Diffraction patterns were collected using laboratory radiation (Cu Kα – 1.5406 Å). The scans were performed over the range of $2\theta = 10 - 60°$ with a step length of 0.1 and an integration period of 1 second. The results are shown in Figure 12. Diffraction patterns were collected at room temperature with the use of a Rigaku XDS 2000 with Ni-filtered Cu Kα radiation (λ=1.5418 Å) and compared against patterns in the Joint Committee of Powder Diffraction Standards (JCPDS) database. The red "X" indicates a secondary phase. For compound 1, the impurity is Potassium Vanadium Oxide Fluoride ($K_2VF_3O_2$). For compound 2, the impurities are Vanadium Oxide Fluoride (VOF) and Potassium Bromide Fluoride ($KBrF_6$). For compound 3, the impurities are Molybdenum Oxide Fluoride ($MoOF_4$) and Potassium Molybdenum Oxide ($K_2Mo_3O_{10}$). For compound 4, the impurities are Potassium Niobium Fluoride (K_2NbF_7) and Niobium Oxide Fluoride (NbO_2F). For compound 5, the impurities are Potassium Niobium Fluoride ($K_2(NbF_7)$) and Potassium Niobium Oxide (KNb_3O_6). For compound 6, the impurities are Potassium Molybdenum Oxide (K_2MoO_4 and K_4MoO_5). For compound 7, the impurity is Potassium Niobium Fluoride (K_2NbF_7). For compound 8, the impurities are Potassium Molybdenum Oxide (KMo_5O_{13}) and Potassium Molybdenum Oxide Fluoride ($K(MoO_3)_3F$).

3.2.5 Resonance Raman Spectroscopy
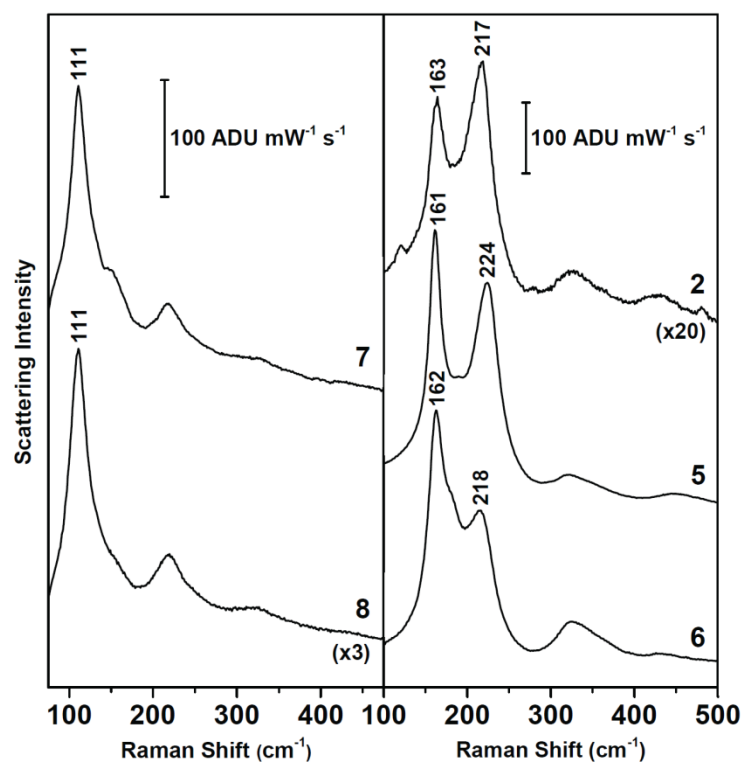
Figure 13: Resonance Raman spectra confirming the presence of $[I_3]^-$ in compounds 7 and 8 and $[Br_3]^-$ in compounds 2, 5, and 6. Spectra were acquired with $\lambda_{ex} = 532$ nm, $P_{ex} = 6.5$ mW, and $t_{aq} = 30$ s [3 accumulations (compounds 2, 7, and 8)] or with $t_{aq} = 5$ s [12 accumulations (compounds 5 and 6)].

The presence of triiodide ions in compounds **7** and **8** and tribromide ions in compounds **2**, **5**, and **6** was confirmed with resonance Raman spectroscopy Figure 13. Observed fundamental (symmetric stretch, v_1) band frequencies agree with previous reports of trihalide detection.[136-139] Additionally, the characteristic overtone progressions of triiodide ions and tribromide ions can be visualized in each spectrum at roughly integer multiples of their respective v_1 frequencies, consistent with previous Raman studies performed on resonance.[140] Interestingly, a prominent

feature to the red of the $[Br_3]^-$ fundamental is present in the spectra of each of the bromine-containing compounds. We attribute this peak to the $[Br_3^-]$ asymmetric stretch, v_2, which becomes Raman active as a result of distortion due to crystal forces.[141,142]

3.2.6 Computational Geometry Optimizations

Computational optimization was performed on the geometries of three configurations of the $[Nb_2O_2F_9]^{3-}$ anion. The purpose of these calculations was to understand the origin of the Λ-shape formed by this anion in the extended solid by analyzing a single unit; the Nb^V anion was chosen over the Mo^{VI} anion because the molybdate anion has 2 additional oxide anions that are disordered between the equatorial ligand sites for the two metal atoms. The three configurations used as starting conditions were (i) the Λ-shape configuration found in compound 3, (ii) a linear condition matching the geometry of the vanadate anion in compound 2, and (iii) the same linear coordinates of (ii) but with the central fluoride shifted perpendicular to the linear axis by 0.1Å. Optimizations were performed using the Q-Chem 4.1 computational suite with three pseudopotentials (CRENBL, LANL2DZ, SBKJC) and four different exchange correlation functionals (PBE0, TPSSH, M06, M11).[143] The optimized geometries of the anionic unit were found to be independent of the basis and functional used and also to be independent of the starting configuration. The optimized geometry was calculated in all cases to be linear with an Nb-F-Nb angle 180º. This result suggests that the coordination environment plays a significant role in generating the Λ-distortion.
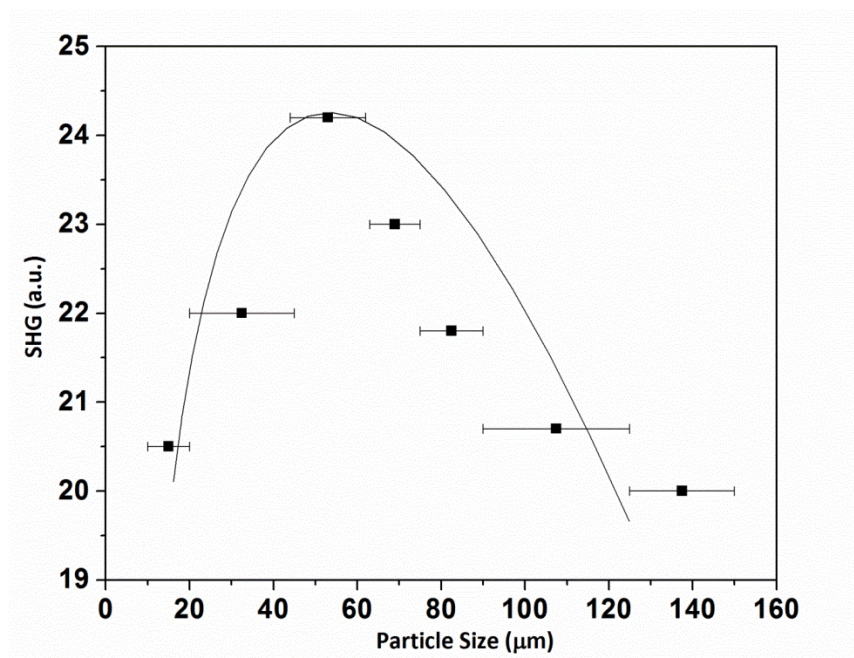
Figure 14: Second-harmonic generation response (arbitrary units) plotted versus particle size of a representative sample ($K_{10}(Mo_2O_4F_7)_3Cl$). The compound exhibits a response approximately 30 times that of α-SiO_2 and is type 1 nonphase-matchable. The line drawn is to guide the eye and is not a fit of the data.

3.2.7 SHG Measurements

Compounds 3-8 belong to a NCS space group (*Pmn*2_1), and their SHG responses were measured. Compounds 7 and 8 showed no signal, which we attribute to the dark color of the $[I_3]^-$ ions in these crystals. Compound 3 was selected for more detailed SHG measurements. The powder SHG response with 1064 nm radiation was found to be approximately 30x α-SiO_2 in the 45 – 63 μm particle size range. Measured SHG response as a function of particle size is plotted in Figure 14. The observed behavior indicates Type 1 non-phase-matchability and puts compound 3 in the class C category of SHG materials, as defined by Kurtz and Perry.[144]

3.3 Bond Valence Sum Calculations

Selected bond valence values are shown in Table 5 individual bond valence values were calculated using the equation given in chapter 2.

Table 5: The angles of the anionic units compared to the bond valence contributions from the transition metals, and the contributions from the coordinating K^+ ions.

Compound	Bridging Fluoride	M-F-M angle	BVS from Metals	BVS from K^+ ions
$K_{30}(V_2O_2F_9)_9F_2Cl$	F3	168.443(314)	0.722	0.255
	F6	180	0.782	0.265
$K_{10}(V_2O_2F_9)_3Br$	F5	180	0.667	0.284
	F8	180	0.726	0.302
$K_{10}(Nb_2O_2F_9)_3Br_2$	F9	160.991(87)	0.740	0.198
	F14	157.136(131)	0.705	0.248
$K_{10}(Nb_2O_2F_9)_3I_2$	F9	164.057(262)	0.755	0.162
	F14	160.296(302)	0.716	0.193
$K_{10}(Mo_2O_4F_7)_3Cl$	F9	168.259(209)	0.765	0.201
	F14	154.038(262)	0.740	0.207
$K_{10}(Mo_2O_4F_7)_3Br_2$	F2	160.633(291)	0.696	0.202
	F14	157.994(350)	0.673	0.246
$K_{10}(Mo_2O_4F_7)_3I_2$	F9	168.643(416)	0.773	0.217
	F14	163.977(664)	0.705	0.262

3.4 Conclusions

The series of compounds in the $K_{10}(M_2O_nF_{11-n})_3X$ family discussed here illustrate how the interplay between anionic building units and their coordination environment can cause polarizing, Λ-type distortions with consequences for the overall symmetry of the material. The second row transition metals Nb^V and Mo^{VI} were found to form anionic units that were more likely to stabilize with these polarizing distortions and produce compounds in the polar space group $Pmn2_1$. The first row transition metal V^V was found to form anions that are less likely to stabilize with a polarizing distortion and to produce compounds having one of the CS space groups $P3m1$ or $C2/m$. We found that the origin of the distortions could be well explained using the bond valence method as a response to an under-bonded bridging fluoride ligand in the anionic unit in accordance with the distortion theorem. The longer equatorial M-F bonds observed in the Nb^V and Mo^{VI} anions act as a limiting factor on the coordination of the bridging fluoride by nearby K^+ cations. This series of compounds serves as an example of how subtle the boundary between CS and NCS phases can be. Future investigations into other systems of pseudosymmetrical compounds with both CS and NCS phases could lend additional insights, and could help lead to a method for predicting the conditions necessary for polarizing distortions of this kind.

Chapter 4

4.1 Crystallographic Challenges

When using experimental data to build or evaluate a theoretical or computational model

of a material, it is important that the experimental data are as accurate and detailed as is

reasonably possible. The fundamental purpose of models is to reproduce, explain, and predict the

results of real experiments. By this metric, the precision of any model is necessarily limited by

the precision and accuracy of the experimental data involved in its development and evaluation.

Even *ab initio* computational models are almost always parameterized by using contraction

coefficients to modify simplified orbital functions. In molecular computational chemistry

parameterization is done by a selection of the basis set to be used or by adjusting contraction

coefficients to minimize the energy of a studied structure.[145] Different basis sets use different

approximation schemes and produce different results when applied to the same system. Basis

sets are selected in these cases based on a history of giving results that agree well with

experiment when used for molecules similar to the molecule to be modeled. In solid state crystal

systems, a basis-set optimization is usually necessary.[145] In other words the basis sets used for

modeling inorganic crystal systems need to be adjusted to minimize the energy of the structure

being modeled. When this is done the model becomes semi-empirical, and has its reliability

limited by the accuracy of the constraints on the structure for which the basis set is being

optimized.

The "accuracy" of a structure refers to how closely the experimentally determined structure resembles an arrangement of atoms in a static equilibrium condition. Several factors can cause an experimental structure to deviate from such a condition, including atomic site disorder, crystal twinning effects, site vacancies, lattice strains, and the effects of temperature. Thermal vibrations can have significant influence on experimental crystal structure and symmetry. Temperature is kinetic energy and at any finite temperature the atoms within a crystal vibrate. Consequently, experimental crystal structures are always representations of a time-averaged arrangement of atoms under dynamic conditions.

4.2 Averaging

As the complexity of crystal systems increase so do the numbers of different ways that the atoms can vibrate with temperature.[146] Experimentally determined atomic positions are averaged over time and distance, with resolution limited by the nature of the variations (whether locally ordered domains form). Time-resolved crystallographic techniques exist, but the application of these is limited to the study of stimulation-response phenomena such as photon driven transitions.[147] Experimental structures are averaged over space, because crystallographic diffraction methods depend on the properties of a repeating unit cell. Small variations in the atom positions between neighboring cells disappear into the average Figure 15. Assuming that a crystal has no defects, vacancies, or disordered sites, the difference between its experimental structure at finite temperature and the crystal structure that would be seen if the experiment could be performed at absolute zero is the limiting factor for the "accuracy" of the experimental structure.
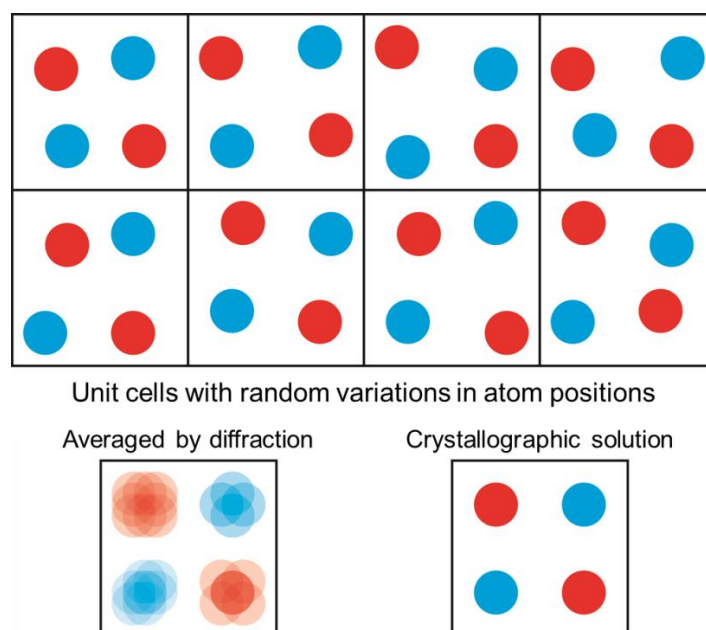
Figure 15: The process of diffraction averages atomic positions over both space and time. Averaging over time causes vibrational motion to be observed as blurring, while averaging over space causes variations in equilibrium positions to be observed as splitting.(Top) 8 unit cells in a crystal with variations in the specific atom positions. (Bottom Left) the depiction of the unit cell that would fit the diffraction pattern from the crystal section shown above best, and includes many sites of partial occupancy. (Bottom Right) The crystallographic solution of the diffraction pattern without sites of partial occupancy, this structure solution misses the variations in atom positions entirely.
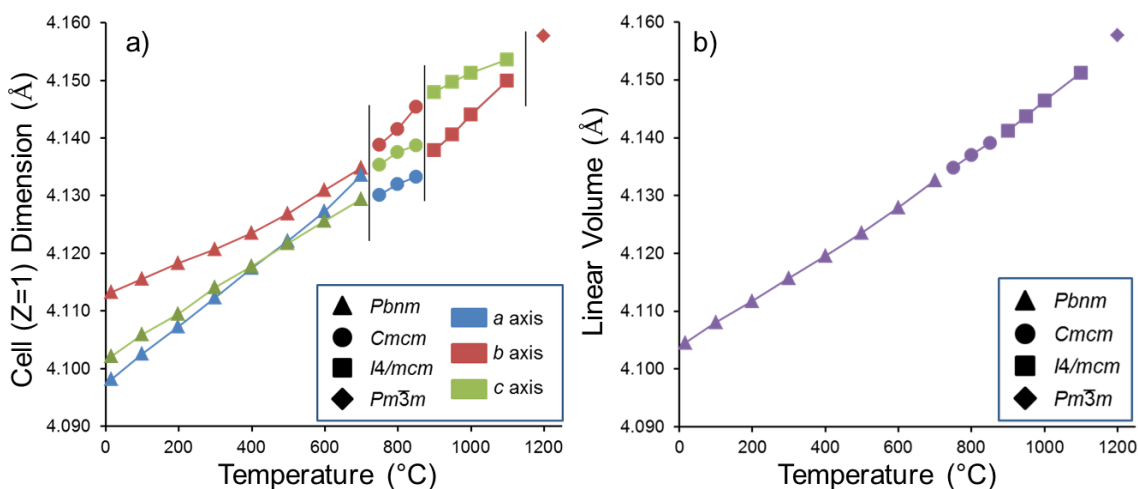
Figure 16: An example of thermal expansion behavior of the lattice parameters of an inorganic solid using the perovskite $SrZrO_3$. The changes in lattice parameters are continuous with temperature for each of the observed phases, with discontinuities occurring only at the phase transition boundaries. No discontinuous changes in lattice parameters or unit cell volumes are ever expected except when coupled to a phase transition. Figures adapted from reference [148].

4.3 Thermal Expansion

It is well understood that material densities are, in part, functions of temperature. For most crystalline solids, increasing the temperature produces in an increase (or decrease) in volume and, in-between discontinuous phase transitions, these temperature-volume relationships follow smooth, continuous curves Figure 16.[148] The same is usually true for the relationships between temperature and individual lattice parameters. Based on these trends it is natural to expect the same behavior from atom positions, to expect that a series of experimental crystal structures, collected for a single phase of a compound under varying temperature conditions, would show that changes in atom positions and bond lengths also exhibit smooth, continuous changes with temperature. This, fascinatingly, seems to not always be the case.

4.4 Bond Distance Nonlinearity

In crystals most thermal energy takes the form of phonon modes, specific resonant vibrations that propagate through the lattice.[146,149] Every real crystal has many individual phonon modes that are populated unevenly in distributions that change with temperature.[150] The interplay of phonon modes in a crystal directly impacts time-averaged (and therefore also the experimentally observed) bond lengths and atomic positions. Consequently, it is reasonable to say that as the temperature of a crystal phase changes only those limitations imposed on atom site positions by the symmetry of the crystal can be reliably expected to hold true. It is important to note that the effect being described is distinct from the concept of the crystallographic thermal parameters, which describe the shape of the probability distribution of an atom in space around its symmetry site and are often represented visually as thermal ellipsoids.[151] The effect discussed here involves nonlinear changes the atomic site coordinates themselves so that the equilibrium positions are different at different temperatures and pressures. In other words, this effect moves the center point of the thermal ellipsoids rather than simply changing their shape. Changes in pressure can also produce nonlinear variations in atom positions, as was shown explicitly by Keller, Holzapfel, and Schulz in their work on elemental crystals of Se and Te.[152]
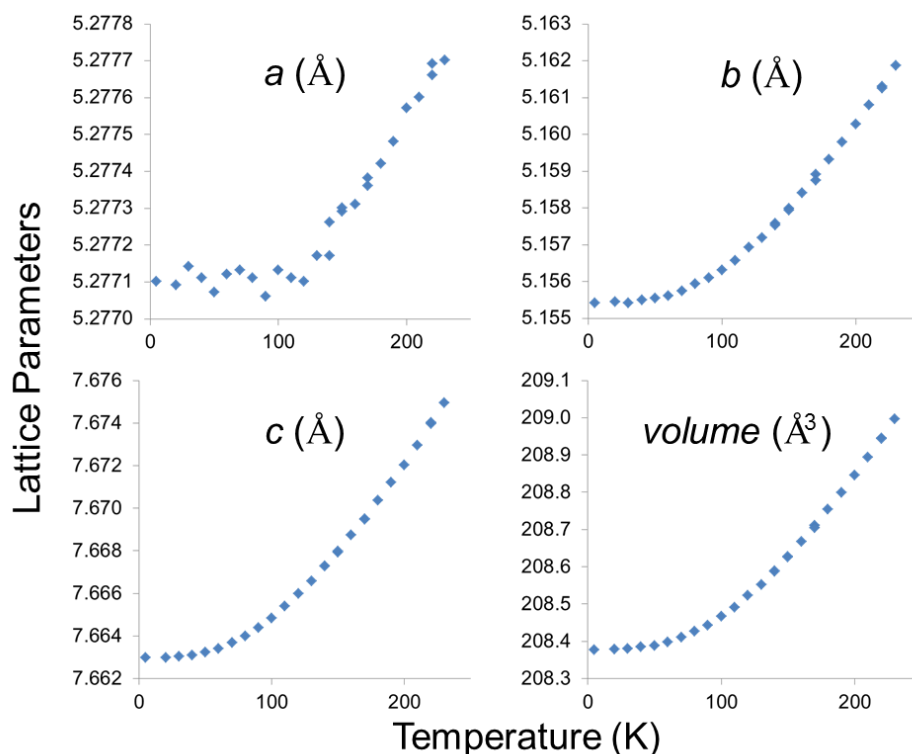
Figure 17: Continuous behavior of the lattice parameters of ε-WO$_3$ from 5K to 250K observed by powder neutron diffraction. The apparent noise in the behavior of the a-axis is due to the very small total change in this parameter and the limits of the experimental precision. Note that the c-axis changes the most over the temperature range (~0.012Å). Adapted from reference [153].

4.4.1 ε-WO$_3$

An example system that illustrates the significant nonlinear impact that changing temperature can have on the observed atom positions in a crystal structure comes from an impressively detailed neutron powder diffraction study by Salje *et al* on monoclinic ε-WO$_3$.[153] In this study 30 experimental crystal structure solutions were obtained for temperatures ranging from 5K to 250K. Changes in the lattice parameters and cell volume were found to follow smooth trends as shown in Figure 17. In the crystal structure of ε-WO$_3$ there are two unique W^{6+}

sites, both sites have 6-fold oxygen coordination with octahedral geometry, and both exhibit out-of-center distortions. Figure 18 plots the reported values of the shortest W-O bond length for each site as a function of temperature, while Figure 19 plots the averaged W-O bond lengths for each site as a function of temperature. It is clear that, for this system, the observed bond lengths change discontinuously with temperature while the volume and lattice parameters change continuously.
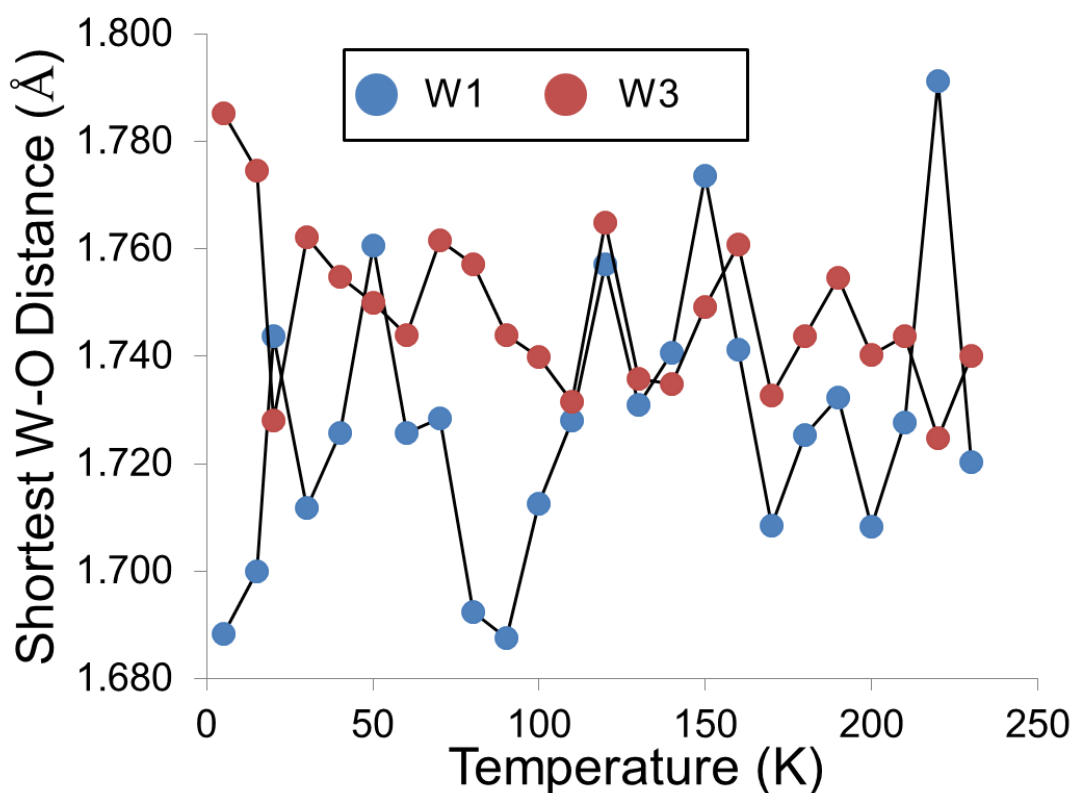
Figure 18: Highly discontinuous behavior of the shortest W-O bond lengths in ε-WO$_3$. The variation is plotted for both of the W sites in ε-WO$_3$. Values taken from crystal structures reported in reference [153].
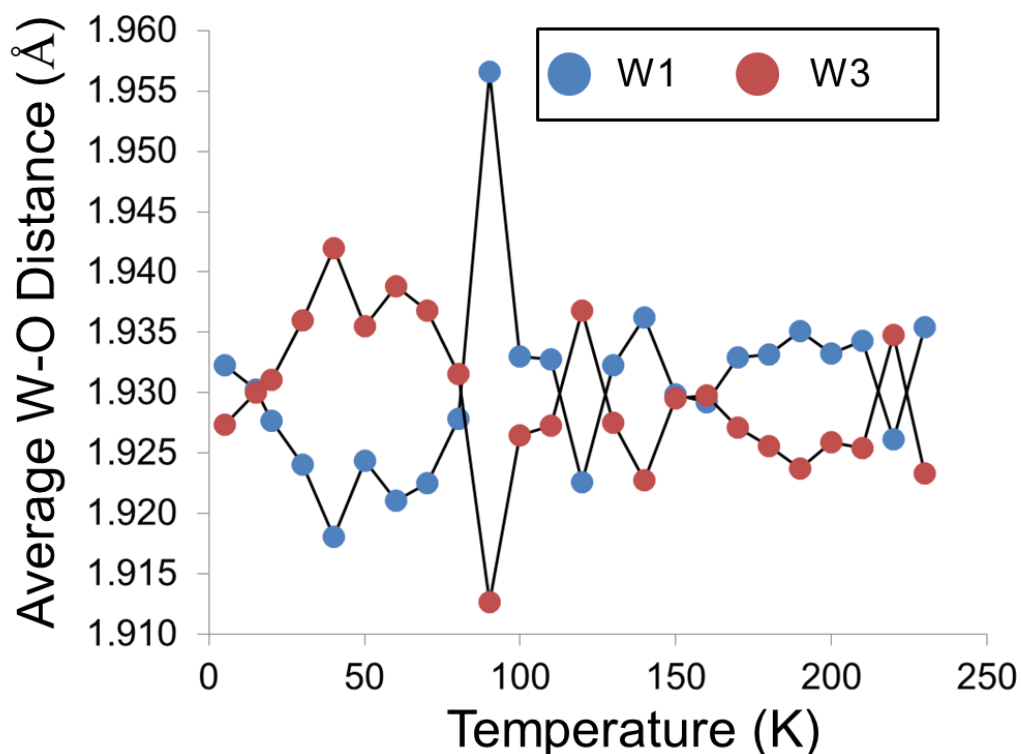
Figure 19: Variation in the average of the 6 W-O bonds for both W sites in ε-WO_3. Even averaged bond lengths show a significant nonlinear relationship with temperature. Values taken from crystal structures reported in reference [153].

4.4.2 β-YbV_4O_8

A single crystal X-ray diffraction study of an isosymmetric phase transition in β-YbV_4O_8 by Friese *et al* also exhibits a complex relationship between the temperature of the system and individual bond lengths.[154] A significant shift in bond lengths is observed at the temperature (~175 K) of the isosymmetric phase transition, but in the temperature regimes below and above the transition the experimentally reported V-O bond lengths change in ways that do not mimic the net lattice changes (Figure 20 and Figure 21).
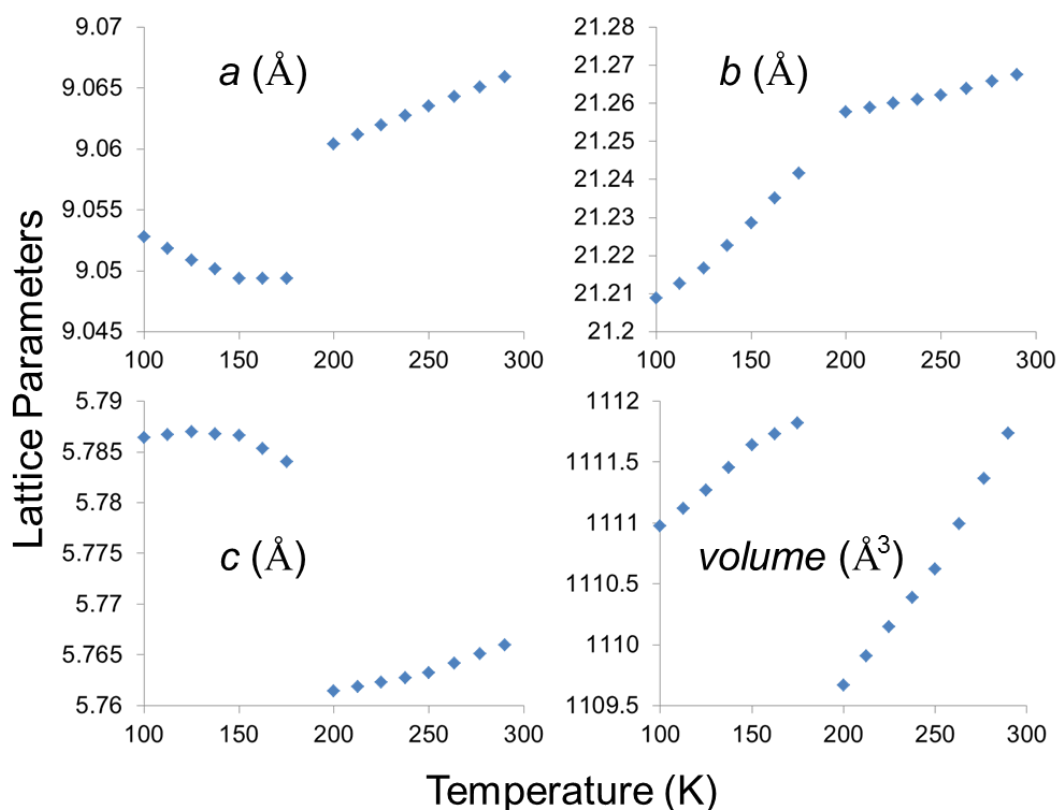
Figure 20: Continuous behavior of the two isosymmetric phases of β-YbV$_4$O$_8$ with temperature, with a discontinuity at the phase boundary (~175K). Adapted from reference [154].

Irregularity in the manner that individual experimental bond lengths change with temperature may be linked to phonon mode population distributions in the crystal changing with temperature. As phonon modes become populated in different ratios, the time-averaged atomic positions change. The reported behaviors of the ε-WO$_3$ and β-YbV$_4$O$_8$ systems suggest that for crystals with low enough symmetry experimentally observed atomic positions can vary significantly with small changes of temperature. Consequently, while crystal structures at every temperature point correspond to the thermodynamic equilibrium conditions they are not necessarily translatable to crystal structures in static equilibrium.
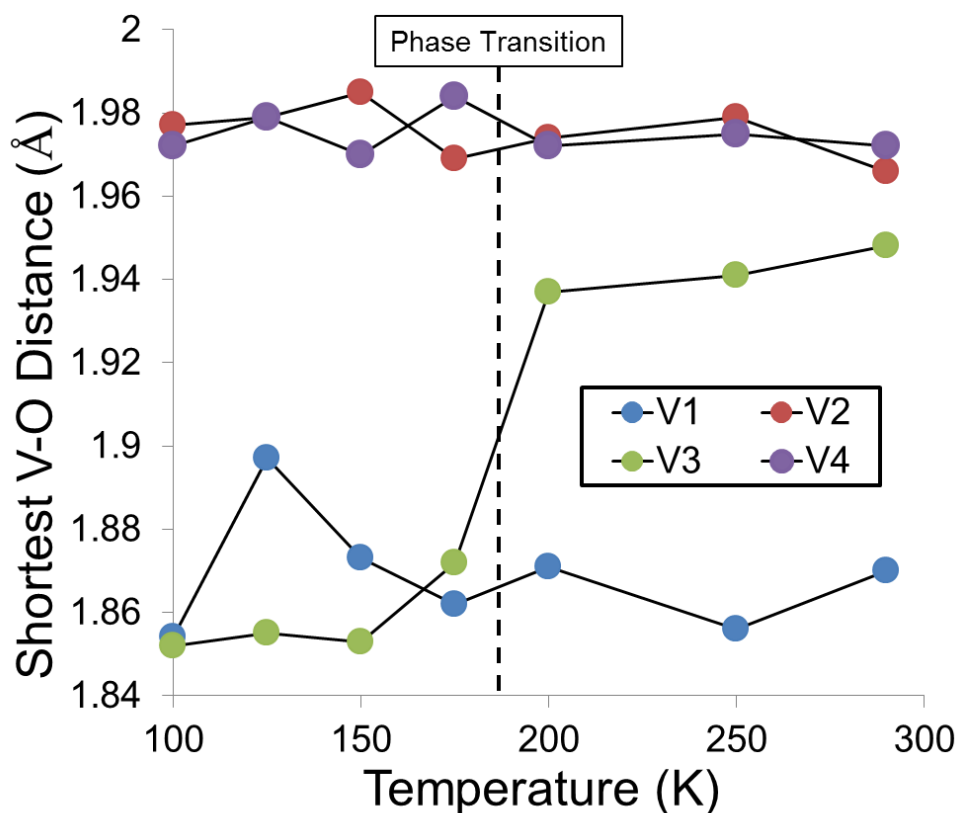
Figure 21: Discontinuous behavior of the experimental shortest V-O bond lengths for the four V sites in β-YbV$_4$O$_8$. Values taken from published single crystal x-ray diffraction structures in reference [154].

4.5 Consequences

Analysis of the experimental evidence discussed above indicates that small temperature variations can alter observed atomic positions by unexpectedly large amounts without breaking the crystal symmetry. Additional evidence and demonstrations of reproducibility will be necessary to prove (or disprove) this behavior. If it is real and reproducible, this effect may have significant implications for the future of computational inorganic chemistry. Improving the practical usefulness of theoretical models for predicting crystal structures requires comparing

them to experimental structures. If the experimental structure information is distorted by the influence of temperature effects and those effects are not accurately accounted for by the theory, inaccurate conclusions about the models will result. For empirical models, which are more directly based on experimental data, the impact of nonlinear relationships between measured atomic positions and temperature is far more critical. Structure-based empirical models are parameterized to minimize net forces. It is very likely that two empirical models based on two of the reported ε-WO$_3$ structures collected only 10K apart would predict behavior different from each other, and that neither model would predict the atom positions of the other. The scale of the average fluctuation in the reported shortest W-O bond lengths in ε-WO$_3$ represent changes to the coulombic component of the pair interaction energy in amounts on the order of 1eV (~96 kJ/mol) for a change in temperature of only 10K, an enormous level of uncertainty. To put that variation in perspective, the total lattice energy of NaCl is ~8eV/formula unit.[155] When fitting empirical models for simulation purposes, thermal variations between experimental and minimum potential energy structures cause the temperature and pressure ranges where the simulations are accurate to shrink.

4.6 Strategy for Improving Experimental Data Sets

By collecting crystal structures at very low temperatures, uncertainty about the relationship between experimental results and the static equilibrium structures can be minimized. While the impact of temperature on crystal structure causes uncertainty, varying the pressure on a crystal changes the static equilibrium structure. This can be useful when constructing empirical models, because it allows collection of multiple crystal structures on the same sample, representing static equilibria at a different pressure conditions. By exploiting the influence of

pressure and minimizing the influence of temperature, a large amount of high quality

experimental data can be collected, ideally suited to the development of robust empirical models.
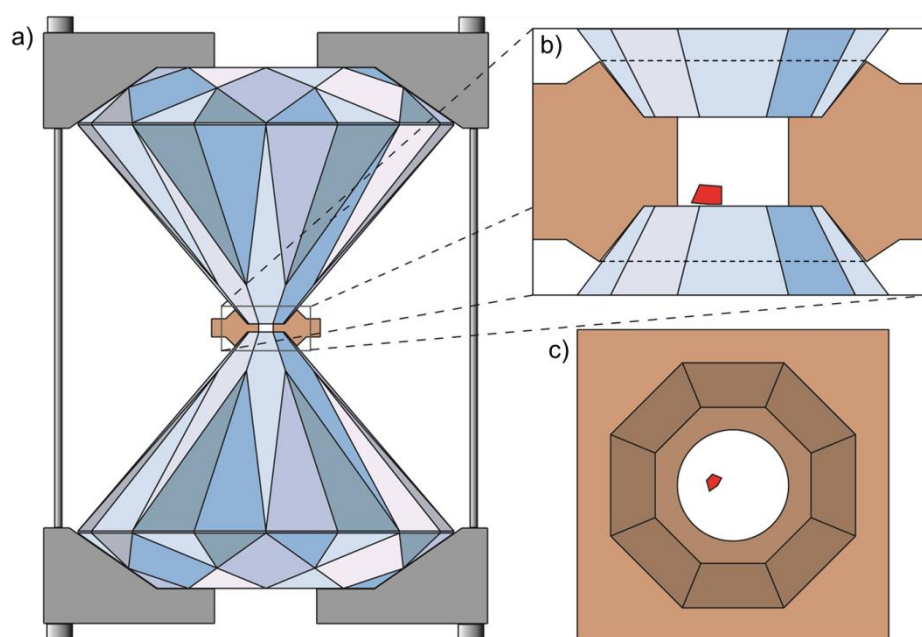
Figure 22: Diamond Anvil Cell. a) Side view showing two flattened-tip brilliant-cut diamonds

mounted in a frame used to apply and adjust the pressure, with a metal gasket sandwiched

between the tips. b) Close up side view of metal gasket (cutaway) showing the sample (red)

inside a hole drilled through the gasket. c) Top down view of metal gasket and sample with

diamonds omitted, the octahedral indentations from the diamond in the metal gasket can be seen.

(Features are not shown to scale).

Probably the most useful tool for experimental investigation of high pressure systems is

the diamond anvil cell (DAC).[156] DACs allow a variety of experiments to be performed under a

broad range of pressure conditions, from x-ray methods to IR spectroscopy to ultrasonic

vibrational measurements. A DAC houses samples in a chamber made by drilling a hole in a metal gasket which is then sandwiched between the flattened tips of two brilliant cut diamonds (Figure 22). By bringing the diamond surfaces closer together the metal gasket is made to deform and the volume of the sample chamber shrinks increasing pressure on the sample.

High pressure crystallography has its own set of special challenges.[157] One of these is limitations on the diffraction geometry resulting from the shape of physical DAC apparatus, limitations that become more significant as pressure is increased the lattice dimensions of the sample shrink causing 2θ values to increase. Contributions to the collected diffraction patterns from the pressure medium, the metal gasket, and the diamonds complicate the data analysis procedure. When doing variable pressure studies over a finite period of time, there is also a tradeoff between the number of pressure conditions being measured and the quality of the data collection for each point.

This concept of using low-temperature and variable pressure crystal structures to develop empirical models with improved predictive capabilities was important for the research that will be discussed in detail in [CHAPTER]. Cryogenic (~15K) DAC single diffraction studies on the behavior of the crystal structure of $KNaNbOF_5$ in response to varying pressure were used as the basis for the development of an empirical model of the ionic system.[CITE] Molecular dynamics simulations performed using this model were able to successfully reproduce and provide a structural explanation for previously unsolved in situ powder diffraction patterns of a temperature induced reconstructive phase transition. The importance of this success, for the discussion here, is that the empirical-type model was predictive at very different pressure/temperature conditions than those of the experiments on which the model was based,

and that it was also predictive for the system in 3 different crystal phases when it was fit only to one of them, indicating transferability.

Early computational modeling efforts focused primarily on the behavior of systems exhibiting high symmetry phases having atomic coordinates fully constrained by their Wyckoff site symmetries and involving no internal degrees of freedom.[158] These symmetry conditions eliminate any possibility of nonlinear effects of temperature or pressure on atom positions. For such high-symmetry phases the fractional atomic coordinates cannot change independently when lattice dimensions change in response to changing pressure and temperature conditions. Lower symmetry phases permit significant impact from changes in temperature or pressure on the observed structure of a crystal without actually changing the symmetry of the crystal. This effect takes the form of nonlinear changes to relative atomic positions in experiments where the structure is observed at a series of small temperature intervals. Changing pressure conditions have been reported to result in a similar type of nonlinear effect on relative atomic positions.[152] The observation of this kind of behavior is reasonable given that the relationships between bond lengths and bond energies are both complicated and different for different bond types. These effects are usually either overlooked, or assumed to be small enough to ignore.

4.7 Conclusions

A major implication of these observed temperature/pressure effects is that relative atomic positions for a low symmetry crystal structure at 0K cannot be reliably predicted by taking the atomic positions from the experimental structure at some significantly higher temperature, and mapping them onto the thermal expansion behavior of the lattice dimensions. In other words, in order to reliably determine the relative coordinates of the atoms in a low symmetry crystal

structure at some temperature it is necessary to actually measure the single crystal structure at that temperature.

Empirical and semi-empirical methods are still necessary for computational modeling of complex structures.[105] One of the primary shortcomings to using empirical atomistic models is that they tend to only be predictive within a small window of physical conditions.[105,116,117] By taking into account the effects described in this chapter the window of conditions for which an empirical model of a complex crystal system can be expected to be predictive can be expanded significantly. An empirical model fit to crystal structures collected at very low temperatures can reproduce the real behavior of the system much more reliably than one fit using a series of room temperature crystal structures.

Chapter 5

5.1 Solid-Solid Phase Transitions

A solid-solid phase transition is when the atomic structure of a material changes from one ordered crystalline state to a different ordered crystalline state in response to changing temperature, pressure, or electromagnetic fields.

A displacive phase transition is a transition that can be described by small shifts in observed atomic positions with no breaking of bonds. Solid-solid phase transitions usually involve a change of crystal symmetry (though not always), and group/subgroup relationships always link the initial and final phases of a displacive transition. These transitions may be first order (discontinuous) or second order (continuous). This makes it possible to apply group theoretical descriptions to completely describe the symmetry changes involved in displacive phase transitions. Displacive phase transitions are observed in several heavily studied ferroelectric materials. Transitions associated with octahedral tilting in perovskites are also displacive.

A well-studied example of a displacive solid-solid phase transition is the temperature induced transition from the α- to β-phase of quartz.[159] The transition to β-phase is characterized by the loss of a tilting angle between the corner-linked SiO_4 tetrahedral units. Some compounds, such as the ferroelectric perovskite $KNbO_3$ undergo several sequential displacive phase transitions with changing temperature.[160-162] In all but one of the phases of $KNbO_3$ the B-site cation, Nb^{5+}, exhibits an out-of-center distortion within its octahedral coordination polyhedron. In the lowest temperature phase this distortion is directed toward a face. As the temperature is

increased the distortion shifts to edge directed, then corner directed, and finally the distortion

disappears (Figure 23).

5.2 Disorder in Crystals

There are two general kinds of disorder that parts of crystal systems can have, static

disorder and dynamic disorder, Figure 24 gives a brief visual description of the two. Dynamic

disorder results from continuously active local rearrangements of atom sites in the individual unit

cells while in statically disordered systems individual unit cells maintain their atomic

arrangements over time, but differ in some way from nearby unit cells. Dynamic disorder often

presents experimentally as static order with enlarged thermal parameters.[163] The progression of

phase transitions in $KNbO_3$ can be described as a series of displacive transitions, but it can also

be understood as a series of dynamic-type order-disorder phase transitions.[164]
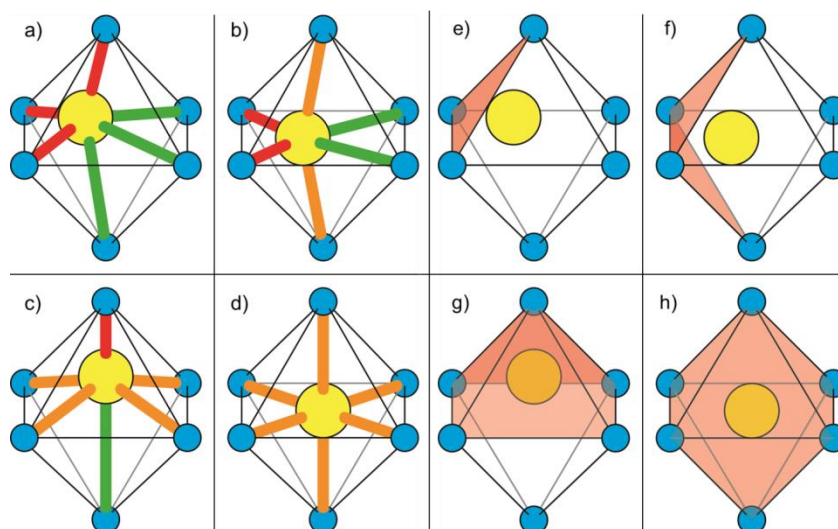
Figure 23: The NbO_6 octahedron is different for each of the four phases of $KNbO_3$.

Experimentally, the central Nb atom (yellow) undergoes displacive transitions from a face-

directed distortion (a, R3m), to an edge-directed distortion (b, Amm2), to a corner-directed

distortion (c, P4mm), to an undistorted phase (d, Pm3-m). The O atoms (blue) are displaced little throughout the transitions, and the displacive explanation suggests that the minimum energy Nb position within its octahedral coordination environment goes through 4 non-equivalent positions. The system is more reasonably explained as a series of order-disorder transitions. This explanation gives the Nb atom 8 equivalent energetic minima, distortions toward each of the faces of the octahedron. Electrostatic interactions between nearby NbO_6 octahedra give a preferred direction for the positions occupied (shaded faces). The low temperature phase is ordered with all Nb atoms distorted in the same direction toward a face (e, *R3*m), heating results in dynamic disorder between 2 adjacent faces and appears edge directed (f, *Amm*2), the next phase is disordered between 4 faces and seems corner directed (g, *P4mm*), and finally when the Nb is disordered between all 8 faces, there is no apparent distortion (g, *Pm3-m*).

5.2.1 Experimental Character of Disorder

The Nb atom in an isolated $[NbO_6]$ octahedron has 8 minimum energy positions corresponding to displacement from the center toward each of the 8 faces of the octahedron. In $KNbO_3$ the face distorted position occupied by the Nb atom results in a local dipole moment and influences the position occupied by neighboring Nb atoms, so that the lowest temperature structure is ordered with all Nb atoms distorted in the same direction. As the temperature of the system is increased, an order/disorder transition distributes the Nb between a pair of adjacent octahedral faces, so that it oscillates about a point between the faces, and appears to be distorted toward the shared edge. Increasing the temperature further leads to another order/disorder transition that distributes the Nb atom between four of the faces of the octahedron, making it appear to distort toward the corner the four faces share. The dipole moment is still present and

the system maintains ferroelectric properties. The final order/disorder transition distributes the

Nb atom between all 8 minimum potential energy positions, eliminating the conserved

component of the dipole moment and making the Nb atom appear to occupy the center of the

octahedron.
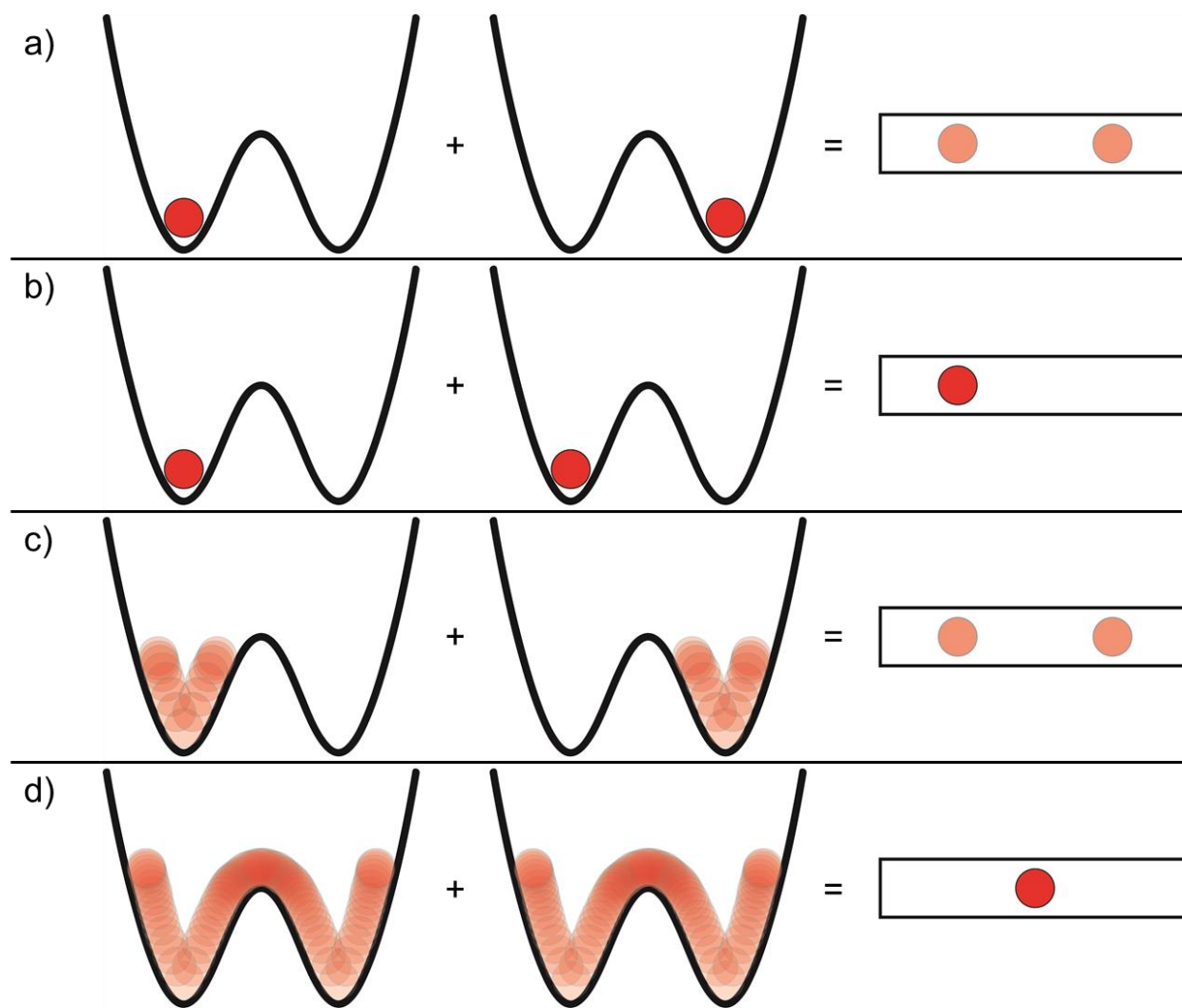
Figure 24: Static vs dynamic disorder, a one dimensional crystal with atoms in double well

potential environments (2 cells shown) can exhibit 3 different ordering conditions. (a) If the

system is static and there is no preference for either potential well the atom will appear to be split

between two sites. (b) If the system is static and one of the potential wells is preferred the system is, and will appear, ordered. (c) If the system has vibrational energy (heat), no preferred well, and the energy to switch between wells is larger than the vibrational energy, the system will appear disordered between two sites. (d) If the system has vibrational energy, no preferred well, and the energy to switch between wells is smaller than the vibrational energy, the system will appear ordered at a point halfway between the two sites. Conditions (a) and (c) are statically disordered states, condition (b) is ordered, and condition (d) is a dynamically disordered state. Dynamically disordered atoms are observed at positions that are different from the lowest energy positions for those atoms.

5.2.2 Resolution Dependence

The term "disorder" describes a state in which multiple arrangements of the same system are indistinguishable from each other. As this definition implies, disorder is a resolution dependent condition, with practical limits imposed by the ability of an experiment to resolve differences in space and time, and with fundamental limits on individual particles imposed by the uncertainty principle.[165] Any description of disorder (or order) in a measured system is limited by the experimental resolution, though it is rarely made explicit. Disorder in crystal systems comes in several forms, and transitions between ordered and disordered states can be of first or second order.[166,167] Magnetic phase transitions are order/disorder transitions that do not, in general, involve significant structural components, as they are governed by the spin orientations of unpaired electrons and these only weakly impact the motions of atomic nuclei.

5.2.3 Mixed Occupancy

One type of crystallographic disorder, often encountered in oxide-fluoride compounds, is the existence of a shared atomic site. This kind of disorder is the occupation of a single crystallographic site within the unit cells by more than one kind of atom. In oxide-fluoride compounds the strong similarity between the oxide and fluoride anions (in terms of ionic size and bonding distances) frequently leads to this kind of disorder. Historically, characterizations of oxide-fluoride crystal structures have been made without any attempt to tell oxygen and fluorine sites apart, because the experimental resolution was simply not adequate to do so reliably.[168,169] This has likely resulted in reported crystal structures with more disorder or higher symmetry than would be found using more modern instruments. It is possible to resolve the difference between oxygen and fluorine sites using modern diffraction technology, however it is still usually considered necessary to provide some additional evidence, such as an argument based on bond valence sums, to support the elemental assignments. For many compounds higher resolution diffraction experiments cannot resolve atom site disorders because they simply do not have any long range order. A transition from an ordered condition to one with atom-site disorder involves switching atoms between sites and often requires a significant amount of energy.

5.2.4 Split Occupancy

Crystal disorder can also occur when an individual atom has two (or more) stable equilibrium sites with a distribution of occupation between them, this is called split occupancy. Atom site disorder and split occupancy are both kinds of static disorder. Experimental crystallography cannot differentiate between individual unit cells in a sample because of the statistical nature of crystallographic methods. If the energetic barrier between the sites the atom

can occupy is low enough that thermal vibrations can easily overcome it, split occupancy

disorder becomes dynamic disorder (Figure 24). In non-stoichiometric crystals, a random

distribution of vacancies produces crystallographic sites of partial occupancy, another kind of

crystallographic disorder closely related to split occupancy.

An important difference between static and dynamic disorder is the impact on the

observed atomic positions. Atoms that are statically disordered between two identical energetic

minima appear to be at both minimum energy positions with site occupancies of ½ for each

position. Atoms that are dynamically disordered across two local energetic minima appear

primarily to occupy the midpoint between the two sites. A dynamically disordered atom switches

back and forth between minimum energy sites and, as it crosses over between the sites, it

expends kinetic energy and slows down. Consequently, spends most of its time in the region of

maximum potential energy and minimum energy gradient, which is the top of the transition

barrier. So, as described for the $KNbO_3$ system above, displacive transitions and order-dynamic

disorder transitions can often be the same thing.

5.3 Reconstructive Transitions

Among solid-solid phase transitions the most enigmatic and intriguing category is

possibly that of the reconstructive transitions. These transitions do not exhibit the well-defined

symmetry relationships that govern displacive and order-disorder transitions. Reconstructive

phase transitions convert crystals between structures that do not share a group-subgroup

relationship, meaning that neither phase contains all of the symmetry operations of the

other.[170] Reconstructive transitions are drastic, involving the breaking and forming of bonds, and

they often result in fracturing of single crystal samples due to the stresses exerted on the lattice.

Reconstructive transitions have historically been referred to as the "uninteresting" case, for theoretical investigation because their lack of symmetry relationships.[171] The absence of direct symmetry relationships between the phases linked by a reconstructive transition makes it much more difficult to reliably deduce a kinetic transition pathway. Displacive and order/disorder transitions can be described well by Landau theory, but the lack of group/subgroup relationships leaves the symmetry of the super groups for reconstructive transitions ambiguous.[170] Additionally, activation energy barriers are typically very high for reconstructive transitions and their critical temperature/pressure conditions are often extreme, complicating experimental investigations.

5.4 Investigating Reconstructive Transitions

The analytical ambiguity of reconstructive transitions, the reason they were considered "uninteresting" in the past, is the very reason they are such interesting subjects for research today. With modern computational resources it is possible to address the behaviors of such systems using molecular dynamics and Monte Carlo methods, without relying on symmetry operations.[172-175] Reconstructive transitions can provide new insights into crystallization processes and the nature of interatomic interactions. By examining the mechanisms of reconstructive transitions, and the symmetries of the phases involved, we will be able to develop new rules for predicting the formation of crystal phases.
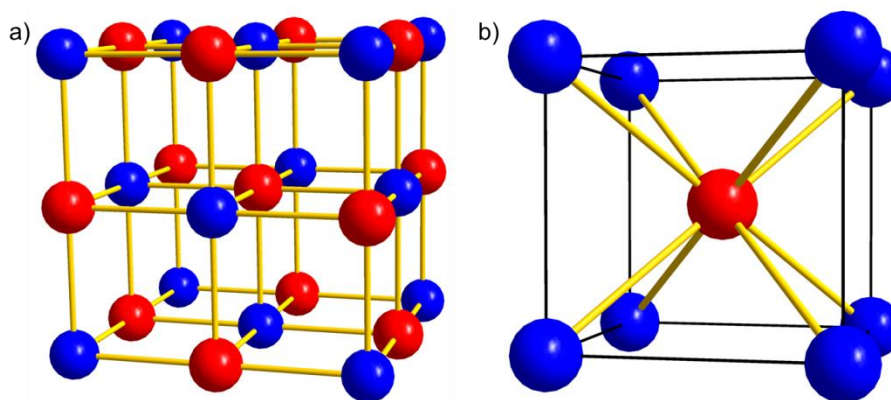
Figure 25: (a) NaCl-type or B1 alkali halide structure (space group Fm3-m), each atom has 6 nearest neighbors. (b) CsCl-type or B2 alkali halide structure (space group Pm3-m), each atom has 8 nearest neighbors.

5.4.1 B1 to B2 Transitions

Reconstructive phase transitions have most often been described and studied in compositionally simple compounds (materials made of 3 or fewer elements).[176-179] An example of one of these is the pressure-induced phase transition that occurs in most of the binary alkali halide salts, and involves a transition from the 6 nearest-neighbor NaCl-type structure to the 8 nearest-neighbor CsCl-type structure (Figure 25). In most of the literature on this transition the two phases are referred to, using the Strukturbericht notation, as the B1 and B2 phases, respectively. This reconstructive phase transition occurs primarily in response to an increase in pressure, and is experimentally reversible (with significant hysteresis). The B1 to B2 transition in the alkali halide salts is often used as a test case for various kinds of computational models by checking the ability of the model to identify the ground state phases and transition pressures for these binary salts. A detailed 2008 study by Čančarević *et al* compared several ab initio models this way, including Hartree-Fock and Density Functional Theory (DFT) using six different

functionals, and found significant variation in the predicted ground state phases.[180] None of the evaluated methods accurately predicted even the observed ground state phase for all 20 alkali halide salts that were modeled, although one method (DFT using LDA-VBH functional) predicted the correct phase for all but one. For the B1 to B2 transition itself, several kinetic pathways have been proposed and investigated and first principles calculations of the various mechanisms have had difficulty identifying a most likely mechanism.[181] By employing molecular dynamics simulations, the role of crystal defects in seeding the transition has been investigated for the KCl system.[182]

5.5 Conclusions

The study of solid-solid phase transitions offers important insights into the rules that govern the formation and determine the symmetry properties of crystal systems. Displacive and order-disorder transitions can be well-understood from a group theoretical point of view, while reconstructive transitions are more mysterious and analytically challenging. Reconstructive transitions are also an under-examined class of phase transitions. Detailed examination of phase transition mechanisms can be used to help deduce interatomic interaction properties that have high transferability.

Chapter 6

6.1 Interatomic interaction functions

In the effort to predict the behavior of crystal compounds researchers have explored using a broad variety of theoretical and computational models. One of the earliest and simplest of these models posits that interatomic forces obey the principle of superposition and that therefore the net potential energy of an individual atom can be described as the sum of contributions from the surrounding structure. While the inescapable fact that the world is quantum mechanical means that a model of this kind is very different from what we consider to be the fundamental nature of reality, it is nevertheless still possible for such models to accurately predict material properties that are consistent with experimental observations in many cases. Mathematical formulations used to calculate contributions to the potential energies of individual atoms in these kinds of model systems are called interatomic interaction functions.[183,184] There are two main forms of interatomic interaction functions, and these are pairwise functions, and many-body functions.[158,185,186] Interatomic interaction functions are used to investigate the microscopic behavior and properties of systems involving atomic motion and are applied using computational mechanistic simulation methods including molecular dynamics (MD) and Monte Carlo simulations.

All forms of interatomic interaction functions contain parameters that are derived either empirically, by fitting against experimental data, or theoretically, by fitting against data obtained through ab initio calculations. These fitted parameters are the numerical constants of the interatomic interaction functions, and the reliability of an atomistic model is determined by how well, and under what conditions, they reproduce the properties of the physical system. The

process of deriving these parameters and the factors that influence their fidelity are therefore of critical importance for advancing the field of computational atomistic dynamics.

The ability of a model to accurately predict the behavior of a system under conditions other than those that its parameters were directly fit to reproduce is sometimes referred to as its transferability. Theoretically derived functions (using ab initio methods) for a compound tend to give a moderately sized but relatively consistent level of error in predicted properties (compared to experiment) across a wide range of simulated conditions.[110] Empirically derived functions, conversely, tend to predict experimental properties with very low error when the simulated conditions are close to the conditions of the experimental data used for fitting their parameters, but tend to exhibit rapidly increasing levels of error as simulated conditions diverge from the experimental conditions.[187] In other words, ab initio based models have higher transferability than empirical models, and empirically based models can achieve greater accuracy than ab initio models. Ab initio calculations are not very precise (for purposes of interatomic potential derivations) when predicting atom positions and lattice dimensions in inorganic crystals with predicted unit cell volumes usually differing by more than 5% from experimental values even for small unit cell phases like perovskites.[40,41] Ab initio methods are far less accurate when used to calculate elastic properties, with differences between calculated and measured bulk moduli on the order of 50% being common. Consequently, until advances in ab initio methods allow for more accurate structure predictions at lower computational cost, there are significant advantages to deriving potential function parameters empirically.

6.2 Pairwise Models

Pairwise interaction functions were used to model the behavior of the crystalline alkali halide salts as early as the 1930s, and are still often applied today.[186,188,189] The pairwise formulation of interatomic interactions is the simplest model, as it does not formally address angle dependent effects or electron delocalization. Pairwise potentials can be very effective when used to simulate the behavior of ionic solids or fluid systems. For crystals with delocalized electrons, such as metals, or those with significant covalent bonding, such as crystals of organic molecules, pairwise potentials are less successful at reproducing experimental behavior. When studying metals an embedded atom model is most often used to calculate atomic potential energies. Covalent systems, when treated in an atomistic manner for MD simulations, frequently use bond order potentials, a class of many-body potential functions.[190,191]

Pairwise interatomic interactions functions are based on the assumption that the potential energy of one atom is the sum of individual potential energies between that atom and every other atom in the structure. Within a pairwise model, every interacting pair of atoms in a structure generates a pair of force vectors that act on the two atoms. These force vectors are oriented parallel to the line separating the atoms and have a magnitude that is a function of the distance between them. The function of distance that determines the magnitude of the force is unique for every pair of atom types in the structure. This simply means that the interaction between an oxygen atom and a fluorine atom, for example, is found using a different function than the function used to find the interaction between two oxygen atoms. The number of pair functions required to model a system is a function of compositional complexity. For a compound containing n types of atoms/ions the number of unique pair functions is n*(n+1)/2. While a

simple binary salt needs only 3 functions, a compound with 5 unique ion types requires 15 pair functions.

Interatomic interaction functions must be dominated by repulsive terms at very short distances in order to reflect the behaviors of real atoms. Short-range repulsion between atoms is associated with the exclusion principle and is often referred to as Pauli repulsion. Interaction functions must also reproduce coulombic behavior as interatomic distances become very large. This is especially important for ionic systems and many pairwise functional forms use the Coulomb equation for point charges as one of their components.

There are many functional formulations used for pairwise interatomic potentials. To illustrate, the General Utility Lattice Program (GULP), an atomistic simulation program, allows a user (as of version 4.2) to apply 33 different forms of pairwise interaction functions.[106] The formulation most commonly used for atomistic simulations of simple solid state ionic systems, like the alkali halides, is probably one developed by, and named for, Born, Huggins, and Meyer, in the 1930s.[186,188,189,192,193] The Born-Huggins-Meyer (BHM) potential for interactions between pairs of ions uses an exponential term to mimic the short range Pauli repulsion and two power law terms to account for dipole-dipole and dipole-quadrupole effects. These terms are added to a standard coulombic interaction using the formal charge on the two ions.

$$V_{\alpha\beta}(r_{ij}) = \frac{q_\alpha q_\beta}{4\pi\varepsilon_0 r_{ij}} + A_{\alpha\beta} * e^{\left(B_{\alpha\beta}(\sigma_{\alpha\beta} - r_{ij})\right)} - \frac{C_{\alpha\beta}}{r_{ij}^6} - \frac{D_{\alpha\beta}}{r_{ij}^8}$$

eqn. 2

In eqn. **2**, $V_{\alpha\beta}(r_{ij})$ is the pairwise potential contribution for the interaction between atoms i of type α and j of type β as a function of the distance r_{ij} separating them, q_α and q_β are the charges of the ion types, the variables $A_{\alpha\beta}$, $B_{\alpha\beta}$, and $\sigma_{\alpha\beta}$ parameterize the Pauli repulsion contribution, and $C_{\alpha\beta}$ and $D_{\alpha\beta}$ parameterize the dipole-dipole and dipole quadrupole contributions respectively. Simpler forms of pair interaction functions, such as the Lennard-Jones or Van der Waals potentials can often be used for modeling systems like atomic gases or other non-ionic fluids.[194,195]

Pair potentials have significant limitations, such as trouble reproducing the behavior of atoms with lone pairs of electrons and the angular dependence of covalent bonding in molecules. There is also an often mentioned but rarely sourced claim that pairwise, centric forces possess a fundamental inability to fully describe the elastic properties of cubic, monatomic crystal systems, at least those for which every atomic site is also a center of symmetry.[196] In particular, the statement holds that the Cauchy relation $C_{12}=C_{44}$ is always obtained from the mathematical derivation of these terms when using pairwise forces, while the Cauchy relation is not observed by experiment. The topic was debated in the literature through the first half of the 20th century.[197,198] While the assumptions that must be made (linear relationship between displacement and restoring force) to reach this conclusion do not strictly hold even for pairwise centric forces, it is nevertheless clear that purely pairwise interactions are insufficient to fully describe the elastic properties of all materials.

6.3 Many Body Potential Models

Modern atomistic dynamic simulations of molecular compounds (organic compounds, biological macromolecules, polymers, etc.) are often done using many-body potentials.[191] The

motivation for this is that solving the complete Schrodinger equation for complicated systems (more than a few hundred atoms or so) is still computationally unreasonable. Many-body potentials can reproduce more varied behaviors than pair potentials, but this comes in exchange for increased complexity and greater computational expense. Interatomic potentials are referred to as many-body when the potential function equations depend on the relative positions of three or more atoms. A simulation using a pair potential model with n atoms requires a number of calculations proportional to n^2 per step. The number of calculations per step using a three-body potential model is proportional to n^3, for a four-body potential it is proportional to n^4 etc.

6.4 Embedded Atom Models

When simulating metallic compounds, which have delocalized electrons, the form of interatomic potential function commonly used is the embedded atom model (EAM), which depicts the structure as point particles embedded in a "cloud" of electron density.[199] The embedded atom model is slightly reminiscent of the "Plum Pudding" model of the atom, proposed by J. J. Thomson prior to the discovery of the nucleus.[200] In an EAM function a pairwise potential between atomic nuclei is combined with an "embedding function" and a function for contributions to the electron cloud charge density from each atom as a function of the distance from them.

$$E_i = F_\alpha \left(\sum_{i \neq j} \rho_\beta(r_{ij}) \right) + \frac{1}{2} \sum_{i \neq j} V_{\alpha\beta}(r_{ij})$$

eqn. 3

In the EAM   eqn. 3 E_i is the potential energy of atom i of type α, F_α(x) is the

embedding function for an atom of type α into an electron cloud with a charge density of x,

$\rho_\beta(r_{ij})$ is the function that determines the contribution by atom j of type β to the electron cloud at

the position of atom i, and $V_{\alpha\beta}(r_{ij})$ is a pairwise potential function for the interaction between

atoms i and j. An EAM function therefore requires two more functions per atom type than do

pairwise potentials.

6.5 Fitting Potential Function Parameters

When interatomic interaction function parameters are fit empirically, the experimental

conditions represented by the data are often limited, because the individuals running the

simulations are usually not the same people who perform the experimental measurements.

Parameter fitting is rarely done exclusively and directly to experimental values collected for the

purpose of fitting, instead, extrapolations that are themselves fit to experimental results already

in the literature are used to artificially increase the size of the data set.[201,202] Extrapolations used

for this purpose involve mapping the atomic positions in an experimental crystal structure onto

thermodynamic equations of states, such as the Mie-Grüneisen equation of states which

incorporates the relationships between lattice volume and vibrational properties, or the Birch-

Murnaghan equation of states which relates pressure and lattice volume.[116,203-205] These kinds of

extrapolations implicitly treat atomic positions within crystal lattices as having linear

relationships with lattice dimensions, an often inaccurate assumption. While interatomic

interactions and changes in atomic positions with temperature and pressure must reproduce the

thermodynamic properties of the bulk material, the thermodynamic properties cannot be used to

obtain the corresponding changes in atom positions. This is a general statement and is true for all phases of all materials.

Performing experiments on samples and refining function parameters to fit the resulting data can be a dauntingly time-consuming challenge, particularly for complex systems. The number of parameters that are needed to model a system increases rapidly with the number of species present in the system. A pairwise model of a material with 5 ionic species, for example, has 15 unique pairwise interaction functions, while a material with 2 species requires only 3 functions. That means fitting 15 times the number of parameters for a single interaction function. Pairwise interaction functions often have at least 4 independent fitted parameters, giving a total of 60 parameters to fit for a 5 ion-type material. Researchers usually try to avoid tackling such difficult parameterization problems.

6.5.1 Quality Data Makes Good Data Sets

When compiling a library of fitting data for a system of interest there are several concepts that are useful to keep in mind. When selecting crystal structures to use, any that contain sites of partial or mixed occupancy should be avoided as they complicate the calculation of interatomic potentials and compromise the reliability of the interatomic distances. For fitting to multiple experimental structures the R-factors that represent the precision of the individual crystal structures can be used to modify their importance to the function that evaluates the fit at each refinement step.[205]

The amount of experimental fitting data required to have a unique fit for a system increases with the number of parameters being refined. More complex systems require more

independent parameters. This is partially compensated by the fact that complex crystal structures contain more data than do simple structures. The point symmetry of atom sites also impacts the usefulness of the data for fitting. Atomic sites that are positioned at centers of inversion or of improper rotation point symmetry are nearly useless for structure-based fitting purposes because the sum of all pairwise interatomic forces on atoms at such sites is always zero, regardless of the function form and parameter values being used. This results from geometry and the only role for such atom sites in structure-based fitting processes is as contributors to the internal pressure.

6.5.2 Fitting Procedures

The actual process of fitting consists of optimizing the parameters of the interatomic interaction functions so that the model reproduces values for a set of known physical properties. For purely structure-based fitting, the physical property to be reproduced is the magnitude of the net force vector acting on each atom site which must be zero for all atoms at static equilibrium.[205] The fitting process is an iterative refinement, applying some user defined form algorithm to optimize a least squares sum of the deviations between calculated and accepted values. In a single refinement step, calculated properties for the experimental structures using some starting set of parameters are compared to the results for several slightly altered parameter values, and the set of parameters that most closely matches the accepted values for those properties is used as the starting condition for the next refinement step. Implementation of this process, despite its relative conceptual simplicity, can be far more time consuming for complicated systems, than actually performing dynamic simulations.

The "fit data" refers to the set of experimental values used to parameterize the interatomic potentials functions. These can be in the form of bulk elastic properties, atomic

structure data, or bulk electrical properties. In an earlier chapter I discussed nonlinear variation of atom positions and bond lengths with respect to changing temperature and pressure. When bulk crystal phase equations of states are used to enhance fit data, this nonlinearity is not taken into account, unless the symmetry of the phase being fit is so high that all atom sites are precisely defined by the unit cell dimensions. The fitting process minimizes the net force on each atom while matching the internal pressure to the pressure conditions of the fit data. Consequently, using equations of states to artificially increase the size of the data-set being fit can lead to deviations from real behavior and limit the transferability of empirical interatomic interaction functions.

Single crystal X-ray diffraction provides the dimensions of the crystal unit cell, as well as the time and space averaged distribution of atoms within that unit cell. The temperature and pressure at which a crystal structure is collected impact both the dimensions of the unit cell and the observed positions of the atoms. For high symmetry crystal structures, such as the B1 and B2 structures adopted by the alkali halide salts, fractional atomic coordinates cannot change without a phase transition taking place. For structures of lower symmetry, fractional coordinates of some atoms can shift without an associated a phase transition. Atoms in crystals have symmetry restrictions on their fractional positions and multiplicity within the unit cell. The various combinations of restrictions possible in a given space group are referred to as the Wyckoff sites.

In the previous chapter I discussed the concept of dynamic disorder, and the fact that dynamically disordered atoms appear to be ordered, by crystallographic methods, and that they are observed at positions that are different from nearby sites of minimum local potential energy. The process of fitting empirical structure data interprets the experimentally observed atom site as

locally minimized potential energy sites. Consequently, a crystal structure that has a dynamically disordered atom site will cause the fitting process to generate interatomic interaction function parameters that inaccurately reflect the behavior of the system because they generate a stable atom position at a location that is not stable. The reliability and transferability of interatomic interaction functions is strongly dependent on their ability to generate potential energy landscapes that match as closely as possible to those of the real system. Dynamic disorder is difficult to identify and can only be realistically disregarded as a possibility in structures collected at cryogenic temperatures. The zero point energy of most vibrational modes in crystals is very small (~0.0081eV for the [111] vibration in Germanium).[206] The minimum energy positions for a dynamically disordered atom with a transition barrier small enough to be overcome by the zero point energy would be expected to be very close to each other, limiting the errors caused by any dynamic disorder present at cryogenic temperatures.

6.6 Conclusions

Ordered single crystal structures, determined experimentally at temperatures approaching absolute zero, closely resemble energy minimized arrangements of their constituent atoms, with the deviation from such a configuration related to the temperature of the system. The net force on each atom in a "static", energy-minimized, crystal structure is, by definition, zero. The fundamental nature of reality prevents any arrangement of atoms from being truly static, and even at the lowest achievable temperature. The internal pressure on such a crystal in equilibrium with its surroundings is exactly equal to the external pressure. Interatomic distances change in response to changes in the pressure on a crystal. Pressure, unlike temperature, is not inherently entropic, and crystal structures collected at any isotropic pressure can be as close to static

equilibrium as the temperature will allow, and cryogenic temperatures get crystal structures as close as experimentally achievable to energy-minimized and static conditions. Experimental single crystal structures collected at such temperatures and at multiple pressure conditions can be used to probe the potential energy surface of the system with maximum resolution and accuracy. This approach is ideal for building empirical data sets for fitting precise interatomic interaction function parameters.

Interatomic interaction functions are a fundamental component of atomistic dynamic simulations. They approximate the potential energy of individual atoms as functions of their environment. The simplest class of interatomic interaction functions is pairwise potentials, which treat atom pair interactions as centric, independent, and superimposable. Metals and molecular crystals require more complicated kinds of interatomic interaction functions, and various many-body potentials are used when simulating one of these kinds of systems.[199] Interatomic interaction functions for are developed by fitting parameters to sets of accepted data that is either experimental or theoretical in origin.[110] Empirical models develop functions using experimental data for the fitting process, while ab initio-based models use a set of data obtained by theoretical methods.[116] Ab initio models have greater transferability than empirical models, while empirical models can make much more accurate predictions within their ideal temperature/pressure regimes.[105] The impact of thermal vibrations on experimental data used for fitting empirical parameters can limit the transferability of empirical models. The transferability and accuracy of empirical models is maximized when parameters are fit to high quality single crystal structures collected at very low temperatures and multiple pressures.

Chapter 7

7.1 Molecular Dynamics Concepts

Molecular Dynamics (MD) is the application of the Newtonian laws of mechanics to molecular or atomistic models of physical systems in order to simulate the evolution of the systems over time.[207] An atomistic molecular dynamics simulation defines a set of atoms in a simulation "supercell", and each atom in this supercell is an independent particle. Because these simulations are n-body problems and therefore lack general analytical solutions, numerical methods of integration are used and changes over time are computed in a step-wise manner.[208,209] Systems are evaluated at discrete intervals of time with the momentum of the particles, the size of the time step interval, and the forces acting on the particles at one "frame" used to determine the change over the following interval.[208] Atomistic MD usually employs interatomic interaction functions to determine the instantaneous forces on each atom at each frame, and these forces are in turn used to modify the momenta of the individual atoms, as well as for calculating the internal pressure of the simulated system.

Molecular dynamics has applications in materials science, fluid dynamics, biochemistry, catalysis, and polymer chemistry among many other fields.[210,211] MD is used for refining crystal structures of biological macromolecules and in attempts to simulate protein folding, which is one of the most daunting problems in all of modern science. The main challenges to be addressed when performing MD simulations are ensuring that the functions used to calculate the interatomic or intermolecular interactions accurate reproduce the potential energy surface for the simulated conditions, ensuring that the simulation constraints reflect the intended conditions, and

optimizing simulations to keep the computation costs reasonable without interfering with the results.

7.2 Periodic Boundary Conditions

When applying molecular dynamics to the behavior of bulk crystalline systems, periodic boundary conditions (PBCs) are used.[207,212] PBCs are conceptually identical to the boundaries of a crystallographic unit cell, in that they describe an infinite system as a repeated volumetric unit. It is necessary to select periodic boundary conditions carefully, as they are capable of generating "correlational artifacts", properties that arise from the dimensions or periodicity imposed on the system by the applied PBCs. For example, vibrational wavelengths of calculated phonon modes are constrained by the dimensions defined by PBCs.[213]

An important component of MD simulations is the selection of a summation method to use for approximating long distance interactions. When calculating the electrostatic potential of a point charge in a neutral crystalline lattice composed of point charges, the sum of the potential contributions from all other point charges is conditionally convergent. That means that the infinite sum of contributions only converges if the sum is performed in the correct way, giving the so-called Madelung constants for the lattice.[214,215] The Ewald summation method and its variations, such as the particle mesh Ewald method, are often used for this purpose.[216] The sum of long range coulombic interactions within an ionic crystal lattice is the Madelung constant problem, which the Ewald summation was originally developed to address. Ewald summation divides the infinite sum of pairwise interactions into two parts a short range part which converges in real space, and a long range part that converges in reciprocal space, consequently, a cutoff radius must be chosen to separate the two parts. The Wolf summation method is a more

recently developed alternative that has greater computational efficiency than the Ewald method.[217] A recent review of various summation methods found that for reasonably large cutoff radii (~20Å), the results of the Ewald and Wolf summation methods are effectively identical.[218]

7.3 Simulation Ensembles

Partition functions represent thermodynamic ensembles and are used to describe systems on the basis of which of the system's thermodynamic state variables are constant and which are allowed to change over time.[219] A thermodynamic ensemble is the collection of possible microstates of a system that satisfy a set of 3 constrained state variables. The partition function of an ensemble describes the possible microstates of a system by fixing the same 3 state variables, making it possible to define the other state variables as functions of each other. When performing computational simulations of a chemical system, thermodynamic ensemble is determined by the properties that the simulation allows to change over time. Three ensembles frequently used in MD simulations are the microcanonical (NVE), canonical (NVT), and isothermal-isobaric (NPT).[106,220,221] The letters in parentheses indicate the state variables that are held constant for that ensemble (N = particle number; V = volume; E = total energy; T = temperature; P = pressure).

7.4 Thermostats

In order to hold a thermodynamic state variable constant, a simulation requires a method for calculating the value of that state variable and a mechanism for adjusting the system to maintain the state variable at its assigned value. In other words, if a MD simulation is intended to maintain a constant temperature, the program needs a way to measure the temperature and a way to adjust the temperature of the system. For some state variables, such as system volume and

particle number, this can be trivial. Calculating values for the temperature and pressure of a simulation system are more challenging and present interesting problems.

Temperature manifests at the atomic scale as kinetic energy. The macroscopic temperature of a system has a magnitude proportional to the time-averaged kinetic energy of all the particles in the system. It is therefore a statistical property and can be calculated for large systems by eqn. 4.

$$T = \frac{2}{3 * k_B} \overline{\left(\frac{1}{2} m_i v_i^2 \right)}$$

eqn. 4

Where k_B is the Boltzmann constant and the over-lined segment indicates the average value of the kinetic energy of all the individual particles in the system. Using this equation, the calculated temperature of a simulated finite system will fluctuate over time reflecting the constantly changing values of kinetic and potential energy for individual atoms and, by extension, the whole system. These fluctuations are statistical noise and will occur even for simulations of systems that are in what would be considered thermal equilibrium. Being statistical in nature, this "temperature noise" has a magnitude that is inversely related to the number of particles in the system. The consistency of the calculated temperature of a simulated system can be increased, either by increasing the number of atoms in the simulated supercell, or by averaging the calculated temperatures over multiple time steps.

Adjusting the temperature of a simulated system is done by applying a thermostat mechanism. Thermostats, in the context of MD, are mathematical functions to adjust the

temperature of the system by changing the kinetic energies of the individual atoms. There are

several popular thermostats, one of the most common is a simple velocity scaling mechanism,

where the instantaneous velocities of all atoms in the simulated system are multiplied by a factor

λ found by eqn. 5 where T_0 is the set temperature and $T(t)$ is the instantaneous temperature.

$$\lambda = \sqrt{\frac{T_0}{T(t)}}$$

eqn. 5

A thermostat that allows more fluctuation of the system temperature, which can be

beneficial when the simulation supercell is small, is the Brendensen thermostat, which

fractionally scales particle velocities by an amount proportional to the difference between the

calculated and set temperature and modified by a user determined coupling constant.[222] This

thermostat scales the atom velocities by a factor λ determined by eqn. 6 where τ_T is a time

constant associated with the coupling.

$$\lambda = \sqrt{\left[1 + \frac{\Delta t}{\tau_T} * \left(\frac{T_0}{T(t)} - 1\right)\right]}$$

eqn. 6

7.5 Barostats

We understand the concept of pressure on the macroscopic scale as the force a system

exerts per unit volume on a surface at the boundary of the system. When describing a system

using periodic boundary conditions there is no real boundary surface. This complicates the

understanding of internal pressure for computation-based simulations. Just as every action has an

equal and opposite reaction, the force vector exerted by atom i on atom j is equal in magnitude to the force vector exerted by j on i and is oriented in the opposite direction. Forces between pairs of particles are either attractive or repulsive. Attractive forces can be thought of as contraction forces and repulsive forces as expansion forces. By multiplying the force vector on an atom by the distance vector separating that atom from the origin of the force, as is done in the virial expression below, we arrive at a mathematical expression for the pressure.

While developing the MD simulations that I performed as part of my own research, discussed in the next chapter, I found that much of the literature that establishes the mathematical groundwork for modern MD simulations is derived using either the Hamiltonian or Lagrangian reformulations of classical mechanics. These reformulations produce the same results as Newtonian mechanics and have distinct advantages over the classical formalism for deriving general principles. However, Hamiltonian and Lagrangian mechanics are much more mathematically abstract than the classical formulation, making it much harder to develop an intuitive understanding of the situations being described in these papers. The barostat system of Parrinello and Rahman, for instance, is derived in their paper by using the Lagrangian formalism and tensor expressions of physical properties.[223] In the following section I will be attempting to explain the MD pressure concepts in more readily understood Newtonian formulations.

A commonly used equation for computing the internal pressure of a system of N particles that uses pair interactions is the virial pressure equation for systems in equilibrium

eqn. 7, where p is the pressure, k_B is the Boltzmann constant, T is the simulation temperature, N is the number of atoms, V is the supercell volume, the over-line of the

sum indicates an average taken over time, f_{ij} is the force on atom i exerted by atom j, and r_{ij} is the

distance vector going from i to j.

$$p = \frac{k_B * T * N}{V} + \frac{1}{V * 3} \overline{\sum_{i<j} f_{ij} r_{ij}}$$

eqn. 7

This equation defines the internal pressure of the system in virial expansion terms as

modifications to the ideal gas pressure. The macroscopic pressure is a statistical property that, in

the form given above, is partially a function of the system temperature, which is also a statistical

property, making this expression less accurate for non-equilibrium situations. The internal

pressure can also be calculated in an instantaneous manner. This is done by omitting the

temperature dependent component of the virial pressure equation and using an instantaneous sum

for the second component instead of a time averaged sum (eqn. 8).

$$p(t) = \frac{1}{V(t) * 3} \sum_{i<j} f_{ij}(t) \, r_{ij}(t)$$

eqn. 8

As one would expect, the instantaneous pressure fluctuates over time much more than the

standard virial pressure. This can be either advantageous or detrimental for simulation purposes,

depending on the system and processes being studied.

For an isothermal isobaric ensemble (NPT), a barostat must be applied to accommodate

changing internal pressures by adjusting the simulation supercell dimensions. Andersen

developed a barostat that enables the simulation supercell to expand and contract in response to

changing internal or external pressures, but does not permit independently changing supercell dimensions or variation of supercell angles.[221]

An alternative, the Berendsen barostat, allows the three supercell side lengths to change independently and is similar in function to the Berendsen thermostat, using essentially the same mechanism.[222] Unfortunately, the time-scaling mechanism employed by the Berendsen thermostat/barostat has been shown to produce "artifacts" when used in MD simulations. One of these involves violations of the principle of equipartition of energy in simulated systems, producing a "flying ice cube" effect, so care must be taken when using this barostat.[224]

The Parrinello-Rahman barostat allows unconstrained evolution of the supercell dimensions and angles, and scales the rate of variation of the supercell using a constant of proportionality in the form of an artificial mass that gives inertial behavior to the lattice constants.[223] Parrinello and Rahman described their barostat concept using Lagrangian mechanics and what follows is an attempted translation of the concepts in the interests of clarity. One challenge that arises when using the internal pressure to change the lattice constants of a simulated supercell is that a set of 3 axial pressure vectors cannot generate all of the lattice changes that are possible. The number of lattice constants that can be changed for an unconstrained supercell is 6 (a, b, c, α, β, and γ). The sum of pressure contribution vectors along a-, b-, and c-axes can only be used to derive changes in a, b, and c lattice constants. To generate changes in α, β, and γ constants (the lattice angles) at least 3 additional pressure vectors are required, those can be the ab, ac, and bc (face diagonal) internal pressure vectors. These new vectors cannot be derived from the net a, b, and c, pressure vectors, contributions to them must be calculated for each interatomic force vector individually. The expression for the net pressure

vector in the *a*-axis is given as an example by   eqn. 9 where $\hat{a}$ is the

unit vector oriented along the *a*-axis.

$$p_{\vec{a}}(t) = \frac{\hat{a}}{V(t)*3} \sum_{i<j} f_{ij}(t)\, \vec{r}_{ij}(t) \circ \hat{a}$$

eqn. 9

The instantaneous pressure of the simulated system for expansion or contraction of one of

the lattice constants can be written as a vector as discussed above. The dot product of that vector

(combined with the external pressure vector) with the normal vector of the plane in the supercell

gives the magnitude of the force per unit area perpendicular to that plane. The Parrinnello-

Rahman barostat uses this force and a constant of proportionality that takes the form of an

arbitrary mass to impart momentum to changes in lattice dimension values.

7.6 Randomness in Simulations

MD simulations can be run in a purely deterministic fashion, so that the behavior of the

system is entirely dependent on the starting conditions of the system. However, depending on the

purpose of the simulation, it can be very advantageous to incorporate randomization processes.

For example, in a simulation using NPT type conditions, the system exchanges heat with its

surroundings. Incorporating randomness into the distribution of the thermal energy added to or

removed from the simulated system can increase the rate of phase space exploration by the

system and avoid the errors associated with deterministic simulations. As with many other

aspects of MD simulations, care must be taken when incorporating randomizing processes.

Randomized changes to particle momenta should be in small increments compared to the rate of

deterministic changes. This helps prevent the randomizing processes from being the cause of

changes rather than just redirecting the path of the simulated system through phase-space. Just as purely deterministic MD simulations with slightly different starting conditions can look very different from each other after a short period of simulation time, small randomized variations in conditions can lead to significant variation as the simulation progresses.

7.7 Conclusions

MD simulations involve a great deal of mathematical and physical complexity. They often require significant computational power to perform, and can be very sensitive to subtle variations in starting conditions. However, when they are correctly formulated using accurate and transferrable interatomic interaction functions they can provide insights into the behavior of physical systems that cannot realistically be obtained through other methods. The continuous advancements made in computational technology and the broad range of applications identified for simulations of atomistic systems suggests that MD and related methods will become much more common in the near future. MD simulations help researchers make sense of confusing experimental results and are a powerful tool for modern scientific investigations.

Chapter 8

8.1 KNaNbOF$_5$ Transition
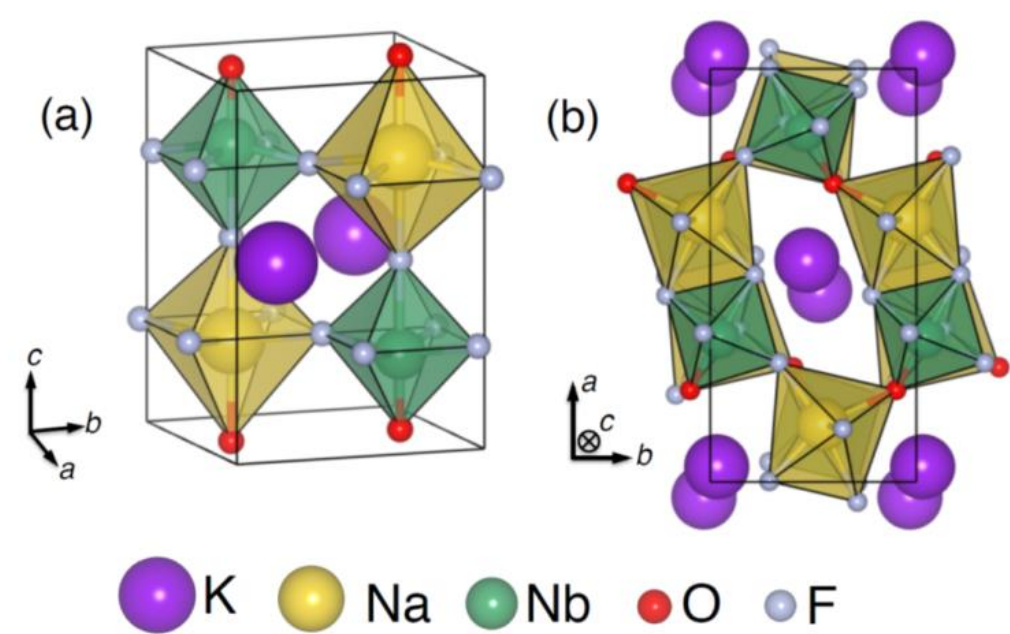
Figure 26: Unit cells for known phases of KNaNbOF$_5$: (a) *P4/nmm* (CS) structure and (b) *Pna21* (NCS) structure.

KNaNbOF$_5$ is a compound of particular interest for the study of noncentrosymmetry in solid state inorganics.[57,58,70,225-227] Two polymorphs of this quinary compound are stable at room temperature.[57] One of these phases is Centrosymmetric (CS) crystallizing in space group *P4/nmm* and the other phase adopts the Noncentrosymmetric (NCS) space group *Pna2$_1$* (Figure 26). The properties of the NCS phase include triboluminescence and a piezoelectric response greater than that of α-Quartz.[225] A temperature induced phase transition linking the CS and NCS phases has been reported. *In situ* XRD experiments demonstrate that at ~360 °C both phases transition to a third high temperature (HT) phase.[58] Upon cooling, the HT phase always reverts to the NCS phase. The structure of the phase observed at 360 °C has not previously been reported.

Attempts were made to index and solve the structure from powder XRD data, but results were inconclusive.[58,225] Both transitions are determined to be of first order based on the observation that initial and final phases are present at the same time during transition (Figure 27). In addition to the difference in space group, the polymorphs of $KNaNbOF_5$ are actually quite distinct. The CS phase has a perovskite-like structure and a higher degree of order in the orientations of $[NbOF_5]^{2-}$ octahedral units. Additionally, there is no K-O coordination in the CS phase, but there is K-O coordination in the NCS phase. The stark contrast between the structures of the two stable polymorphs, the first order nature of the transition, and the absence of a group-subgroup relationship connecting the known phases all indicate that $KNaNbOF_5$ undergoes a reconstructive phase transition. The irreversible nature of the CS to HT step also indicates that it is a reconstructive phase transition.
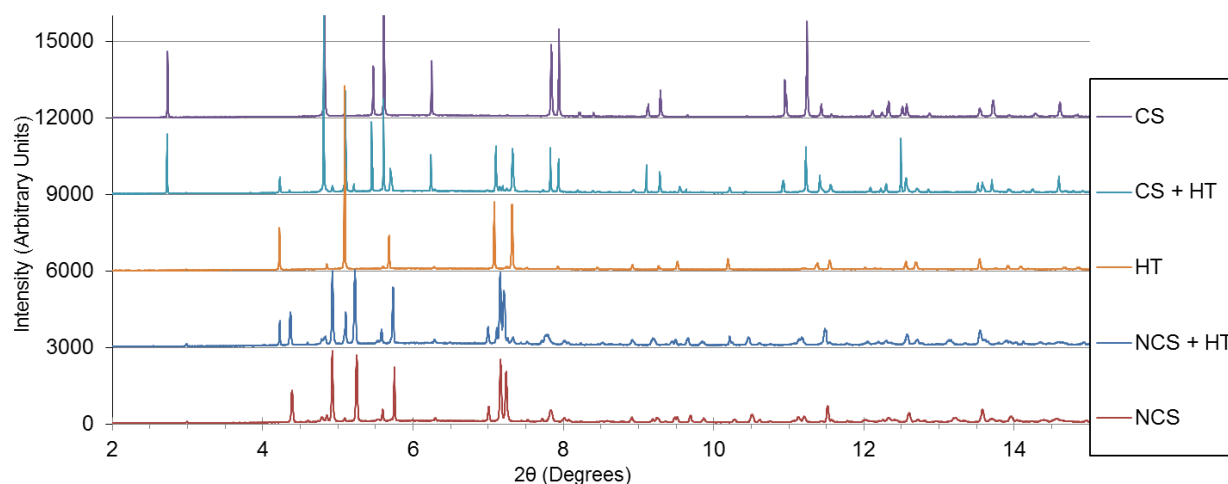
Figure 27: In situ powder diffraction of the CS to HT to NCS phase transitions. The fact that both phase transitions are first-order is confirmed by the simultaneous observation of patterns for the HT phase and the CS (CS + HT) and the NCS (NCS + HT) during either transition.

Our investigations into the nature of the reconstructive CS to HT transition in $KNaNbOF_5$ indicated that polar octahedral $[NbOF_5]^{2-}$ anions within the crystal become disordered between 6 possible orientations as the temperature of the system increases. We found that this process provides the driving force for the reconstructive transition, causes the irreversible nature of the transition, and explains the finding that the newly identified HT phase (space group *Cmcm*) occupies a saddle point on the energy landscape.

Results from our research provided an explanation for the inconclusiveness of the in situ powder XRD analyses. We found the high temperature phase to have orthorhombic crystal symmetry with a strong pseudo-symmetric relationship to a rhombohedral lattice. This relationship, along with the presence of secondary phases observed in all of the high temperature patterns, generated a level of uncertainty in predicted unit cell dimensions that the powder refinement algorithms could not resolve.

8.2 Results and Discussion

High quality in situ synchrotron powder diffraction studies of the phase transitions were performed prior to the beginning of this work. Analysis of this data revealed the existence of the high temperature phase, and showed that the two phase transitions involved were both first order. Attempts to identify the atomic structure, or even the unit cell dimensions, of the high temperature phase by traditional powder solution methods were found to be inconclusive. This complicated the development of a more detailed understanding of the processes involved in the transition.
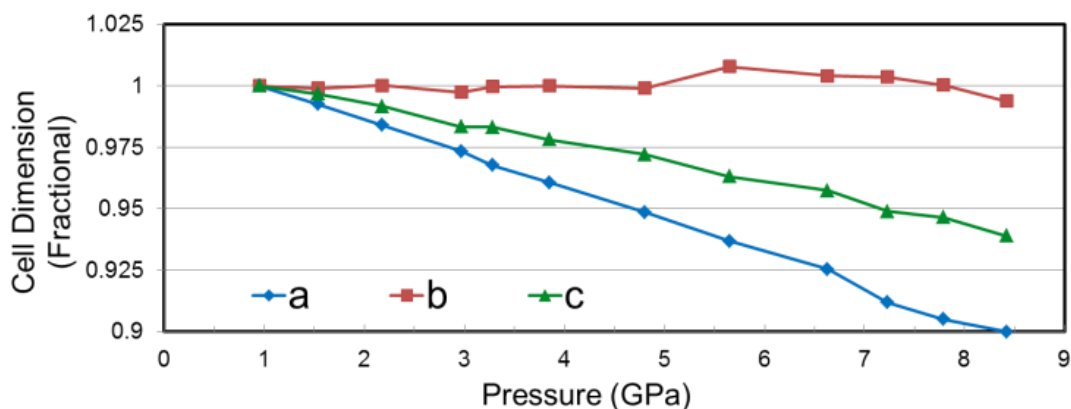
Figure 28: Experimentally observed changes in the lattice dimensions of the NCS phase with pressure at 15 K by cryogenic DAC single crystal diffraction at Argonne National Laboratory. The crystal volume decreases approximately linearly with increasing pressure. In several regions the *b*-axis length expands with increasing pressure. The *b*-axis is longer than its initial value through the 5-8 GPa range, and over the explored pressure range changes only very slightly in comparison to the *a*-axis and *c*-axis. *Experimental uncertainty in the y-axis is too small to depict.*

To understand the reconstructive CS to HT transition in $KNaNbOF_5$, identification of the high temperature, hidden phase is required. We performed molecular dynamics simulations to explore the structural phase space using a uniquely parameterized set of empirical pairwise interatomic interaction functions. Our parameterization method involved an unusual level of experimental rigor, using cryogenic (T = 15K) diamond anvil cell (DAC) single crystal diffraction studies of the lattice and atomic position parameters of $KNaNbOF_5$ over a range of pressures. By this method we successfully simulated the temperature dependent behavior of $KNaNbOF_5$ at atmospheric pressure based on the pressure dependent behavior at low temperatures. Figure 28 shows the observed changes in lattice dimensions with pressure for the NCS phase of $KNaNbOF_5$ at 15K. It is interesting to note that, while the crystal volume

decreases approximately linearly with increasing pressure, the individual lattice dimensions and

bond lengths change inconsistently along the pressure range. These inconsistencies would not be

observed or incorporated by less rigorous empirical fitting processes. The empirical interatomic

interaction function parameters used in the MD simulations were fit to these crystal structures by

minimizing forces and calculated/experimental pressure differences.
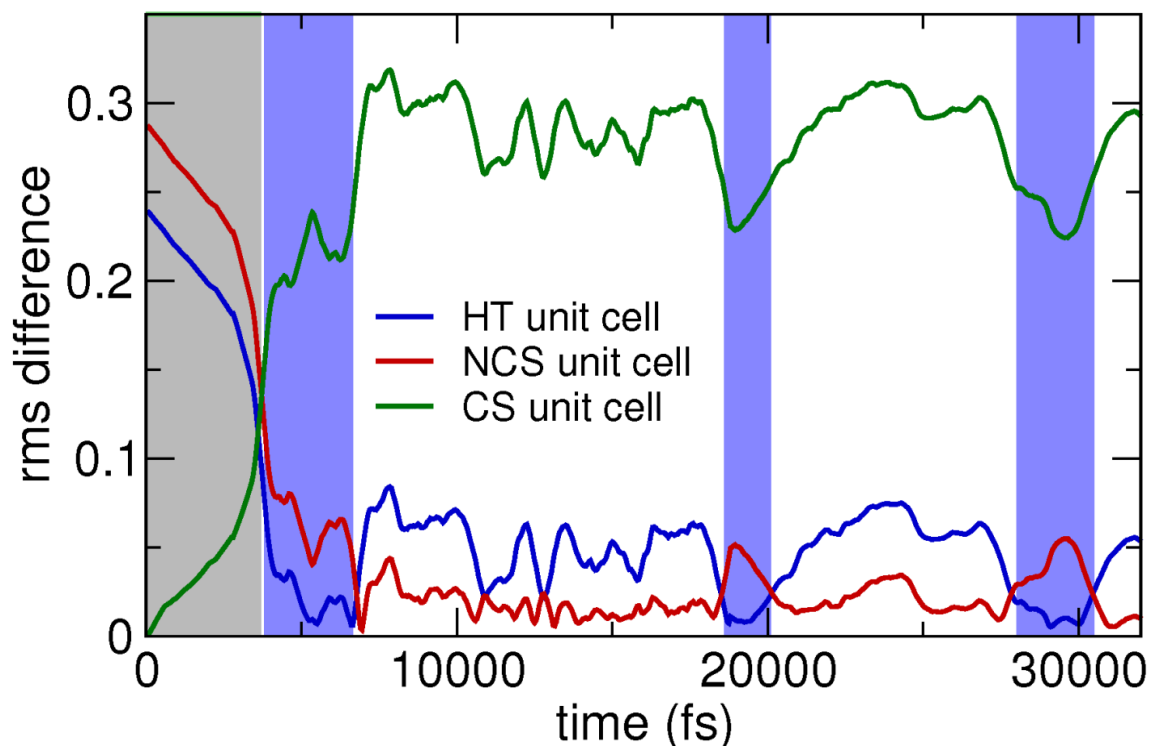
Figure 29: Plot of root mean square differences between the simulated crystal lattice parameters

as a 1ps moving average and the lattice parameters for the three experimentally observed phases

against simulation time; the phase with the lowest value is the phase with the unit cell parameters

that most closely match those of the simulated cell at that time. The simulation is observed to

transition from the CS phase to a HT phase and then to transition multiple times between HT

phases and the NCS phase. The gray highlighted region indicates the period when the simulation was constrained to promote the initial transition and the blue highlighted regions indicate periods when candidate structures for the HT phase were observed. The simulation temperature was held constant at 350 ºC.

Changes in the lattice dimensions of the simulated crystal, as a 1ps moving average, were compared individually to the unit cell dimensions for the CS and NCS phases of $KNaNbOF_5$ and to the dimensions of an orthorhombic cell fit to the most intense peaks of the experimental powder pattern of the HT phase. The root mean square differences between the simulated crystal dimensions and the three experimental lattices are plotted in Figure 29. The simulated supercell can be seen to transition from the CS phase (gray region), to a dynamic system oscillating between an approximation of the HT cell (blue regions) and NCS cell dimensions. There are two distinct phases adopted by the simulation with lattice dimensions matching the experimental powder diffraction pattern of the HT phase, and these were investigated as candidates for the HT phase structure. Space groups for the candidate phases were obtained from P_1 symmetry MD simulation "snapshots" using the online utility FindSym,[228] and identified as belonging to the space groups *Pbcm* and *Pnma*. Careful comparison between the experimental HT phase powder diffraction pattern and simulated patterns for these two phases revealed several low intensity peaks in each of the simulated patterns that are absent from the experimental pattern (Figure 30). The experimental HT phase was proposed, based on this, to be a dynamically disordered phase and to have a super-group relationship to both the *Pbcm* and *Pnma* phases. Throughout the simulation, O and F site positions were found to become disordered. To facilitate space group

identification from the simulation structures, this O/F disorder was artificially removed. The identified *Pbcm* and *Pnma* structures retain artificial O/F ordering.
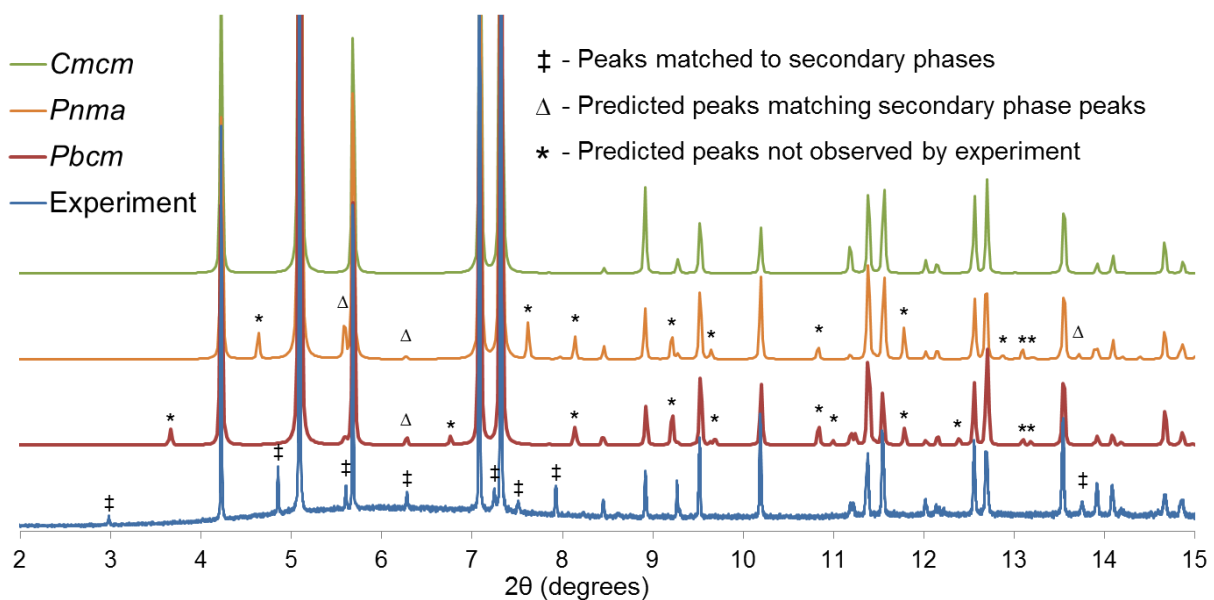
Figure 30: Comparison of experimental powder diffraction pattern for the HT phase of KNaNbOF$_5$, simulated patterns for the two candidate phases, (*Pbcm* and *Pnma*) identified from our MD simulation and the simulated pattern for the proposed average structure for the HT phase (*Cmcm*).

Using the FindSym program we discovered that the cation-only sublattices of the MD predicted *Pnma* and *Pbcm* phases both have *Cmcm* symmetry.[228] A *Cmcm* space group crystal structure with anion positions approximately midway between those of the *Pnma* and *Pbcm* unit cells was constructed (Figure 31). DFT energy minimization was used to relax the positions of the atom sites within the unit cell and the simulated powder diffraction pattern was compared to

the experimental HT phase pattern (Figure 30). The peak intensities matched well and only two of the low intensity *Cmcm* simulated diffraction peaks were absent from the experimental pattern. We found that the extra peaks from the DFT relaxed *Cmcm* phase could be eliminated from the simulated pattern by treating the O and F sites as disordered and removing a corresponding out of center distortion of the Nb site (Figure 32), suggesting, in agreement with the observed behavior of the MD simulation, that the experimental HT phase has disordered O and F sites. Several peaks in the experimental pattern are not present in the simulated patterns. These peaks were matched with various silicates that could form as minor components from side reactions between the sample and glass wool used in the experimental setup.
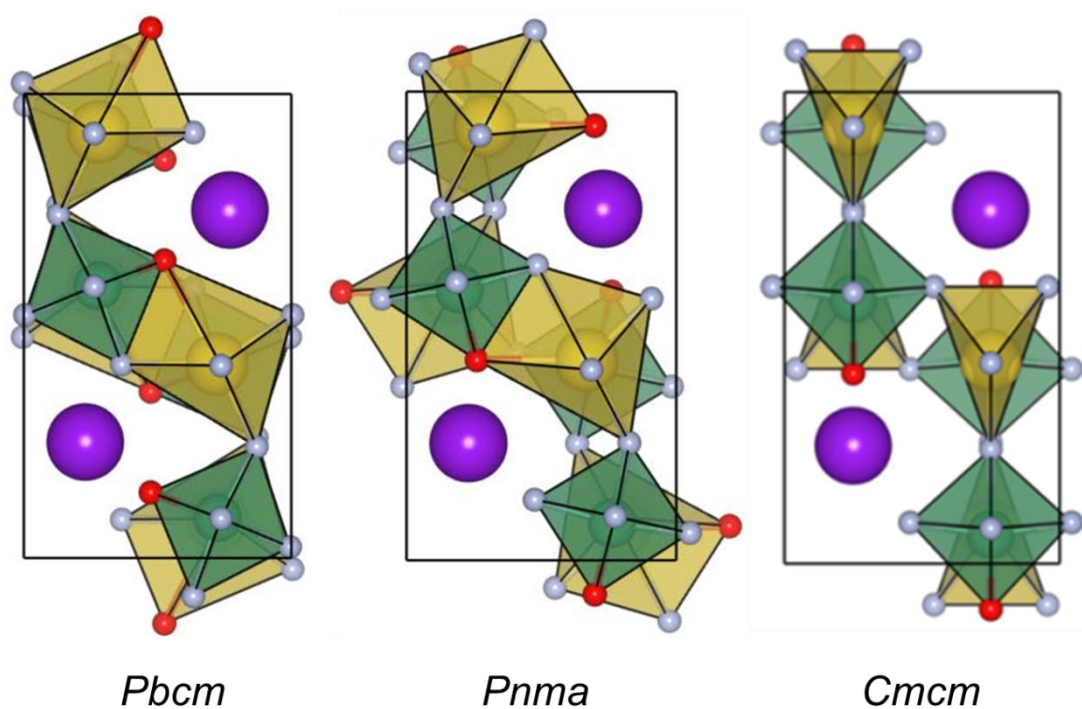
Figure 31: *Pbcm* and *Pnma* crystal structures identified from the MD simulation and the *Cmcm* transition structure. Green octahedra are $[NbOF_5]^{2-}$ units and yellow octahedra are the Na

coordination polyhedra. Potassium ions are purple. Oxygen and fluorine sites are depicted artificially ordered, the simulated structures did not have ordered oxygen and fluorine sites.
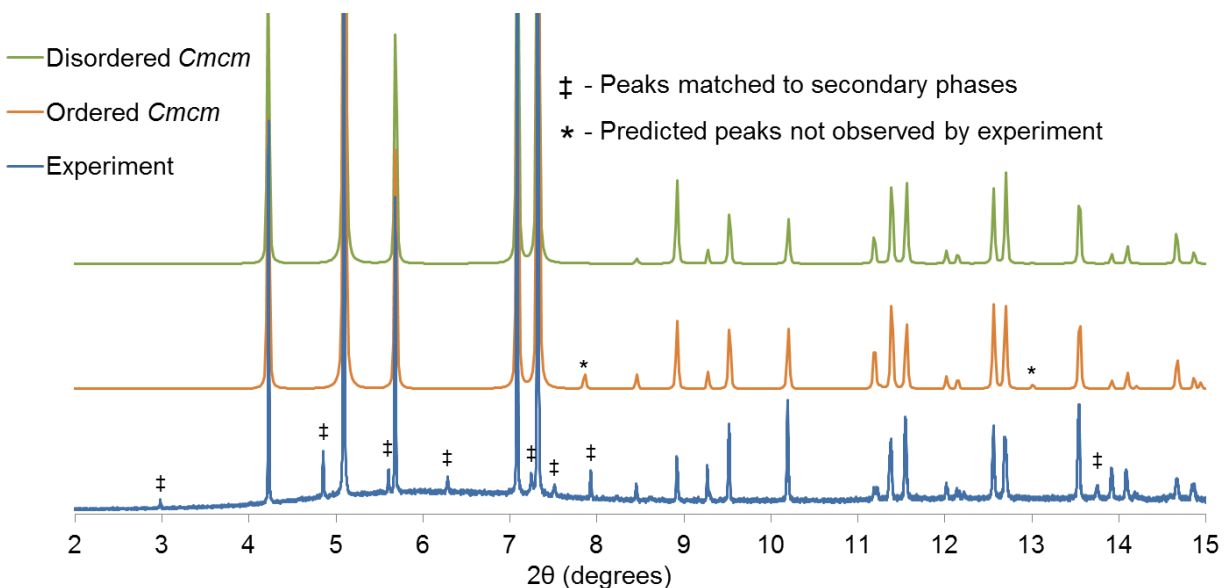
Figure 32: Comparison between the experimental HT phase powder diffraction pattern, a simulated pattern for the ordered minimum energy *Cmcm* structure (obtained by DFT energy minimization), and a version of the *Cmcm* structure in which oxide and fluoride sites are disordered, and the Nb out of center distortion is removed. Two of the peaks predicted for the ordered *Cmcm* structure are absent from the experimental pattern. It can be seen that these two peaks are absent from the pattern for the disordered version of the *Cmcm* structure, supporting the conclusion that the HT phase has disordered oxide and fluoride sites.

Polar anionic $[NbOF_5]^{2-}$ units are constructed from metal-ligand bonds that are much stronger than any other bonding interactions in the $KNaNbOF_5$ system. These molecular anionic

units are so strongly bound that it is unlikely that they dissociate in any of the temperature/pressure conditions investigated in this work. Based on the reported properties of related systems that have been investigated in the past, thermal dissociation of the niobium oxide-fluoride anions should happen when the temperature of the system is somewhere above 600 °C. [27] In our MD simulations, instead of dissociating, the $[NbOF_5]^{2-}$ units were found to undergo rigid rotation events, maintaining the coordination geometry of the Nb cation but changing the direction of the Nb-O bond.

Over the course of the MD simulation, $[NbOF_5]^{2-}$ units were seen undergoing frequent "hopping" type rotation events (Figure **33**). These events allow the dipole moments of the anionic units to become disordered relative to each other without them breaking any of their strong ligand-metal bonds. Previous work, on the compound $K_3WO_3F_3$ provided experimental evidence that indicated the presence of temperature driven reorientations of polar, heteroanionic octahedra leading to displacive order-disorder transitions.[80] In $KNaNbOF_5$ these rigid unit rotation events likely result in a loss of the O and F site ordering as discussed above, and it is also probable that they play a key role in producing the driving force for the reconstructive transition process. "Hopping" rotation events in this system generate a distribution of the octahedral anionic units between six different, locally stable, orientations (Figure 34a). At low temperatures (in both phases) the rate of these events is low, and the crystallography shows a strong preference for a specific preferred orientation of the anion dipole (Nb-O bond axis). At higher temperatures the events are more rapid and the orientations become statically disordered. In the HT phase, the rotation events occur often enough to exhibit dynamic disorder. This

dynamic disorder generates the observed HT phase (*Cmcm*) structure, and also provides an explanation for the unusual coordination environments of the Na^+ and K^+ ions in that structure.
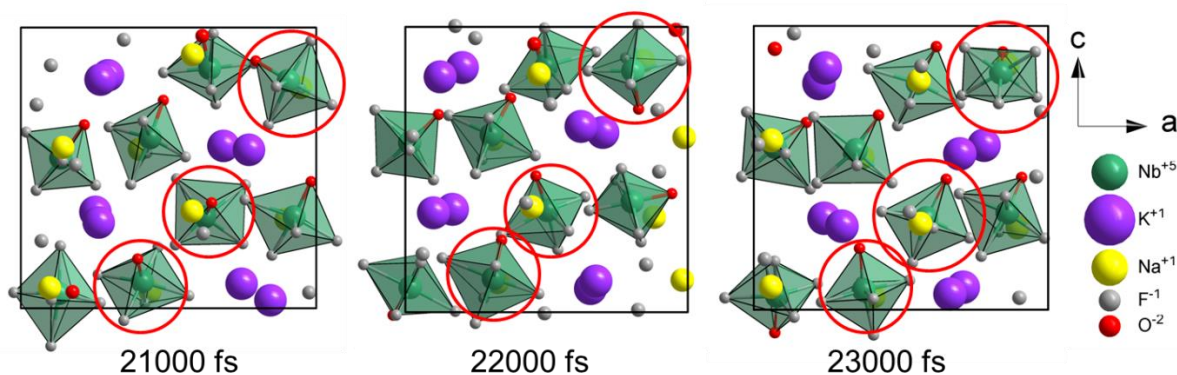
Figure 33: Snapshots of the MD simulation supercell at 1000fs intervals. Hopping rotations of $[NbOF_5]^{2-}$ units with respect to the K and Na cation lattices, which change O/F site ordering, were observed in our MD simulation, the three circled octahedra undergo changes in their orientations over this 2000fs example period. These rotation events occur randomly to individual octahedra (rather than being collective transitions) with a statistical frequency dependent on the temperature.

In related oxyfluoride elpasolites, phase transitions have been reported and characterized as being driven by the development of orientational disorder in octahedral heteroanionic units, the described transitions have always been of the displacive order-disorder type, unlike the reconstructive transition described here.[80,229-231] In the system investigated here, the O/F site ordering is intrinsically coupled to the stabilization of the A-site sublattice (K^+ ions and vacant sites) in the CS *P*4/*nmm* phase. Analogous to a double perovskite, this phase has a structure that contains two unique 12-coordinate cation sites. One of these is occupied by K^+ cations, while the other is vacant. The K^+ sites coordinate exclusively with F^- anions in the ordered CS phase. In

metal oxide fluoride octahedral units O^{2-} anions have a more positive charge associated with them than do the F^- anions.[28] In the CS phase, this arrangement stabilizes the K^+/vacant site distribution. When the O & F sites become disordered (upon heating), this stabilizing effect is removed, and the relative energy of the distribution of K^+ sites and vacant A sites becomes dominated by the electrostatic interactions between nearby K^+ cations, which have acquired an effective positive charge because of their decreased F-site coordination and the corresponding increase in O-site coordination. A merging of the destabilized K^+ sites with the destabilized vacant sites that have acquired an effective negative charge (needed to balance out the effective positive charge on the K^+ sites) takes place. This merging of occupied and vacant sites is the driving force for the reconstructive transition. Dynamic disorder of the $[NbOF_5]^{2-}$ units discussed above catalyzes the transition process, and the static to dynamic disorder transition makes the lattice flexible enough to overcome the reconstructive transition barrier. This contrasts the reported behavior of oxyfluoride elpasolites, which have a strong similarity to the CS phase structure. The elpasolite phases have no vacant sites, and therefore could not be expected to undergo a transition that requires merging of a vacant site with an occupied site.
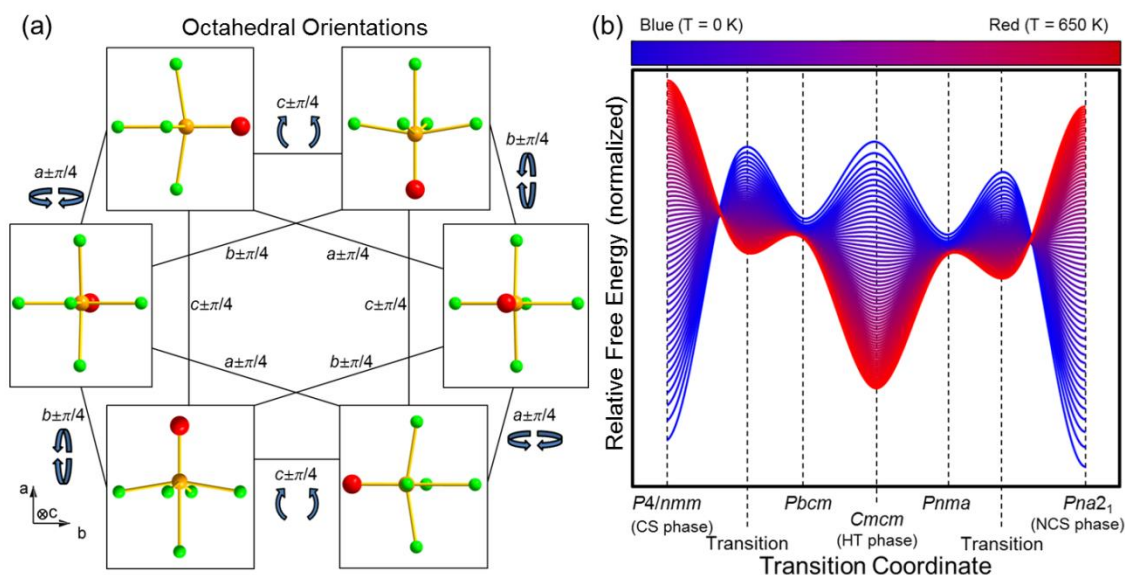
Figure 34: a) Polar $[NbOF_5]^{2-}$ octahedra undergo 90° hopping rotations at a rate determined by the temperature of the system. The rotational axes relating pairs of the 6 stable orientations are indicated. These hopping rotations lead to disorder of the O and F sites and they effectively lower the strength of O^{2-} & F^- bonds with K^+ and Na^+ ions. The order/disorder transition is continuous. b) A qualitative transition state theory plot illustrating the influence of temperature driven octahedral disorder on the free energy landscape of the $KNaNbOF_5$ system. Line colors from blue to red indicate the temperature (in 10 Kelvin increments). When the $[NbOF_5]^{2-}$ octahedra are ordered (at low temperature, blue lines), the CS and NCS phases are stable but, as the temperature rises and the degree of octahedral disorder increases, the *Cmcm* phase that is observed at HT conditions becomes favored. The zero temperature free energy landscape (last blue line) is identical to the potential energy landscape combined with contributions from the zero point energy. The *Cmcm* phase is a transition state and an unstable phase in the potential energy landscape, while in the free energy landscape it becomes the stable phase at high temperature.

8.3 Irreversible transition

A qualitative explanation of the reason for the irreversible nature of the CS to HT transition is illustrated in Figure 34b. The free energy values are shifted and rescaled to show the changes in relative free energy among various structures. The difference between the free energy landscape, which includes finite temperature contributions, and the potential energy landscape is an important one. The potential energy landscape includes only electronic contributions, while the free energy landscape combines electronic contributions with vibrational and configurational entropic effects. Consequently as the temperature of a system decreases, the free energy landscape approaches the potential energy landscape. Systems achieve equilibrium by minimizing their free energy.

A description of the effects of temperature-dependent disorder of the $[NbOF_5]^{2-}$ dipole orientations is useful for this analysis. This disorder changes the potential energy landscape of the system as well as the free energy landscape. In the low temperature ordered state, the CS phase exists as a metastable structure in the potential energy landscape as the polar NCS structure is more stable (Figure 34b). When the $[NbOF_5]^{2-}$ octahedra are disordered, the coordination environment of the layered K^+ cations and vacant cation sites in the CS phase lose the stabilizing influence provided by that order. The result is that the K^+ sites and the vacant sites develop opposite effective charges, and consequently begin to attract each other.

The HT phases (*Pbcm*, *Pnma*, and *Cmcm*) are stabilized because the K^+ and vacancies are combined in these structures. At high temperature, with fully disordered $[NbOF_5]^{2-}$ octahedra, and sufficient thermal energy, the free energy of the CS to HT transition is reduced and the *Pbcm* and *Pnma* phases, which are locally stable variants of *Cmcm* in the *potential* energy landscape,

become unstable phases in the *free* energy landscape. Thermodynamic equilibrium requires minimization of the *free* energy. Consequently the *Cmcm* phase is made the stable bulk state as a dynamically disordered phase.

Thermally driven octahedral rotations cause the high-temperature structure to be dynamically disordered between the *Pbcm* and the *Pnma* phases. Even though the experimentally observed HT *Cmcm* structure occupies a saddle point in the potential energy landscape, because it serves as the bridge between the two locally stable polymorphs, it is stabilized at high temperature. The HT phase does not revert to the CS phase upon cooling because the CS phase is higher in energy while the system is disordered, and the energy to rearrange the cation sublattice is too high to overcome when the system is cooled enough to regain long range order. The HT to NCS transition changes the cation sublattice only slightly, and remains thermally accessible as the system cools. So the CS to HT phase transition is made favorable by octahedral disorder at elevated temperatures (~625 K). Without disorder (only present at elevated temperatures) the CS/HT transition is inaccessible, but without ordered octahedra (only possible at low temperatures), the HT phase is more stable than the CS phase. Consequently the CS to HT phase transition is irreversible and the HT phase always transforms to the NCS phase on cooling.
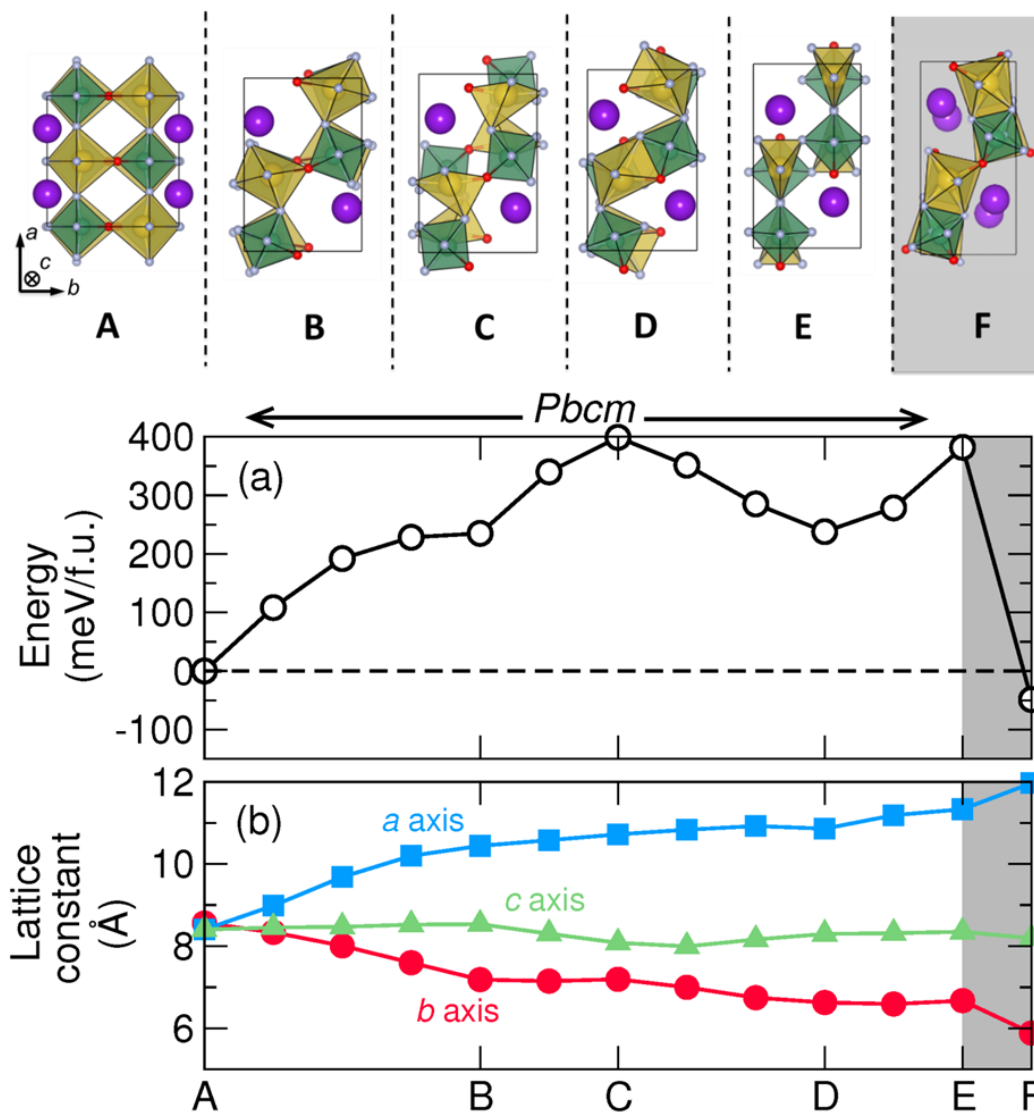
Figure 35: Properties and structure along the minimum energy phase transformation path at zero pressure. The reaction coordinate is accumulated configurational change along the path. Here the letters indicate key structures, shown above. The region shaded grey represents the reversible HT to NCS transition not investigated by the G-SSNEB.

8.4 Transition Pathway

A computational examination of the phase transition from the *P4/nmm* CS phase to a model *Cmcm* HT phase, which omits the O/F site disorder but, as will be shown, retains bond breaking effects caused by rotations of the $NbOF_5$ octahedra, was performed. We computed a hypothetical minimum energy pathway (MEP) for the transition at 0K between these two phases using the generalized solid-state nudged elastic band (G-SSNEB) method, within a constrained symmetry subspace spanned by the *Pbcm* group, a common subgroup of both space groups. The optimized MEP and structures at selected points along the transition coordinate are shown in Figure 35 along with a plot of the changes to the calculated lattice energy. There are two points on the MEP (reaction coordinates C and E) that represent energetic barriers with a magnitude of ~400 meV/f.u. above the low temperature CS phase structure (reaction coordinate A), and one of these (coordinate E) corresponds to the HT *Cmcm* structure. An intermediate energetic minimum (~200 meV/f.u.) appears at the coordinate labeled D, and that structure is very similar to the *Pbcm* structure identified from the earlier MD simulations as a candidate for the HT phase. An energetic inflection point is observed at coordinate B, and is attributed to the boundary between structures with 6-fold and 5-fold Na^+ coordination. At coordinate D, the Na^+ ions regain 6-fold coordination with a corresponding decrease in lattice energy. The energy increases again along the transition to point E (*Cmcm* structure) as the Na^+ ions again become 5-fold coordinated.
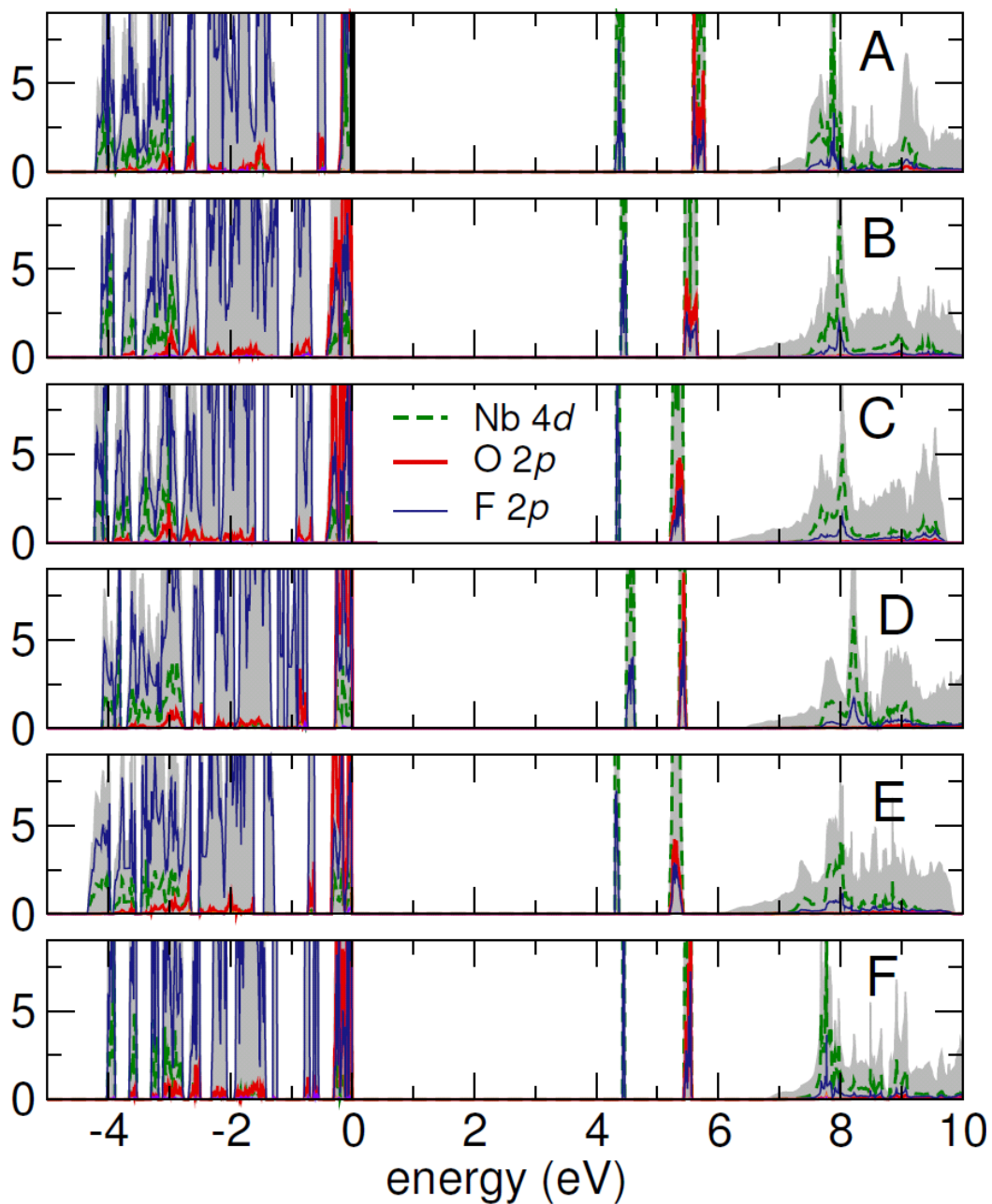
Figure 36: Atomically resolved partial density of states (DOS) plots of the transition structures along the MEP.

A close examination of the structures along the calculated MEP can aid in understanding the corresponding energies. Throughout the transformation, the Nb atoms maintain a 6-fold

octahedral coordination, the $[NbOF_5]^{2-}$ units acting like single molecule anions, attributed to the strong hybridization between the Nb $4d$ states and the ligand $2p$ states (Figure 36). The $[NbOF_5]^{2-}$ units undergo rigid 90° rotations about the c-axis with respect to the units in the neighboring plane. These rotations break some of the Na-ligand bonds, deforming the stable octahedral coordination environment of the Na^+ ion and raising the overall lattice energy. The cell parameters respond to the reconstruction, removing the tetragonal relationship observed in the $P4/nmm$ structure and becoming orthorhombic. At the highest energy structure along the transition (C), the Na coordination is 5-fold, resulting from a broken Na-F bond. Stable compounds with 5-fold Na coordination are extremely rare, so it is understandable that such a structure would be unstable. Recovery of 6-fold coordination by the Na cation through a change in connectivity between the Na and Nb coordination polyhedra from purely corner sharing to a mixture of corner and edge sharing (structure A vs structure D) occurs, which lowers the energy of the lattice, and causes structure D to represent a local energy minimum. The $Cmcm$ structure is then reached by additional Na-ligand bond breaking, giving a $KNaNbOF_5$ structure with corner connectivity unstable 5-coordinate Na cations. From A to E the b-axis contracts by ~2.68 Å while the a-axis elongates by ~3.56Å. In contrast, the c-axis is nearly unchanged, only decreasing by ~0.22Å. These lattice changes are consistent with the experimental structure evolution and also agree with the behavior observed in the MD simulation.

The most dramatic component of the phase transition is the significant restructuring of the cation lattice. We observe the K^+ cations being displaced along the a-axis in the MEP, moving away from the cell boundary and toward the $a/4$ position. The $P4/nmm$ structure includes vacant sites that are very similar to the K^+ cation sites. By shifting to the $a/4$ position, the K^+

cations and vacant sites are effectively combining, eliminating the vacant sites and increasing the packing density of the cation sublattice.

Calculated results suggest that strong covalent interactions dominate over the ionic bonds in determining the transition behavior of $KNaNbOF_5$. Strongly covalent nature of the Nb-ligand bonds, as observed throughout the MEP, supports the idea that the octahedral $[NbOF_5]^{2-}$ anions act as rigid molecular units throughout the reconstructive transition. The nearly pure ionic character of the K/Na-ligand bonds, conversely, supports the view that these are the bonds that break and reform over the course of the reconstructive transition. The MEP is an approximate description of the reconstructive transition. Owing to the first-order nature of the transition, requiring nucleation and growth of the HT phase at the expense of the CS phase, the transition most likely proceeds through a domino effect that has strong similarities to the MEP. The MEP model predicts that the *Pbcm*-type structure, independently identified by the MD simulation, is a local energetic minimum. The *Cmcm* structure, which was not found to be stable in the ab initio MEP calculation or by the empirically based MD simulation is a supergroup transition state linking the *Pbcm* and *Pnma* structures. The observed HT phase is therefore best described as a system dynamically disordered between the *Pbcm* and *Pnma* structures, and is experimentally observed as having the structure of the transition structure, the *Cmcm* phase.

8.5 Experimental Methods

8.5.1 Cryogenic Crystallography

Single crystal X-ray diffraction precession data were collected for the NCS phase of $KNaNbOF_5$. Single crystals of the NCS phase of $KNaNbOF_5$ were synthesized using a

previously reported method.[58] Cryogenic, high pressure single crystal diffraction experiments were done using a Diamond Anvil Cell (DAC) with rhenium metal gaskets and were performed at station 16-BM-D at the Advanced Photon Source (APS) at Argonne National Laboratory. A liquid helium flow was used to achieve a temperature of 15 K for all experiments. The pressure in the DAC was controlled using a dual diaphragm arrangement and monitored by in-line ruby fluorescence. Experimental pressures ranged from 1-10 GPA. Diffraction patterns were collected on a MAR 345 CCD plate detector. Neon gas was used as the pressure medium and diffraction rings from its crystalline phase can be observed in the collected data. Single crystal DAC data processing was performed using the GSE_ADA software package and refined using SHELXL.[232,233]

8.5.2 Molecular Dynamics

MD simulations for this project were performed using a purpose-made script written in Mathematica 9. The MD system comprised a pseudo-isothermal-isobaric (NPT) ensemble in which the calculated temperature and internal pressure were fractionally adjusted toward set values with each time step. Internal temperature was calculated from the kinetic energy of the simulated atoms and pressure was calculated as a sum of contributions from each pair interaction. The supercell angles were fixed at 90º, but each dimension was allowed to change dynamically to adjust the internal pressures by a method analogous to that of Parrinello and Rahman.[223] Our simulation also introduced very small, randomized, fluctuations in atomic momentum vectors intended to mimic radiative thermal energy exchange between ions, and accelerate phase space exploration.

KNaNbOF$_5$ is an ionic system. Pairwise interatomic interaction functions can reasonably be applied to dynamic simulations of ionic systems because electrons are primarily localized around individual atoms.[27] We fit an empirical set of pair interaction functions for the KNaNbOF$_5$ system to apply to our MD simulation. We used a multiple power law form for our pair interaction functions, and the force form is given as equation 1.

$$F(r_{ij}) = k_e \frac{q_i * q_j}{r_{ij}^2} + \frac{A_{ij}}{r_{ij}^4} + \frac{B_{ij}}{r_{ij}^6} + \frac{C_{ij}}{r_{ij}^8} + \frac{D_{ij}}{r_{ij}^{10}}$$

eqn. 10

In **eqn. 10** r_{ij} is the interatomic distance between the i_{th} and the j_{th} ions, k_e is Coulomb's constant (14.39964 V^{2}Å eV^{-1}), and the q terms are the nominal ionic charges for the two ions. The A, B, C, and D terms are the empirical pair function parameters specific to the ion types for i and j. The first part of this equation is the coulomb contribution to the pair interaction, and the four other terms are the fitted portion. The fitted sections are purely empirical and are not intended to individually represent specific physical contributions to the interaction. A table of the numerical values of the empirical constants, A, B, C, and D, for each of the 15 pair interaction types is available in Table 6.

To increase the predictive range of our pair functions we fit their empirical parameters to experimental single crystal structures collected over a range of pressures and exclusively at cryogenic temperatures. We incorporated structure data obtained using DAC variable-pressure, cryogenic diffraction measurements, on a sample of the NCS phase of KNaNbOF$_5$. The pair interaction functions were optimized to reproduce, as closely as possible, the atom positions and

internal pressures for each experimental structure. Low temperature (≤ 100 K) data was used to minimize the impact of thermal vibrations on observed atomic positions and lattice constants.

Our MD simulation of the $KNaNbOF_5$ system started as a $\sqrt{2}$ x $\sqrt{2}$ x 2 CS phase supercell. The cell axes of the orthorhombic HT and NCS phases are oriented at an angle of 45 degrees with respect to the two a-axes in the tetragonal CS phase. The $\sqrt{2}$ x $\sqrt{2}$ x 2 transformation gives the supercell lattice an orientation that allows it to represent both CS and NCS phases, and was used for that reason. The simulation temperature was held constant at 350 °C. Pathways for reconstructive phase transitions often occur by nucleation at crystal surface structures, grain boundaries, or site defects. Consequently, MD simulations of reconstructive transitions in a bulk material often involve very high activation energies compared to experimental observations. To accelerate the CS to HT transition in our simulation of $KNaNbOF_5$ we found it necessary to restrict changes in two of the supercell dimensions to be unidirectional (though not driven) until the system had passed the kinetic transition barrier and would not immediately return to the CS phase configuration. After the simulation passed this threshold (at ~3500 fs), these restraints on the supercell were removed.

Table 6: Empirical parameters used with eqn. 10 & eqn. 11 for calculating pairwise interatomic forces.

Pair #	i	j	q_i*q_j	A	B	C	D
1	K	K	1	113.57	-3301	-20372	747183
2	K	Na	1	-125.83	3429	-60596	930669
3	K	Nb	5	-1064.38	27390	-366343	2199599
4	K	O	-2	-271.73	5327	-26612	70572
5	K	F	-1	-12.85	-1556	10213	31616
6	Na	Na	1	89.12	-3122	-40788	630055
7	Na	Nb	5	29.09	-4587	20250	500820
8	Na	O	-2	38.24	-822	4625	12704
9	Na	F	-1	97.23	-1437	-2919	42755
10	Nb	Nb	25	-1289.08	26925	-206327	2329999
11	Nb	O	-10	-11.57	514	2244	433
12	Nb	F	-5	-580.28	5308	-11384	8803
13	O	O	4	-389.35	11910	-102958	510556
14	O	F	2	-150.16	4977	-62724	329822
15	F	F	1	-58.68	2260	-9353	42236

To account for force contributions from the extended structure, we employed the Wolf summation method.[217] The Wolf summation method is less computationally expensive than the Ewald method for calculating the contributions from the extended structure using periodic boundary conditions, and has been shown to give similar results when the cutoff radius is set sufficiently high.[218] We used the Wolf summation method when fitting pair interaction function parameters as well as in the MD simulations. Each power law component of the force function

used in our MD simulation was converted in a manner analogous to that used to derive the Wolf summation formulation for the Coulomb component. The function used in our fitting process and in our simulation to calculate the pairwise interatomic forces with the parameter values in Table 6 is given in eqn. 11.

$$F_{ij}(r, \alpha, R_c) =$$

$$k_c * q_i * q_j * \left[\left(\frac{2 * \alpha * e^{(-\alpha^2 * r^2)}}{\sqrt{\pi} * r} + \frac{Erfc(\alpha * r)}{r^2} \right) - \left(\frac{2 * \alpha * e^{(-\alpha^2 * R_c^2)}}{\sqrt{\pi} * R_c} + \frac{Erfc(\alpha * R_c)}{R_c^2} \right) \right] +$$

$$\frac{A_{ij}}{3} * \left[\left(\frac{2 * \alpha * e^{(-\alpha^2 * r^2)}}{\sqrt{\pi} * r^3} + \frac{3 * Erfc(\alpha * r)}{r^4} \right) - \left(\frac{2 * \alpha * e^{(-\alpha^2 * R_c^2)}}{\sqrt{\pi} * R_c^3} + \frac{3 * Erfc(\alpha * R_c)}{R_c^4} \right) \right] +$$

$$\frac{B_{ij}}{5} * \left[\left(\frac{2 * \alpha * e^{(-\alpha^2 * r^2)}}{\sqrt{\pi} * r^5} + \frac{5 * Erfc(\alpha * r)}{r^6} \right) - \left(\frac{2 * \alpha * e^{(-\alpha^2 * R_c^2)}}{\sqrt{\pi} * R_c^5} + \frac{5 * Erfc(\alpha * R_c)}{R_c^6} \right) \right] +$$

$$\frac{C_{ij}}{7} * \left[\left(\frac{2 * \alpha * e^{(-\alpha^2 * r^2)}}{\sqrt{\pi} * r^7} + \frac{7 * Erfc(\alpha * r)}{r^8} \right) - \left(\frac{2 * \alpha * e^{(-\alpha^2 * R_c^2)}}{\sqrt{\pi} * R_c^7} + \frac{7 * Erfc(\alpha * R_c)}{R_c^8} \right) \right] +$$

$$\frac{D_{ij}}{9} * \left[\left(\frac{2 * \alpha * e^{(-\alpha^2 * r^2)}}{\sqrt{\pi} * r^9} + \frac{9 * Erfc(\alpha * r)}{r^{10}} \right) - \left(\frac{2 * \alpha * e^{(-\alpha^2 * R_c^2)}}{\sqrt{\pi} * R_c^9} + \frac{9 * Erfc(\alpha * R_c)}{R_c^{10}} \right) \right]$$

eqn. 11

In eqn. 11 F_{ij} is the force between atom types i & j, r is the distance between atoms i & j, α is the convergence parameter (0.185 used), R_c is the cutoff radius (18Å used), k_c is Coulomb's constant ($k_c=1/(4*\pi*\varepsilon_0)$), and $Erfc(x)$ is the complementary error function of x.

8.5.3 DFT Methods

To investigate the energetics of the reaction pathway in $KNaNbOF_5$ we employ the generalized solid-state nudged elastic band (G-SSNEB).[234] The forces and stresses are evaluated with density functional theory (DFT) calculations in the general gradient approximation (GGA) of Perdew-Burke-Ernzerhof revised for solids,[235] (PBEsol) as implemented in the Vienna Ab Initio Simulation Package (VASP),[236,237] with the projector augmented wave (PAW) method,[238] to treat the core and valence electrons using the following valence configurations: $3s^2 3p^6 4s^1$ for K, $2p^6 3s^1$ for Na, $4p^6 5s^1 4d^4$ for Nb, $2s^2 2p^4$ for O, and $2s^2 2p^5$ for F. We use a 5 x 5 x 5 Monkhorst-Pack k-point mesh,[239] with Gaussian smearing (10 meV width) for Brillouin zone (BZ) integrations and a 500 eV plane wave cutoff. Structural relaxations are performed until the Hellmann-Feynman forces are less than 10meV $Å^{-1}$ on each atom. The free energy values were derived from the phonon vibrational frequencies using the PHONOPY package.[240]

8.6 Conclusions

Combining the results from empirically-based MD simulations and ab initio DFT methods to investigate a reconstructive phase transition in $KNaNbOF_5$, we successfully identified the symmetry and structure of the previously unsolved high temperature phase. It was found that the high temperature phase is structurally complicated, with a structure that is likely produced by a dynamic disorder across two different structures with nearly identical cation sublattices, but different dipole orientations of the $[NbOF_5]^{2-}$ octahedral units. A quantitative minimum energy pathway for the transition at 0K was calculated using ab initio methods, and a qualitative phenomenological model that identifies a driving force the reconstructive transition and explains it as involving both displacive and order-disorder components was proposed. The

displacive component of the reconstructive transition is made energetically favorable by an order-disorder transition involving the orientations of the dipole moments belonging to the octahedral $[NbOF_5]^{2-}$ units. These units act as rigid molecules, and disordering of O and F sites arises when the individual units experience "hopping" type rotation events that change the direction of the Nb-O bond. In the *P4/nmm* starting phase, the resulting disorder destabilizes the distribution of the K^+ and vacant sites, providing the driving force for the displacive part of the reconstructive phase transition.

The reconstructive transition in $KNaNbOF_5$ results from the presence of vacant sites in the cation lattice of the starting phase. While disordering of the polar, heteroanionic units plays an important role, similar behavior in related compounds with fully occupied cation lattices do not exhibit reconstructive transitions. The presence of dipole units that stabilize an ordered distribution of vacant and occupied cation sites, along with the accessibility of an order-disorder transition involving those dipole units, are both necessary for the reconstructive transition observed in this system. Reconstructive transitions should be observed in related compounds that possess these same components. Two specific candidates, $KNaWO_2F_4$ and $KNaMoO_2F_4$, have been synthesized hydrothermally and are reported to crystallize in the space group *P4/nmm*.[57] Based on the results discussed here, it is considered likely that both of these phases should undergo thermally induced irreversible reconstructive phase transitions but at a somewhat higher temperature than the transition observed in $KNaNbOF_5$, and should, on cooling, adopt phases that have not yet been reported for these compounds. The approach used here, combining detailed experimental investigation, empirically based computational methods, and ab initio analytical investigations, can provide new insights into phase transitions in other heteroanionic

solid state systems. This method can enable researchers to develop a detailed understanding of dynamic mechanisms that lead systems to adopt specific structures, and will aid in the development of advanced computational methods that will someday be able to predict the synthetic conditions necessary to produce useful and previously undiscovered solid state phases.

Chapter 9

9.1 Conclusions and Future Directions

Efforts to develop methods that would allow truly directed synthetic inorganic chemistry for discovery of new, noncentrosymmetric crystal phases have, in recent decades, focused on the incorporation of polar anionic building units.[1-6] This concept takes advantage of a tendency for dipoles to adopt long-range order in crystal lattices and increases the probability that a new phase will have polar symmetry. Recently, an extension to this concept has been developed that involves using Λ-shaped, polar units that promote alignment through steric ordering effects as well as through dipole interactions.[7,8]

Improvements to our understanding of those influences that stabilize formation of noncentrosymmetric crystal phases would contribute to the development of additional strategies. One way to achieve this understanding would be to observe the atom-scale dynamic processes of crystal formation from solution and in the solid state for both centrosymmetric and noncentrosymmetric phases. Direct observation of these processes by experimental methods (such as in situ pair distribution function analysis) can only be done with a lower level of resolution than is desirable. Consequently, the most promising techniques for investigating atom-scale crystal formation involve using computational models to generate dynamic simulations.[9-11]

A major challenge in the development of computational methods to reliably simulate dynamic behavior of atomistic systems is constructing models that are able to *accurately* predict the potential energy surfaces of the systems in question.[12] Models are either based on ab initio calculations, experimental measurements, or a combination of the two. Ab initio-based models

lack precision and empirically-based models lack transferability.[13,14] In the work presented here on the phase transition in $KNaNbOF_5$ it was shown that it is possible, at least in some cases, to develop empirical models that have reasonably good transferability, and can be applied to closely approximate phase transition behavior.[15] The empirical-type model used for that work was parameterized by fitting against diffraction measurements of the pressure/structure behavior of one phase of this system at cryogenic conditions (T = 15K) using a diamond anvil cell. This model was successfully used to discover the crystal structure of the previously unsolved high temperature (T ≈ 625K) phase, confirmed by matching simulated and experimental powder diffraction patterns.

At finite temperatures, systems in equilibrium adopt configurations that minimize their free energy. Free energy surfaces are different from the potential energy surfaces, as the free energy includes kinetic and entropic contributions. The difference between a minimized free energy crystal structure and the corresponding minimized potential energy crystal structure increases with temperature. The ability to parameterize empirical models and the ability to evaluate the predictive accuracy of ab initio models both require detailed experimental determinations of crystal structures in minimized potential energy conditions.[12,16] Thermal energy influences observed bond distances, and there is some evidence in the literature that experimental bond lengths in at least some crystal systems respond in nonlinear ways to small changes in temperature.

Further experimental evidence is needed to confirm the existence of nonlinear relationships between temperature and atomic positions in low symmetry crystal systems. This would involve collecting single crystal structure data for a sample multiple times under a small

range of temperatures. The noncentrosymmetric phase of $KNaNbOF_5$ could be used as a test case for this. One possible explanation for such an effect is that the shifts in bond lengths correspond to changes in relative populations of various acoustic phonon modes.

The conclusions about the origin of the noncentrosymmetric character in the $Pna2_1$ phase of $KNaNbOF_5$ should be tested by investigating the related compounds $KNaMoO_2F_4$ and $KNaWO_2F_4$.[17] These two compounds have been synthesized hydrothermally crystallizing in the $P4/nmm$ space group, the same space group as the centrosymmetric phase of $KNaNbOF_5$. The two related compounds are expected to exhibit similar phase transition behavior, although they are also expected to transition at a higher temperature than $KNaNbOF_5$.

Future progress in the development and application of cryogenic empirical interatomic potentials will involve using them to simulate additional solid-solid phase transitions, and eventually simulating a solid-state synthetic reaction. In the research into the phase transition of $KNaNbOF_5$ the potential functions developed from the acentric phase at low temperatures were able to predict the behavior of the structure at elevated temperature. The next step is to evaluate the versatility of the pair potentials developed for the $KNaNbOF_5$ investigation by using them to simulate the well-studied phase transition behavior of the ferroelectric compound $KNbO_3$.

$KNbO_3$ is a good system to examine next, because it undergoes 3 reversible phase transitions at well-known temperatures. Pair potential functions will need to be accurate over a broad range of conditions in order to predict each transition at the appropriate temperature. The stoichiometry of the system also makes it a good candidate for molecular dynamics simulations. If the pairwise potential functions from the $KNaNbOF_5$ research fail to reproduce the structures

and behavior of $KNbO_3$, a new set of interatomic interaction functions able to reproduce the behavior of both systems would need to be developed.

Once a set of potential functions has been developed that reproduces the structure behavior of several different compounds reliably, the next step will be to simulate melting of at least one of the compounds. Accurate prediction of melting points using potentials developed from cryogenic data would demonstrate broad versatility, and lead into the next stage of this work.

A dynamic simulation of a solid state synthesis reaction will be a challenge. It will require a very large simulation supercell with several different crystalline phases present as isolated sections. Large supercell simulations require a great deal of computing power to perform, amplifying the negative impact of any mistakes in setting up the reaction. Diffusion of atoms in solid state synthesis can take a long time and may become a major hurdle for the simulation. Another challenge will involve identification of product crystal domains within the simulation, which may form as a polycrystalline sample, even on the scale of a simulation. One way that this last challenge might be addressed is to use pair distribution analysis, which is independent of relative orientation. Simulating a solid state synthetic reaction from starting materials successfully would prove that real predictions can be made using cryogenic structure data to develop empirical structure interatomic potential functions for discovering synthetic methods of making new inorganic compounds.

References

Chapter 1 References

(1)   Fedorov, E. *Zap. Mineralog. Obsc.(2)* **1891**, *28*, 1.

(2)   Halasyamani, P. S.; Poeppelmeier, K. R. *Chemistry of Materials* **1998**, *10*, 2753.

(3)   Hollingsworth, M. D. *Science* **2002**, *295*, 2410.

(4)   Glazer, A.; Stadnicka, K. *Acta Crystallographica Section A: Foundations of Crystallography* **1989**, *45*, 234.

(5)   Valasek, J. *Physical review* **1921**, *17*, 475.

(6)   Rieckhoff, K. E.; Peticolas, W. L. *Science* **1965**, *147*, 610.

(7)   Franken, P.; Hill, A. E.; Peters, C.; Weinreich, G. *Physical Review Letters* **1961**, *7*, 118.

(8)   Kurtz, S.; Perry, T. *Journal of Applied Physics* **1968**, *39*, 3798.

(9)   Zyss, J.; Oudar, J. *Physical Review A* **1982**, *26*, 2028.

(10)   Scott, J. *Nature materials* **2007**, *6*, 256.

(11)   Cho, Y.; Fujimoto, K.; Hiranaga, Y.; Wagatsuma, Y.; Onoe, A.; Terabe, K.; Kitamura, K. *Applied physics letters* **2002**, *81*, 4401.

(12)   Dosch, J. J.; Inman, D. J.; Garcia, E. *Journal of Intelligent Material Systems and Structures* **1992**, *3*, 166.

(13)   Wu, C.; Kahn, M.; Moy, W. *Journal of the American Ceramic Society* **1996**, *79*, 809.

(14)   Becker, P. *Advanced Materials* **1998**, *10*, 979.

(15)   Chen, C.; Wu, Y.; Li, R. *Journal of Crystal growth* **1990**, *99*, 790.

(16)   Yokotani, A.; Sasaki, T.; Yoshida, K.; Nakai, S. *Applied physics letters* **1989**, *55*, 2692.

(17)   Buscaglia, M. T.; Bassoli, M.; Buscaglia, V.; Alessio, R. *Journal of the American Ceramic Society* **2005**, *88*, 2374.

(18)   Li, J.; Jin, Y.-L.; Zhang, X.-G.; Yang, H. *Solid State Ionics* **2007**, *178*, 1590.

(19)   Lundblad, A.; Bergman, B. *Solid State Ionics* **1997**, *96*, 173.

(20)   Bunsen, R. *Justus Liebigs Annalen der Chemie* **1848**, *65*, 70.

(21)   von Schafhäutl, K. E. *Gelehrte Anzeigen* **1845**, *20*, 561.

(22)   McWhan, D. *Sand and Silicon: Science that Changed the World*; OUP Oxford: New York, USA, 2012.

(23)   Harrison, W. T.; Nenoff, T. M.; Gier, T. E.; Stucky, G. D. *Inorganic Chemistry* **1993**, *32*, 2437.

(24)   Norquist, A. J.; Heier, K. R.; Stern, C. L.; Poeppelmeier, K. R. *Inorganic chemistry* **1998**, *37*, 6495.

(25)   Donakowski, M. D.; Vinokur, A. I.; Poeppelmeier, K. R. *Zeitschrift für anorganische und allgemeine Chemie* **2012**, *638*, 1991.

(26)   Donakowski, M. D.; Gautier, R.; Yeon, J.; Moore, D. T.; Nino, J. C.; Halasyamani, P. S.; Poeppelmeier, K. R. *Journal of the American Chemical Society* **2012**, *134*, 7679.

(27)   Agulyansky, A. *Chemistry of tantalum and niobium fluoride compounds*; Elsevier: Amsterdam, The Netherlands, 2004.

(28)   Welk, M. E.; Norquist, A. J.; Arnold, F. P.; Stern, C. L.; Poeppelmeier, K. R. *Inorganic chemistry* **2002**, *41*, 5119.

(29)   Maggard, P. A.; Stern, C. L.; Poeppelmeier, K. R. *Journal of the American Chemical Society* **2001**, *123*, 7742.

(30)   Mori, Y.; Kuroda, I.; Nakajima, S.; Sasaki, T.; Nakai, S. *Applied physics letters* **1995**, *67*, 1818.

(31)   Wu, Y.; Sasaki, T.; Nakai, S.; Yokotani, A.; Tang, H.; Chen, C. *Applied physics letters* **1993**, *62*, 2614.

(32)   Chen, C.; Wang, Y.; Wu, B.; Wu, K.; Zeng, W.; Yu, L. *Nature* **1995**, *373*, 322.

(33)   Hu, Z.-G.; Yoshimura, M.; Mori, Y.; Sasaki, T. *Journal of crystal growth* **2004**, *260*, 287.

(34)   Chen, C.; Wang, G.; Wang, X.; Xu, Z. *Applied Physics B* **2009**, *97*, 9.

(35)   Isaenko, L.; Krinitsin, P.; Vedenyapin, V.; Yelisseyev, A.; Merkulov, A.; Zondy, J.-J.; Petrov, V. *Crystal growth & design* **2005**, *5*, 1325.

(36)   Woodley, S. M.; Catlow, R. *Nature materials* **2008**, *7*, 937.

(37)   Oganov, A. R.; Glass, C. W. *The Journal of chemical physics* **2006**, *124*, 244704.

(38)   Dunitz, J. D. *Chemical Communications* **2003**, 545.

(39)   Raccuglia, P.; Elbert, K. C.; Adler, P. D.; Falk, C.; Wenny, M. B.; Mollo, A.; Zeller, M.; Friedler, S. A.; Schrier, J.; Norquist, A. J. *Nature* **2016**, *533*, 73.

(40)   Gautier, R.; Zhang, X.; Hu, L.; Yu, L.; Lin, Y.; Sunde, T. O.; Chon, D.; Poeppelmeier, K. R.; Zunger, A. *Nature chemistry* **2015**, *7*, 308.

(41)   Zhang, X.; Yu, L.; Zakutayev, A.; Zunger, A. *Advanced Functional Materials* **2012**, *22*, 1425.

(42)   Chen, C.-T. *Acta Physica Sinica* **1977**, *26*, 124.

(43)   Chuangtian, C. *Scientia Sinica* **1979**, *22*, 756.

(44)   Chen, C.-t.; Liu, G.-z. *Annual Review of Materials Science* **1986**, *16*, 203.

(45)   Ye, N.; Chen, Q.; Wu, B.; Chen, C. *Journal of applied physics* **1998**, *84*, 555.

(46)   Wu, H.; Yu, H.; Pan, S.; Huang, Z.; Yang, Z.; Su, X.; Poeppelmeier, K. R. *Angewandte Chemie International Edition* **2013**, *52*, 3406.

(47)   Chen, C.; Lin, Z.; Wang, Z. *Applied Physics B* **2005**, *80*, 1.

(48)   Wu, H.; Yu, H.; Yang, Z.; Hou, X.; Su, X.; Pan, S.; Poeppelmeier, K. R.; Rondinelli, J. M. *Journal of the American Chemical Society* **2013**, *135*, 4215.

(49)   Wu, H.; Pan, S.; Poeppelmeier, K. R.; Li, H.; Jia, D.; Chen, Z.; Fan, X.; Yang, Y.; Rondinelli, J. M.; Luo, H. *Journal of the American Chemical Society* **2011**, *133*, 7786.

(50)   Fan, X.; Pan, S.; Hou, X.; Tian, X.; Han, J.; Haag, J.; Poeppelmeier, K. R. *Crystal Growth & Design* **2009**, *10*, 252.

(51)   Yu, N.; Wang, S.; Ye, N.; Liang, F.; Lin, Z.; Luo, M.; Poeppelmeier, K. R. *Chemistry of Materials* **2016**.

(52)   Pan, S.; Smit, J. P.; Watkins, B.; Marvel, M. R.; Stern, C. L.; Poeppelmeier, K. R. *Journal of the American Chemical Society* **2006**, *128*, 11631.

(53)   Wu, L.; Chen, X.; Xu, Y.; Sun, Y. *Inorganic chemistry* **2006**, *45*, 3042.

(54)   Zhang, M.; Pan, S.-L.; Fan, X.-Y.; Zhou, Z.-X.; Poeppelmeier, K. R.; Yang, Y. *CrystEngComm* **2011**, *13*, 2899.

(55)   Becker, P. *Advanced Materials (Weinheim, Germany)* **1998**, *10*, 979.

(56)   Gautier, R.; Donakowski, M. D.; Poeppelmeier, K. R. *Journal of Solid State Chemistry* **2012**, *195*, 132.

(57)   Pinlac, R. A. F.; Stern, C. L.; Poeppelmeier, K. R. *Crystals* **2011**, *1*, 3.

(58)   Chang, K. B.; Vinokur, A.; Pinlac, R. A. F.; Suchomel, M. R.; Marvel, M. R.; Poeppelmeier, K. R. *Inorg. Chem.* **2014**, *53*, 6979.

(59)   Maggard, P. A.; Nault, T. S.; Stern, C. L.; Poeppelmeier, K. R. *Journal of Solid State Chemistry* **2003**, *175*, 27.

(60)   Gautier, R.; Poeppelmeier, K. R. *Inorganic chemistry* **2012**, *51*, 10613.

(61)   Chen, C.; Wu, Y.; Li, R. *International Reviews in Physical Chemistry* **1989**, *8*, 65.

(62)   Pearson, R. G. *Proceedings of the National Academy of Sciences* **1975**, *72*, 2104.

(63)   Goodenough, J. *Annual review of materials science* **1998**, *28*, 1.

(64)   Burns, G.; Scott, B. A. *Physical Review B* **1973**, *7*, 3088.

(65)   Lambeck, P.; Jonker, G. *Journal of Physics and Chemistry of Solids* **1986**, *47*, 453.

(66)   Nambu, S.; Sagala, D. A. *Physical Review B* **1994**, *50*, 5838.

(67)   Stokes, H. T.; Kisi, E. H.; Hatch, D. M.; Howard, C. J. *Acta Crystallographica Section B: Structural Science* **2002**, *58*, 934.

(68)   Bhattacharya, K.; Ravichandran, G. *Acta Materialia* **2003**, *51*, 5941.

(69)   Resta, R.; Posternak, M.; Baldereschi, A. *Physical review letters* **1993**, *70*, 1010.

(70)   Marvel, M. R.; Lesage, J.; Baek, J.; Halasyamani, P. S.; Stern, C. L.; Poeppelmeier, K. R. *J. Am. Chem. Soc.* **2007**, *129*, 13963.

(71)   Heier, K. R.; Norquist, A. J.; Halasyamani, P. S.; Duarte, A.; Stern, C. L.; Poeppelmeier, K. R. *Inorganic Chemistry* **1999**, *38*, 762.

(72)   Norquist, A. J.; Stern, C. L.; Poeppelmeier, K. R. *Inorganic chemistry* **1999**, *38*, 3448.

(73)   Welk, M. E.; Norquist, A. J.; Stern, C. L.; Poeppelmeier, K. R. *Inorganic Chemistry* **2001**, *40*, 5479.

(74)   Gautier, R.; Gautier, R. g.; Chang, K. B.; Poeppelmeier, K. R. *Inorganic chemistry* **2015**, *54*, 1712.

(75)   Pakhomov, V.; RL, D.; TA, K.; TF, L. *ZHURNAL NEORGANICHESKOI KHIMII* **1973**, *18*, 1240.

(76)   Holland, M.; Donakowski, M. D.; Pozzi, E. A.; Rasmussen, A. M.; Tran, T. T.; Pease-Dodson, S. E.; Halasyamani, P. S.; Seideman, T.; Van Duyne, R. P.; Poeppelmeier, K. R. *Inorganic chemistry* **2013**, *53*, 221.

(77)   Yamamoto, H.; Katogi, S.; Watanabe, T.; Sato, H.; Miyata, S.; Hosomi, T. *Applied physics letters* **1992**, *60*, 935.

(78)   Needs, R. L.; Weller, M. T. *Journal of the Chemical Society, Dalton Transactions* **1995**, 3015.

(79)   Withers, R.; Welberry, T.; Brink, F.; Norén, L. *Journal of Solid State Chemistry* **2003**, *170*, 211.

(80)   Molokeev, M.; Fokina, V.; Kocharova, A.; Aleksandrov, K. *Physics of the Solid State* **2011**, *53*, 834.

(81)   Donakowski, M. D.; Görne, A.; Vaughey, J. T.; Poeppelmeier, K. R. *Journal of the American Chemical Society* **2013**, *135*, 9898.

(82)   Zeng, D.; Cabana, J.; Bréger, J.; Yoon, W.-S.; Grey, C. P. *Chemistry of Materials* **2007**, *19*, 6277.

Chapter 2 References

(1)   Brown, I. *Structure and bonding in crystals* **1981**, *2*, 1.

(2)   Brown, I. D.; Poeppelmeier, K. R. *Bond valences*; Springer, 2014.

(3)   Brown, I.; Altermatt, D. *Acta Crystallographica Section B: Structural Science* **1985**, *41*, 244.

(4)   Brese, N. E.; O'Keeffe, M. *Acta Crystallographica Section B* **1991**, *47*, 192.

(5)   Pauling, L. *J. Am. Chem. Soc.* **1929**, *51*, 1010.

(6)   Brown, I. D. 2012.

(7)   Mayer, I. *Chemical Physics Letters* **1983**, *97*, 270.

(8)   Salinas-Sanchez, A.; Garcia-Munoz, J.; Rodriguez-Carvajal, J.; Saez-Puche, R.; Martinez, J. *Journal of Solid State Chemistry* **1992**, *100*, 201.

(9)   Shin, Y.-H.; Cooper, V. R.; Grinberg, I.; Rappe, A. M. *Physical Review B* **2005**, *71*, 054104.

(10)   Lufaso, M. W.; Woodward, P. M. *Acta Crystallographica Section B: Structural Science* **2001**, *57*, 725.

(11)   Marvel, M. R.; Lesage, J.; Baek, J.; Halasyamani, P. S.; Stern, C. L.; Poeppelmeier, K. R. *J. Am. Chem. Soc.* **2007**, *129*, 13963.

(12)   Holland, M.; Donakowski, M. D.; Pozzi, E. A.; Rasmussen, A. M.; Tran, T. T.; Pease-Dodson, S. E.; Halasyamani, P. S.; Seideman, T.; Van Duyne, R. P.; Poeppelmeier, K. R. *Inorganic chemistry* **2013**, *53*, 221.

(13)   Maggard, P. A.; Nault, T. S.; Stern, C. L.; Poeppelmeier, K. R. *Journal of Solid State Chemistry* **2003**, *175*, 27.

(14)   Welk, M. E.; Norquist, A. J.; Stern, C. L.; Poeppelmeier, K. R. *Inorganic chemistry* **2000**, *39*, 3946.

(15)   Welk, M. E.; Norquist, A. J.; Arnold, F. P.; Stern, C. L.; Poeppelmeier, K. R. *Inorganic chemistry* **2002**, *41*, 5119.

(16)   Adams, S. *Solid State Ionics* **2006**, *177*, 1625.

(17)   Adams, S.; Rao, R. P. *physica status solidi (a)* **2011**, *208*, 1746.

(18)   Rao, G.; Sun, J.; Liang, J.; Zhou, W. *Physical Review B* **1997**, *55*, 3742.

(19)   Glazer, A. *Acta Crystallographica Section B: Structural Crystallography and Crystal Chemistry* **1972**, *28*, 3384.

(20)   Wells, A. *Acta Crystallographica* **1954**, *7*, 535.

(21)   Jin, W.; Yeh, P.-C.; Zaki, N.; Zhang, D.; Sadowski, J. T.; Al-Mahboob, A.; van Der Zande, A. M.; Chenet, D. A.; Dadap, J. I.; Herman, I. P. *Physical review letters* **2013**, *111*, 106801.

(22)   Mahatha, S.; Patel, K.; Menon, K. S. *Journal of Physics: Condensed Matter* **2012**, *24*, 475504.

(23)   Dovesi, R.; Orlando, R.; Erba, A.; Zicovich-Wilson, C. M.; Civalleri, B.; Casassa, S.; Maschio, L.; Ferrabone, M.; De La Pierre, M.; D'Arco, P. *International Journal of Quantum Chemistry* **2014**, *114*, 1287.

(24)   Hao, P.; Fang, Y.; Sun, J.; Csonka, G. I.; Philipsen, P. H.; Perdew, J. P. *Physical Review B* **2012**, *85*, 014111.

(25)   Zhang, X.; Yu, L.; Zakutayev, A.; Zunger, A. *Advanced Functional Materials* **2012**, *22*, 1425.

(26)   Gautier, R.; Zhang, X.; Hu, L.; Yu, L.; Lin, Y.; Sunde, T. O.; Chon, D.; Poeppelmeier, K. R.; Zunger, A. *Nature chemistry* **2015**, *7*, 308.

(27)   Kamali, K.; Ravindran, T.; Ravi, C. *Spectrochimica Acta Part A: Molecular and Biomolecular Spectroscopy* **2016**, *155*, 38.

(28)   Gale, J. D. In *Handbook of Materials Modeling*; Springer: 2005, p 479.

(29)   Gale, J. D.; Rohl, A. L. *Molecular Simulation* **2003**, *29*, 291.

(30)   Wang, C.; Chan, C. T.; Ho, K. *Physical Review B* **1989**, *39*, 8586.

(31)   Phillips, J. C.; Braun, R.; Wang, W.; Gumbart, J.; Tajkhorshid, E.; Villa, E.; Chipot, C.; Skeel, R. D.; Kale, L.; Schulten, K. *Journal of computational chemistry* **2005**, *26*, 1781.

(32)   Schaible, M. *Critical reviews in solid state and materials sciences* **1999**, *24*, 265.

(33)   Gale, J. D. *Philosophical Magazine B* **1996**, *73*, 3.

(34)   Duane, S.; Kennedy, A. D.; Pendleton, B. J.; Roweth, D. *Physics letters B* **1987**, *195*, 216.

(35)   Okamoto, Y. *Journal of Molecular Graphics and Modelling* **2004**, *22*, 425.

(36)   Tuckerman, M. E.; Berne, B. J.; Martyna, G. J.; Klein, M. L. *The Journal of Chemical Physics* **1993**, *99*, 2796.

(37)   Car, R.; Parrinello, M. *Physical review letters* **1985**, *55*, 2471.

(38)   Louis, A. *Journal of Physics: Condensed Matter* **2002**, *14*, 9187.

(39)   Stoneham, A.; Harding, J. *Annual Review of Physical Chemistry* **1986**, *37*, 53.

(40)   Swamy, V.; Gale, J. D. *Physical Review B* **2000**, *62*, 5406.

(41)   Grünwald, M.; Zayak, A.; Neaton, J. B.; Geissler, P. L.; Rabani, E. *The Journal of chemical physics* **2012**, *136*, 234111.

Chapter 3 References

(1)   Kaidalova, T. A. P., V. I.; Panin, E. S. *Koordinatsionnaya Khimiya* **1976**, *2*.

(2)   Mattes, R.; Mennemann, K.; Jäckel, N.; Rieskamp, H.; Brockmeyer, H.-J. *Journal of the Less Common Metals* **1980**, *76*, 199.

(3)   Marvel, M. R. Doctoral, Northwestern University, 2008.

(4)   Udovenko, A. A.; Laptash, N. M. *Acta Crystallogr., Sect. B: Struct. Sci* **2012**, *68*, 602.   (5)   Urusov, V. S. *Zeitschrift für Kristallographie/International journal for structural, physical, and chemical aspects of crystalline materials* **2003**, *218*, 709.

(6)   Okazaki, A.; Suemune, Y. *J. Phys. Soc. Jpn.* **1961**, *16*, 671.

(7)   Tanaka, K.; Konishi, M.; Marumo, F. *Acta Crystallographica Section B: Structural Crystallography and Crystal Chemistry* **1979**, *35*, 1303.

(8)   Grabau, M. *Journal of Applied Physics* **1938**, *9*, 215.

(9)   von Schafhäutl, K. E. *Gelehrte Anzeigen* **1845**, *20*, 561.

(10)   Knowles, K. M. **2009**.

(11)   Halasymani, P. S.; Heier, K. R.; Norquist, A. J.; Stern, C. L.; Poeppelmeier, K. R. *Inorg. Chem.* **1998**, *37*, 369.

(12)   Harrison, W. T.; Nenoff, T. M.; Gier, T. E.; Stucky, G. D. *Inorg. Chem.* **1993**, *32*, 2437.

(13)   Norquist, A. J.; Heier, K. R.; Stern, C. L.; Poeppelmeier, K. R. *Inorg. Chem.* **1998**, *37*, 6495.

(14)   Bertolini, J. C. *The Journal of emergency medicine* **1992**, *10*, 163.

(15)   Segal, E. B. *Chemical Health and Safety* **2000**, *7*, 18.

(16)   7.23A ed.; Bruker AXS Inst. Inc.: Madison, WI, 2005.

(17)   Sheldrick, G. *Acta Crystallographica Section A* **2008**, *64*, 112.

(18)   Dolomanov, O. V.; Bourhis, L. J.; Gildea, R. J.; Howard, J. A. K.; Puschmann, H. *Journal of Applied Crystallography* **2009**, *42*, 339.

(19)   Spek, A. L.; Utercht University: Utrect, The Netherlands 2001, 2001.

(20)   Sheldrick, G. M.; Georg-August-Universität Göttingen: 2013.

(21)   Trotter, P.; White, P. *Applied Spectroscopy* **1978**, *32*, 323.

(22)   Chen, X.; Rickard, M. A.; Hull Jr, J. W.; Zheng, C.; Leugers, A.; Simoncic, P. *Inorganic chemistry* **2010**, *49*, 8684.

(23)   Burns, G. R.; Renner, R. M. *Spectrochimica Acta Part A: Molecular Spectroscopy* **1991**, *47*, 991.

(24)   Nour, E.; Shahada, L. *Spectrochimica Acta Part A: Molecular Spectroscopy* **1989**, *45*, 1033.

(25)   Sugai, S.; Saito, G. *Synthetic Metals* **1987**, *19*, 231.

(26)   Świetlik, R.; Schweitzer, D.; Keller, H. *Physical Review B* **1987**, *36*, 6881.

(27)   Kalina, D. W.; Lyding, J. W.; Ratajack, M. T.; Kannewurf, C. R.; Marks, T. J. *Journal of the American Chemical Society* **1980**, *102*, 7854.

(28)   Shao, Y.; Molnar, L. F.; Jung, Y.; Kussmann, J.; Ochsenfeld, C.; Brown, S. T.; Gilbert, A. T.; Slipchenko, L. V.; Levchenko, S. V.; O'Neill, D. P. *Physical Chemistry Chemical Physics* **2006**, *8*, 3172.

(29)   Kurtz, S. K.; Perry, T. T. *Journal of Applied Physics* **1968**, *39*, 3798.

Chapter 4 References

(1)   Èvarestov, R. A. *Theoretical modeling of inorganic nanostructures: Symmetry and ab-initio calculations of nanolayers, nanotubes and nanowires*; Springer, 2015.

(2)   Hornig, D. F. *The Journal of Chemical Physics* **1948**, *16*, 1063.

(3)   Cavalleri, A.; Toth, C.; Siders, C. W.; Squier, J. A.; Raksi, F.; Forget, P.; Kieffer, J. C. *Phys Rev Lett* **2001**, *87*, 237401.

(4)   Zhao, Y.; Weidner, D. J. *Physics and chemistry of minerals* **1991**, *18*, 294.

(5)   Tamm, I. *Zeitschrift für Physik* **1932**, *76*, 849.

(6)   Compaan, A.; Lee, M.; Trott, G. *Physical Review B* **1985**, *32*, 6731.

(7)   Kartha, G.; Ahmed, F. *Acta Crystallographica* **1960**, *13*, 532.

(8)   Keller, R.; Holzapfel, W.; Schulz, H. *Physical Review B* **1977**, *16*, 4404.

(9)   Salje, E. K.; Rehmann, S.; Pobell, F.; Morris, D.; Knight, K. S.; Herrmannsdörfer, T.; Dove, M. T. *Journal of Physics: Condensed Matter* **1997**, *9*, 6563.

(10)   Friese, K.; Kanke, Y.; Fitch, A. N.; Grzechnik, A. *Chemistry of Materials* **2007**, *19*, 4882.

(11)   Morris, D. *Acta Crystallographica* **1956**, *9*, 197.

(12)   Jayaraman, A. *Reviews of Modern Physics* **1983**, *55*, 65.

(13)   Miletich, R.; Allan, D. R.; Kuhs, W. F. *Reviews in mineralogy and geochemistry* **2000**, *41*, 445.

(14)   Michielsen, J.; Woerlee, P.; vd Graaf, F.; Ketelaar, J. *Journal of the Chemical Society, Faraday Transactions 2: Molecular and Chemical Physics* **1975**, *71*, 1730.

(15)   Gale, J. D. In *Handbook of Materials Modeling*; Springer: 2005, p 479.

(16)   Stoneham, A.; Harding, J. *Annual Review of Physical Chemistry* **1986**, *37*, 53.

(17)   Swamy, V.; Gale, J. D. *Phys. Rev. B: Condens. Matter* **2000**, *62*, 5406.

Chapter 5 References

(1)   Tucker, M.; Keen, D.; Dove, T. *Mineralogical Magazine* **2001**, *65*, 489.

(2)   Fontana, M.; Metrat, G.; Servoin, J.; Gervais, F. *Journal of Physics C: Solid State Physics* **1984**, *17*, 483.

(3)   Bratton, R.; Tien, T. *Journal of the American Ceramic Society* **1967**, *50*, 90.

(4)   Sepliarsky, M.; Phillpot, S.; Stachiotti, M.; Migoni, R. *Journal of applied physics* **2002**, *91*, 3165.

(5)   Dove, M. T. *American Mineralogist* **1997**, *82*, 213.

(6)   Krakauer, H.; Yu, R.; Wang, C.-Z.; Rabe, K. M.; Waghmare, U. V. *Journal of Physics: Condensed Matter* **1999**, *11*, 3779.

(7)   Robertson, H. P. *Physical Review* **1929**, *34*, 163.

(8)   Domany, E.; Schick, M.; Walker, J.; Griffiths, R. *Physical Review B* **1978**, *18*, 2209.

(9)   Zhou, Y.; Hall, C. K.; Karplus, M. *Physical review letters* **1996**, *77*, 2822.

(10)   Boukhari, A.; Chaminade, J.; Vlasse, M.; Pouchard, M. *Acta Crystallographica Section B: Structural Crystallography and Crystal Chemistry* **1979**, *35*, 1983.

(11)   Rüdorff, W.; Krug, D. *Zeitschrift für anorganische und allgemeine Chemie* **1964**, *329*, 211.

(12)   Tolédano, P.; Dmitriev, V. *Reconstructive phase transitions: in crystals and quasicrystals*; World Scientific: Singapore, 1996.

(13)   Anderson, P. W. *Some General Thoughts about Broken Symmetry*, DTIC Document, 1981.

(14)   Ceriani, C.; Laio, A.; Fois, E.; Gamba, A.; Martoňák, R.; Parrinello, M. *Physical Review B* **2004**, *70*, 113403.

(15)   Matsui, M.; Akaogi, M. *Molecular Simulation* **1991**, *6*, 239.

(16)   Zahn, D.; Leoni, S. *Physical review letters* **2004**, *92*, 250201.

(17)   Zahn, D.; Hochrein, O.; Leoni, S. *Physical Review B* **2005**, *72*, 094106.

(18)   Rodriguez, J.; Gonzalez-Calbet, J.; Grenier, J.; Pannetier, J.; Anne, M. *Solid state communications* **1987**, *62*, 231.

(19)   Baldinozzi, G.; Simeone, D.; Gosset, D.; Dutheil, M. *Physical review letters* **2003**, *90*, 216103.

(20)   Zelinska, M.; Assoud, A.; Graf, C.; Kleinke, H. *Inorganic chemistry* **2009**, *49*, 1090.

(21)   Yamada, K.; Sera, H.; Sawada, S.; Tada, H.; Okuda, T.; Tanaka, H. *Journal of Solid State Chemistry* **1997**, *134*, 319.

(22)   Čančarević, Ž. P.; Schoen, J. C.; Jansen, M. *Chemistry–An Asian Journal* **2008**, *3*, 561.

(23)   Stokes, H. T.; Hatch, D. M.; Dong, J.; Lewis, J. P. *Physical Review B* **2004**, *69*, 174111.

(24)   Kinoshita, T.; Mashimo, T.; Kawamura, K. *Journal of Physics: Condensed Matter* **2005**, *17*, 1027.

Chapter 6 References

(1)   Rice, O. *Journal of the American Chemical Society* **1941**, *63*, 3.

(2)   Ling, R. C. *The Journal of Chemical Physics* **1956**, *25*, 609.

(3)   Ackland, G. J.; Vitek, V. *Physical review B* **1990**, *41*, 10324.

(4)   Born, M.; Mayer, J. E. *Zeitschrift für Physik* **1932**, *75*, 1.

(5)   Michielsen, J.; Woerlee, P.; vd Graaf, F.; Ketelaar, J. *Journal of the Chemical Society, Faraday Transactions 2: Molecular and Chemical Physics* **1975**, *71*, 1730.

(6)   Gale, J. D. *Philosophical Magazine B* **1996**, *73*, 3.

(7)   Balamane, H.; Halicioglu, T.; Tiller, W. *Physical Review B* **1992**, *46*, 2250.

(8)   Zhang, X.; Yu, L.; Zakutayev, A.; Zunger, A. *Advanced Functional Materials* **2012**, *22*, 1425.

(9)   Gautier, R.; Zhang, X.; Hu, L.; Yu, L.; Lin, Y.; Sunde, T. O.; Chon, D.; Poeppelmeier, K. R.; Zunger, A. *Nature chemistry* **2015**, *7*, 308.

(10)   Huggins, M. L.; Mayer, J. E. *The Journal of Chemical Physics* **1933**, *1*, 643.

(11)   Huggins, M. L. *The Journal of Chemical Physics* **1937**, *5*, 143.

(12)   Tersoff, J. *Physical Review B* **1988**, *37*, 6991.

(13)   Van Duin, A. C.; Dasgupta, S.; Lorant, F.; Goddard, W. A. *The Journal of Physical Chemistry A* **2001**, *105*, 9396.

(14)   Gale, J. D.; Rohl, A. L. *Molecular Simulation* **2003**, *29*, 291.

(15)   Tosi, M.; Fumi, F. *Journal of Physics and Chemistry of Solids* **1964**, *25*, 45.

(16)   Hafemeister, D.; Zahrt, J. *The Journal of Chemical Physics* **1967**, *47*, 1428.

(17)   Lennard, J.; Jones, I. In *Proc. R. Soc. London* 1924; Vol. 106, p 441.

(18)   Beswick, J.; Jortner, J. *Advances in Chemical Physics: Photoselective Chemistry, Part 1, Volume 47* **1981**, 363.

(19)   De Launay, J. *The Journal of Chemical Physics* **1953**, *21*, 1975.

(20)   Epstein, P. S. *Physical Review* **1946**, *70*, 915.

(21)   Zener, C. *Physical Review* **1947**, *71*, 323.

(22)   Daw, M. S.; Foiles, S. M.; Baskes, M. I. *Materials Science Reports* **1993**, *9*, 251.

(23)   Thomson, J. J. *The London, Edinburgh, and Dublin Philosophical Magazine and Journal of Science* **1904**, *7*, 237.

(24)   Mishin, Y.; Farkas, D.; Mehl, M.; Papaconstantopoulos, D. *Physical Review B* **1999**, *59*, 3393.

(25)   Porter, L. J.; Justo, J. F.; Yip, S. *Journal of applied physics* **1997**, *82*, 5378.

(26)   Heinz, D. L.; Jeanloz, R. *Physical Review B* **1984**, *30*, 6045.

(27)   Harding, J. *Molecular Simulation* **1990**, *4*, 255.

(28)   Stoneham, A.; Harding, J. *Annual Review of Physical Chemistry* **1986**, *37*, 53.

(29)   Shanker, J.; Kumar, M. *physica status solidi (b)* **1987**, *142*, 325.

(30)   Brockhouse, B. t.; Iyengar, P. *Physical Review* **1958**, *111*, 747.

(31)   Gale, J. D. In *Handbook of Materials Modeling*; Springer: 2005, p 479.

Chapter 7 References

(1)   Alder, B. J.; Wainwright, T. *The Journal of Chemical Physics* **1959**, *31*, 459.

(2)   Streett, W.; Tildesley, D.; Saville, G. *Molecular Physics* **1978**, *35*, 639.

(3)   Ryckaert, J.-P.; Ciccotti, G.; Berendsen, H. J. *Journal of Computational Physics* **1977**, *23*, 327.

(4)   Ciccotti, G.; Ferrario, M.; Schuette, C. **2014**.

(5)   Ballone, P. *Entropy* **2013**, *16*, 322.

(6)   Brünger, A.; Brooks, C. L.; Karplus, M. *Chemical physics letters* **1984**, *105*, 495.

(7)   Parlinski, K.; Li, Z.; Kawazoe, Y. *Physical Review Letters* **1997**, *78*, 4063.

(8)   Borwein, D.; Borwein, J. M.; Taylor, K. F. *Journal of mathematical physics* **1985**, *26*, 2999.

(9)   Madelung, E. *Phys. Z* **1918**, *19*, 524.

(10)   Ewald, P. P. *Annalen der Physik* **1921**, *369*, 253.

(11)   Wolf, D.; Keblinski, P.; Phillpot, S.; Eggebrecht, J. *The Journal of chemical physics* **1999**, *110*, 8254.

(12)   Fennell, C. J.; Gezelter, J. D. *The Journal of chemical physics* **2006**, *124*, 234104.

(13)   Hill, T. L. *An introduction to statistical thermodynamics*; Courier Corporation, 2012.

(14)   Oliver, P.; Watson, G.; Parker, S. *Physical Review B* **1995**, *52*, 5323.

(15)   Gale, J. D.; Rohl, A. L. *Molecular Simulation* **2003**, *29*, 291.

(16)   Andersen, H. C. *The Journal of chemical physics* **1980**, *72*, 2384.

(17)   Berendsen, H. J.; Postma, J. v.; van Gunsteren, W. F.; DiNola, A.; Haak, J. *The Journal of chemical physics* **1984**, *81*, 3684.

(18)   Parrinello, M.; Rahman, A. *Physical Review Letters* **1980**, *45*, 1196.

(19)   Harvey, S. C.; Tan, R. K. Z.; Cheatham, T. E. *Journal of Computational Chemistry* **1998**, *19*, 726.

Chapter 8 References

(1)   Marvel, M. R.; Lesage, J.; Baek, J.; Halasyamani, P. S.; Stern, C. L.;

Poeppelmeier, K. R. *Journal of the American Chemical Society* **2007**, *129*, 13963.

(2)   Pinlac, R. A. F.; Stern, C. L.; Poeppelmeier, K. R. *Crystals* **2011**, *1*, 3.

(3)   Chang, K. B.; Edwards, B. W.; Frazer, L.; Lenferink, E. J.; Stanev, T. K.; Stern,

N. P.; Nino, J. C.; Poeppelmeier, K. R. *Journal of Solid State Chemistry* **2015**.

(4)   Chang, K. B.; Vinokur, A.; Pinlac, R. A. F.; Suchomel, M. R.; Marvel, M. R.;

Poeppelmeier, K. R. *Inorganic chemistry* **2014**, *53*, 6979.

(5)   Han, H.; Cheng, C.; Xiong, X.-G.; Su, J.; Dai, J.-X.; Wang, H.; Yin, G.; Huai, P.

Materials **2015**, *8*, 8578.

(6)   Vasiliev, A.; Laptash, N. *Journal of Structural Chemistry* **2012**, *53*, 902.

(7)   Stokes, H. T.; Hatch, D. M. *Journal of Applied Crystallography* **2005**, *38*, 237.

(8)   Agulyansky, A. *Chemistry of tantalum and niobium fluoride compounds*;

Elsevier: Amsterdam, The Netherlands, 2004.

(9)   Molokeev, M.; Fokina, V.; Kocharova, A.; Aleksandrov, K. *Physics of the Solid

State* **2011**, *53*, 834.

(10)   Udovenko, A. A.; Laptash, N. M. *Acta crystallographica. Section B, Structural

science* **2011**, *67*, 447.

(11)   Udovenko, A. A.; Laptash, N. M. *Acta crystallographica. Section B, Structural

science* **2008**, *64*, 527.

(12)   Udovenko, A. A.; Laptash, N. M. *Acta Crystallographica Section B: Structural

Science* **2008**, *64*, 645.

(13)   Welk, M. E.; Norquist, A. J.; Arnold, F. P.; Stern, C. L.; Poeppelmeier, K. R. *Inorganic Chemistry* **2002**, *41*, 5119.

(14)   Sheldrick, G. M.; Schneider, T. R. *Methods in enzymology* **1997**, *277*, 319.

(15)   Dera, P. *GeoSoilEnviroCARS, Argonne, Illinois* **2007**.

(16)   Parrinello, M.; Rahman, A. *Physical Review Letters* **1980**, *45*, 1196.

(17)   Wolf, D.; Keblinski, P.; Phillpot, S.; Eggebrecht, J. *The Journal of chemical physics* **1999**, *110*, 8254.

(18)   Fennell, C. J.; Gezelter, J. D. *The Journal of chemical physics* **2006**, *124*, 234104.

(19)   Sheppard, D.; Xiao, P.; Chemelewski, W.; Johnson, D. D.; Henkelman, G. *The Journal of chemical physics* **2012**, *136*, 074103.

(20)   Perdew, J. P.; Ruzsinszky, A.; Csonka, G. I.; Vydrov, O. A.; Scuseria, G. E.; Constantin, L. A.; Zhou, X.; Burke, K. *Physical Review Letters* **2008**, *100*, 136406.

(21)   Kresse, G.; Furthmüller, J. *Physical Review B* **1996**, *54*, 11169.

(22)   Kresse, G.; Joubert, D. *Physical Review B* **1999**, *59*, 1758.

(23)   Blöchl, P. E. *Physical Review B* **1994**, *50*, 17953.

(24)   Monkhorst, H. J.; Pack, J. D. *Physical Review B* **1976**, *13*, 5188.

(25)   Togo, A.; Oba, F.; Tanaka, I. *Phys. Rev. B: Condens. Matter* **2008**, *78*, 134106.

Chapter 9 References

(1)   Chen, C.-T. *Acta Physica Sinica* **1977**, *26*, 124.

(2)   Chen, C. T. *Scientia Sinica* **1978**, *22*, 756

(3)   Welk, M. E.; Norquist, A. J.; Poeppelmeier, K. R. *Abstracts of Papers, 221st ACS National Meeting, San Diego, CA, United States, April 1-5, 2001* **2001**, INOR.

(4)   Maggard, P. A.; Nault, T. S.; Stern, C. L.; Poeppelmeier, K. R. *Journal of Solid State Chemistry* **2003**, *175*, 27.

(5)   Marvel, M. R.; Lesage, J.; Baek, J.; Halasyamani, P. S.; Stern, C. L.; Poeppelmeier, K. R. *Journal of the American Chemical Society* **2007**, *129*, 13963.

(6)   Wu, H.; Yu, H.; Yang, Z.; Hou, X.; Su, X.; Pan, S.; Poeppelmeier, K. R.; Rondinelli, J. M. *Journal of the American Chemical Society* **2013**, *135*, 4215.

(7)   Donakowski, M. D.; Gautier, R.; Yeon, J.; Moore, D. T.; Nino, J. C.; Halasyamani, P. S.; Poeppelmeier, K. R. *Journal of the American Chemical Society* **2012**, *134*, 7679.

(8)   Holland, M.; Donakowski, M. D.; Pozzi, E. A.; Rasmussen, A. M.; Tran, T. T.; Pease-Dodson, S. E.; Halasyamani, P. S.; Seideman, T.; Van Duyne, R. P.; Poeppelmeier, K. R. *Inorganic chemistry* **2013**, *53*, 221.

(9)   Müser, M.; Binder, K. *Physics and Chemistry of Minerals* **2001**, *28*, 746.

(10)   Ceriani, C.; Laio, A.; Fois, E.; Gamba, A.; Martoňák, R.; Parrinello, M. *Physical Review B* **2004**, *70*, 113403.

(11)   Kinoshita, T.; Mashimo, T.; Kawamura, K. *Journal of Physics: Condensed Matter* **2005**, *17*, 1027.

(12)   Ballone, P. *Entropy* **2013**, *16*, 322.

(13)   Gale, J. D. In *Handbook of Materials Modeling*; Springer: 2005, p 479.

(14)   Swamy, V.; Gale, J. D. *Physical Review B* **2000**, *62*, 5406.

(15)   Holland, M.; Charles, N.; Rondinelli, J. M.; Poeppelmeier, K. R. *Journal of the American Chemical Society* **2016**.

(16)   Èvarestov, R. A. *Theoretical modeling of inorganic nanostructures: Symmetry and ab-initio calculations of nanolayers, nanotubes and nanowires*; Springer, 2015.

(17)   Pinlac, R. A. F.; Stern, C. L.; Poeppelmeier, K. R. *Crystals* **2011**, *1*, 3.